Experimental characterization of axial dispersion in coiled flow inverters

By

Luigi Gargiulo

University College London

Department of Chemical Engineering

Supervisors

Dr Luca Mazzei

Prof. Asterios Gavriilidis

A thesis submitted for the degree of

Master of Philosophy

2015

I, Luigi Gargiulo, confirm that the work presented in this thesis is my own. Where information has been derived from other sources, I confirm that this has been indicated in the thesis.

Abstract

Narrow residence time distributions (RTDs) are extremely desirable in many chemical engineering processes where plug flow behaviour is requested. However, at low Reynolds numbers the flow is laminar resulting in strong radial velocity gradients. This in turn causes spreading of fluid particles, usually referred to as hydrodynamic dispersion. Such problem is particularly relevant to microfluidic devices operated in laminar regime due to the reduced dimension and low operating flow rates. Many solutions have been proposed to reduce the hydrodynamic dispersion: static mixers, segmented flow, secondary flow, etc. The latter relies on the action of centrifugal force inducing transversal mixing in helically coiled tubes. Further mixing and therefore reduced dispersion can be achieved by introducing geometrical disturbances, generating chaotic advection.

Coiled flow inverters (CFI) exploit the beneficial effects of secondary flow and chaotic advection. They consist of sections of helically coiled tubes with 90-degree bends placed at regular intervals along a cylindrical support. Despite being a very promising solution, they have not been extensively adopted. This is due to the lack of experimental data and correlations relating the design parameters and operating conditions to the reduction of hydrodynamic dispersion.

In this thesis, a flexible and reliable experimental procedure was developed to investigate RTD in microfluidic devices. It resorts to step input injections and UV-vis inline spectroscopy for detecting the concentration of tracer. The procedure was validated using Taylor's dispersion for straight tubes. The platform was then employed to perform experiments on CFIs, constructed with microfluidic capillaries, varying operating conditions and a geometrical parameter. A similar characterization was carried out on helically coiled tubes. A significant reduction of axial dispersion was observed as compared to straight pipes, confirming the available data in the literature. It was also demonstrated that the curvature ratio primarily defines the strength of radial mixing in CFIs and therefore represents a crucial design parameter.

Table of contents

List of figures

List of tables

Chapter 1

Introduction

In recent years, there has been an increasing interest in *process intensification* to respond to the need for more environmentally friendly and more efficient operations in chemical engineering. The idea of dramatically reducing the size of process plants as a means to render them more efficient both in terms of raw materials and energy consumption started in the 90`s. Since then a new fast developing research field, usually referred to as microfluidics, has attracted researchers analyzing the possibility of exploiting the advantageous properties of miniaturization.

Microfluidics is defined as *"the science and engineering of systems in which fluid behavior differs from conventional flow theory primarily due to the small length scale of the system*" (Nguyen, 2002). The attribute *micro-* refers to the length scale that determines the characteristics of the flow: internal sizes of microfluidic devices range from 1 to 1000 μm. The reduced dimensions enable to operate with high surface-to-volume ratio leading to significant advantages compared to large scale systems: enhanced mass and heat transfer; improved controllability (as a result of shortened response time); increased safety (as a result of reduced volumes). Moreover, in microfluidic systems traditional scale-up is substituted by numbering-up, in a process known as scale-out, without the need for a pilot plant, shortening dramatically the time that it takes from formulation to production. This could lead to the adoption of microfluidic technologies not only for analytical purposes but also for large scale manufacturing in process industries, particularly fine chemistry and pharmaceuticals (Roberge et al., 2005). In more recent years microfluidic devices have been extensively adopted as analytical tools mainly for biochemistry and molecular biology applications (Cho et al., 2011). Despite an enormous potential, the adoption of microfluidics for process intensification of conventional chemical engineering processes is still very limited. This is due to a number of intrinsic challenges that are yet to be addressed, such as high pressure drops, clogging, hydrodynamic dispersion (i.e. the spreading of

fluid particles due to both convection and molecular diffusion). Among these, significant hydrodynamic dispersion arising from laminar flow is particularly relevant for many continuous operations.

In microfluidic devices with simple geometries, the flow behaviour is dictated by viscous forces rather than inertia, as a result of the operating low Reynolds number (Squires and Quake, 2005). The absence of turbulence makes diffusion the only transport mechanism and, despite the shortened length scale, in general this is a rather slow process. A whole branch of microfluidics has been dedicated to the proposition of complex micro-structures capable of achieving faster and more effective mixing. Parallel and serial lamination, flow focusing, split and recombination are examples of passive micromixers designed to shorten mixing times (Hessel et al., 2005; Nguyen and Wu, 2005). These are very effective tools in applications where fast mixing between different streams is crucial. However, low hydrodynamic dispersion is essential for many other continuous processes, such as flow reactions or particle synthesis. Approaching plug-flow behaviour is required for a wide range of chemical reactions as well as for nano- and micro- particle synthesis (Marre and Jensen, 2010).

When dealing with synthesis of particles, the precise control of their final size is crucial. The residence time experienced by particles in the reactor dictates their final size and therefore is a crucial aspect to monitor. However, due to hydrodynamic dispersion, forming particles experience a wide range of residence times, eventually resulting in a broad range of sizes. One of the solutions proposed to approach plug-flow resorts to multiphase segmented flow, with growing particles confined to the dispersed phase. Segmented flow, also referred to as slug flow, is characterized by the introduction of a second phase at flow rate ratios around 1 to create slugs of each individual phase. The slugs behave as small batch reactors travelling through the systems, effectively reducing the dispersion of residence time. Nonetheless, achieving stable slugs particularly for cases where long residence times are needed can be challenging. The introduction of an additional phase requires also down-stream separation operations that are not always desired for industrial applications. As a result, we shall focus on studying different solutions, capable of reducing the extent of axial dispersion in microfluidic devices, relying on modifications of the geometry, rather than on the flow conditions.

In this work, the focus was on a class of structures that have been demonstrated to act positively on the hydrodynamics of tubular systems operating under laminar regime. Exploiting the action of centrifugal force, one can alter the velocity profile and induce recirculation in the radial direction, resulting in the creation of a secondary flow. This can be achieved in helically coiled tubes that can be simply constructed with capillaries on cylindrical supports. Changing the direction of action of the centrifugal force, the radial vortices shift resulting in a further mitigation of the velocity gradient. This idea was firstly proposed by Saxena and Nigam (1984) in their pioneering work on coiled flow inverters (CFI). However, their paper still remains, to our knowledge, the only available work concerned with the reduction of hydrodynamic dispersion in single phase flow. The absence of systematic work characterizing the effect of design parameters of CFI on the hydrodynamic properties has possibly prevented their adoption on a larger scale so far. CFIs have been constructed using pipes coiled on tridimensional structures designed to induce the flow inversions. However, the recent and fast development of 3D printing techniques allows a whole new class of tri-dimensional structures to be designed and fabricated (Capel et al., 2013). Such techniques offer the possibility of designing and manufacturing precisely CFIs in compact structures, with the possibility of integration of other components needed for continuous operations.

1.1 Research objectives

CFIs represent a potential solution to reduce the hydrodynamic dispersion in microfluidic devices operated in single-phase flow. The main objective of this thesis is to carry out an experimental characterization of the hydrodynamics of coiled flow inverters. The motivation behind this is the absence of experimental data related to the axial dispersion of such systems. We aim to verify and possibly extend the available data on the hydrodynamics of CFIs. We also aim to investigate fluid dynamic conditions (i.e. Reynolds numbers) as well as CFIs parameters relevant to microfluidic applications.

A crucial step towards this goal is the development of a reliable experimental setup to measure RTDs. We aim to provide insight into the challenges involved in the experimental characterization of residence time distributions (RTDs) in microfluidic devices. Eventually our goal is to propose a reliable and flexible experimental procedure to be used to perform RTD experiments on different microfluidic devices.

1.2 Thesis outline

Chapter 2 includes a relevant background as well as literature surveys on the four main research topics: the residence time distribution (RTD) theory, the axial dispersion model, RTD detection systems for microfluidics and secondary flow. In chapter 3, the development of a platform to investigate reliably the hydrodynamics of different microfluidic devices is reported. Two different systems were analysed and of each validation experiments were carried out. Technical challenges encountered and solutions adopted are provided. Finally in Chapter 5, the axial dispersion of CFIs and HCTs was investigated by means of RTDs studies. Three CFIs and HCTs were constructed, using TEFLON capillaries commonly used in microfluidics, with different coil-to-tube diameter ratios (i.e. design parameter indicating the curvature ratio). Experiments were carried out at different Reynolds number and the axial dispersion model was applied to quantify the extent of dispersion. The results were compared with analytical solution for straight pipes.

Chapter 2

Background and literature survey

2.1 Introduction

This chapter aims to provide the reader with the background and literature review necessary to support the work developed in Chapter 3 and 4. It is divided into four major sections:

- An introduction to residence time distribution (RTD) focused on the theory behind it, technical challenges related to experimental investigations and numerical models.
- An introduction to the axial dispersion model (ADM), the flow model adopted in this work to quantify hydrodynamic dispersion.
- A literature survey on the works concerned with hydrodynamics in microfluidic devices.
- A literature review on the effect of secondary flow on the hydrodynamics of pipes operated in laminar flow. Here the so-called helically coiled tubes (HCTs) and coiled flow inverters (CFI), which represent the focus of Chapter 4, are presented. A detailed description of the effect of each different design parameters of CFIs on the axial dispersion is reported.

2.2 Residence Time Distributions (RTDs)

The concept of RTD is mostly linked to the analysis of the performances of chemical reactors. Since its first formulation by Dankwerts (1953), the literature on this subject has been enriched over the years by a significant amount of work. Several authors have dedicated sections of their textbooks to this chemical reaction engineering topic (Fogler, 2006; Levenspiel, 1999; Nauman and Buffham, 1983; Wen and Fan, 1975).

More recently, a comprehensive review has been published by Nauman (2008) reporting the historical development of the RTD theory, the experimental as well as the modeling techniques adopted and its applications.

The RTD is defined as the function $E(t)$ such that the product

$$E(t)\mathrm{d}t \qquad \text{Eq. 2.1}$$

represents the fraction of fluid elements whose residence time in the vessel lies in the range $\mathrm{d}t$ around the time t. $E(t)$ is the *residence time density (or frequency) function*.

Consequently, the fraction of fluid residing in the vessel between t_1 and t_2 is given by:

$$\int_{t_1}^{t_2} E(t)\,\mathrm{d}t \qquad \text{Eq. 2.2}$$

On the other hand, the fraction of fluid with *age* (i.e. time spent in the vessel) smaller than t_1 is given by

$$\int_{0}^{t_1} E(t)\,\mathrm{d}t \qquad \text{Eq. 2.3}$$

Being a probability distribution function, $E(t)$ satisfies the normalization condition:

$$\int_{0}^{\infty} E(t)\,\mathrm{d}t = 1 \qquad \text{Eq. 2.4}$$

The area under the residence time density function is unitary, because the fraction of fluid elements residing into the vessel for a time between 0 and ∞ has to be 1.

For plug flow reactors, the RTD is a delta function centred on the reactor space-time τ; in this case, no real distribution of residence times is present, for every element of fluid resides the same time τ in the reactor. This time, which is also called macroscopic residence time, is a macroscopic property of the system that depends both on the vessel geometry and the operating conditions. For a tubular vessel with constant cross section:

$$\tau = \frac{V}{\dot{v}} = \frac{L}{u} \qquad \text{Eq. 2.5}$$

where V and L are the volume and length of the vessel, respectively, $\dot{v}$ is the volumetric flow rate and u is the velocity of the fluid averaged over the cross-section of the pipe. Note that the space-time can be calculated for any kind of vessel, if one knows its volume and the fluid flow rate. As said, the RTD of the ideal plug flow reactor is a Dirac-δ centred on the reactor space-time, that is:

$$E_{PFR}(t) = \delta(t - \tau) \qquad \text{Eq. 2.6}$$

This function just states that all fluid elements reside in the reactor the same time τ. The other reference flow pattern in RTD theory is that of continuously stirred tank reactor (CSTR). Each element of fluid at the inlet is instantaneously and perfectly mixed with the material already present in the vessel. It can be easily demonstrated that the RTD for CSTR is the following decreasing exponential function:

$$E_{CSTR}(t) = \frac{1}{\tau} e^{-t/\tau} \qquad \text{Eq. 2.7}$$

The RTD of real vessels can only tend to these ideal behaviours and the extent of the deviation must be investigated by means of well-designed RTD studies.

2.2.1 Pulse experiment

In a pulse experiment, a given amount of tracer m_0 is injected istantaneously at the inlet boundary of the vessel with a uniform concentration across the inlet boundary. The concentration of tracer is then recorded as a function of time at the outlet, $C_{pulse}(t)$. For a vessel of volume V with fluid flowing at constant volumetric flow rate $\dot{v}$, the differential fraction of tracer $\mathrm{d}m/m_0$ exiting the vessel between t and $t + \mathrm{d}t$ is given by:

$$\frac{\mathrm{d}m}{m_0} = \frac{\dot{v}\, C_{pulse}(t)\, \mathrm{d}t}{m_0} \qquad \text{Eq. 2.8}$$

Therefore:

$$E(t)\mathrm{d}t = \frac{\mathrm{d}m}{m_0} = \frac{\dot{v}}{m_0} C_{pulse}(t)\mathrm{d}t \qquad \text{Eq. 2.9}$$

The *E* curve is directly obtained from an operation of normalization of $C_{pulse}(t)$ in a pulse experiment, as Eq. 2.9 and Figure 2.1 show. To normalize C_{pulse}, one needs to know the total mass m_0 of tracer injected. If this quantity is unknown, one can easily calculate it using the equation below:

$$m_0 = \int_0^\infty \dot{v} C_{pulse}(t)\,\mathrm{d}t \qquad \text{Eq. 2.10}$$

It derives that the *E* curve can be so determined:

$$E(t) = \frac{C_{pulse}(t)}{\int_0^\infty C_{pulse}(t)\,\mathrm{d}t} \qquad \text{Eq. 2.11}$$

From $E(t)$ the mean residence time can be calculated

$$\bar{t} = \int_0^\infty E(t) t\,\mathrm{d}t \qquad \text{Eq. 2.12}$$

This is the first moment of the distribution. It should be noted that $\bar{t}$ is equal to the space-time only if dead spaces or bypassing are not present in the vessel. Hence, the comparison between the measured mean residence time ($\bar{t}$) and the macroscopic one (τ) is an important tool to evaluate unexpected ills of the reactor.

It is also useful to calculate the *variance* of the distribution, which is the second moment about the mean:

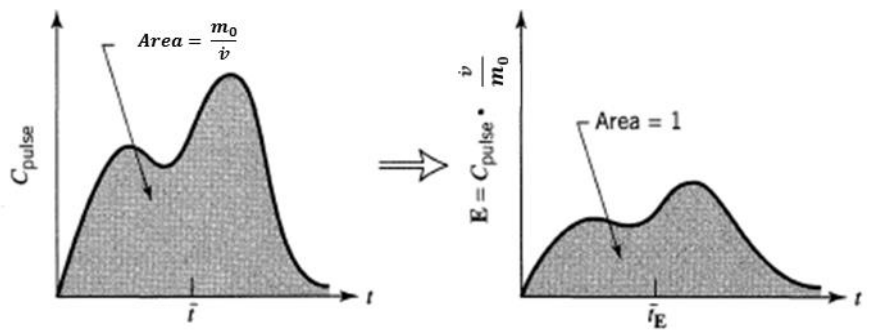

Figure 2.1 - Obtaining the E(t) curve from the experimental C_{pulse} (Levenspiel, 1999).

$$\sigma_t{}^2 = \int_0^\infty (t - \bar{t})^2 E(t)\,\mathrm{d}t \qquad \text{Eq. 2.13}$$

The variance is a measure of the spread of the distribution. The dimensionless variance is defined as:

$$\sigma_\vartheta{}^2 = \frac{\sigma_t{}^2}{\bar{t}^2} \qquad \text{Eq. 2.14}$$

For a plug flow reactor $\sigma_\vartheta{}^2 = 0$ because the variance is zero, whereas in a CSTR the dimensionless variance is unitary. Turbulent flow reactors exhibit $0 < \sigma_\vartheta{}^2 < 1$, while laminar flow reactors can present $\sigma_\vartheta{}^2 > 1$ (Nauman, 2008).

The dimensionless version of the residence time density function, $E_\vartheta(\theta)$, is employed to compare the spread of the distribution of systems with different mean residence time. It is defined in the dimensionless domain of times $\vartheta = t/\,\bar{t}$. The relationship between E and E_ϑ is

$$E_\vartheta = \bar{t}E \qquad \text{Eq. 2.15}$$

Clearly, the first moment of E_θ is equal to 1.

We have seen that from a pulse experiment one can directly extract the E curve without any need of further manipulation of the measured data. The main drawback of this procedure is related to the injection of the tracer. Eq. 2.9 is strictly valid only for a Dirac-δ input, which is complex to achieve in real experiments. A pulse input is performed by introducing a finite amount of tracer. If the total volume of tracer injected is much smaller than the internal volume of the vessel to examine and if the injection time is much smaller than the expected residence times in the system, we can mimic a perfect pulse input and the equations presented, although not strictly valid, are good approximations. An alternative and less complex technique resorts to a step input.

2.2.2 Step experiments

A step input can be performed by instantaneously changing the concentration of tracer at the inlet boundary of the vessel from 0 to a certain value C_{max} and keeping it constant for $t > 0$ at constant volumetric flow rate. The recorded concentration-time curve at the outlet is denoted as C_{step}(t) (Figure 2.2).

A new quantity can be defined:

$$F(t) = \frac{C_{step}(t)}{C_{max}} \qquad \text{Eq. 2.16}$$

The $F(t)$ is called *cumulative distribution function* or simply *F curve* and it is related to the residence time density function. In particular, $F(t)$ represents the fraction of fluid with an age between 0 and t. From Eq. 2.3 we can write:

$$F(t) = \int_0^t E(t')\mathrm{d}t' \qquad \text{Eq. 2.17}$$

Differentiating we can derive the relationship between E and F:

$$\frac{\mathrm{dF}}{\mathrm{d}t} = E \qquad \text{Eq. 2.18}$$

Therefore, to obtain the E curve from a step experiment, one needs to apply an operation of differentiation to the measured data. In theory doing so is simple, but in practice it may significantly increase the noise of the data, particularly when one deals with discrete series of data. Step input experiments, however, are relatively easy to perform compared with those that resort to a pulse input.

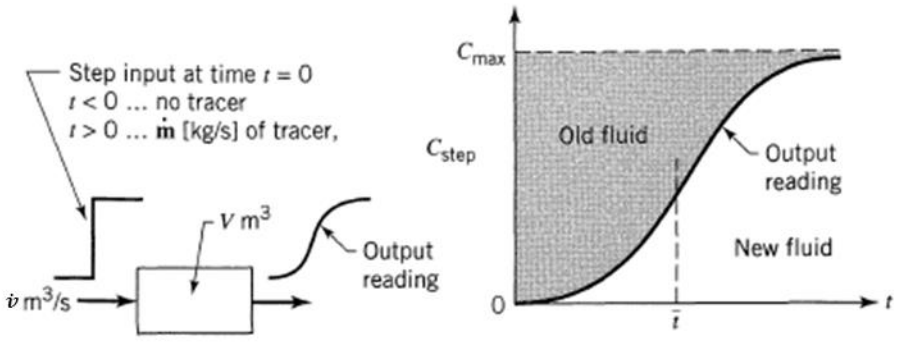

Figure 2.2 - Schematic of a step input experiment (Levenspiel, 1999).

2.2.3 The convolution integral

For arbitrary inputs of tracer, there exists a relationship between the time-dependent concentration curves at the inlet ($C_{in}(t)$) and outlet ($C_{out}(t)$) of the system (Figure 2.3). This relationship is given by:

$$C_{out}(t) = (E * C_{in})(t) = \int_0^t E(t - t')C_{in}(t')\mathrm{d}t' \qquad \text{Eq. 2.19}$$

This is called *convolution integral* or *convolution product*. Although mathematically difficult to manage in the presented form, the convolution integral is an important tool for RTD experiments. As previously mentioned, the biggest challenge is usually related to the injection of the tracer. Additionally, since the injection point may be located at a certain distance from the inlet boundary of the vessel, the shape of the input stimulus produced by the injector change as it approaches the vessel entrance. As a result, the RTD curve cannot always be derived directly from the measured transient concentration in the effluent stream, $C_{out}(t)$. However, if one knows $C_{in}(t)$, for example detecting it as a function of time at the inlet, the convolution integral allows to extract the RTD of the vessel. This procedure is called deconvolution, $E(t)$ being one of the factor of the convolution product.

As a result of the convolution theorem, the Fourier transform of a convolution product corresponds to the product of the Fourier transforms. Therefore:

$$\mathcal{F}(E * C_{in}) = \mathcal{F}(C_{out}) = \mathcal{F}(E)\mathcal{F}(C_{in}) \qquad \text{Eq. 2.20}$$

It is then necessary to transform back the transfer function (Eq. 2.20) to obtain the RTD of the vessel.

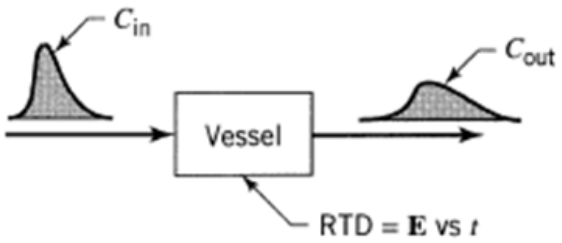

Figure 2.3 – Schematic representation of RTD experiments with arbitrary input.

$$E = \mathcal{F}^{-1}(\mathcal{F}(E)\,) = \mathcal{F}^{-1}\left(\frac{\mathcal{F}(C_{out})}{\mathcal{F}(C_{in})}\right) \qquad \text{Eq. 2.21}$$

Note that in real experiments both $C_{in}(t)$ and $C_{out}(t)$ are available as a series of points, rather than in a continuous form. One of the methods that achieves the inverse transformation from the Fourier domain is the *Fast Fourier Transform* (Cantu-Perez et al., 2010). Although simple, this algorithm can strongly affect the reliability of the results because of the increase of noise. When using such a method we need to further manipulate data (e.g. signal filters); consequently, the possibility of adding inaccuracies is high. An alternative procedure, sometimes referred to as *convolution-deconvolution* method, requires assuming that the RTD is well depicted by a flow model, for instance the axial dispersion model (Bošković and Loebbecke, 2008). The unknown distribution $E^*(t, \boldsymbol{\theta})$ will be function of the vector $\boldsymbol{\theta}$, representing the parameters of the flow model. These can be estimated minimizing the squares of the deviation between the predicted distribution and the measured one, as follows

$$\epsilon = \left[\sum\left(C_{out}(t) - \sum_{0}^{t} C_{in}(t-t')E^*(t', \boldsymbol{\theta})\Delta t'\right)\right]^2 \qquad \text{Eq. 2.22}$$

The convolution-deconvolution method clearly relies on the assumption of the flow model. As a consequence different models can lead to completely dissimilar RTDs. On the other hand, the measured concentration should be consistent with the shape of the distribution predicted by the model, which must be chosen only if this is the case.

2.2.4 Detection of the tracer concentration

When discussing the residence time distribution theory it was assumed that the detection boundary is characterized by flat velocity profiles. However, there exist many circumstances when this is not the case; for instance the parabolic velocity profile occurring in laminar flow systems with circular cross section. The velocity can be expressed as a function of the radial position: $u = u(r)$. We consider only the axial component of the velocity as we assume that particles of fluid do not move in the radial

direction at any point of the system. Additionally, we consider the flowing system to be at steady state. Previously, it was also assumed that the concentration of tracer across these boundaries is uniformly distributed. Removing this restriction and considering the concentration to be dependent on the radial position, we can write $C = C(r)$. It is also assumed that there is no effect of diffusion (neither molecular nor turbulent) across the boundary. For a pulse input experiment, we can express the amount of tracer leaving the system in the differential interval of time $\mathrm{d}t$ as:

$$\mathrm{d}m(t) = \mathrm{d}t \int_A c(r)u(r)\mathrm{d}A \qquad \text{Eq. 2.23}$$

where A denotes the area of the circular section. Now we define the *mixing-cup concentration*

$$c_{mix}(t)\ \dot{v} \equiv \int_A c(r)u(r)\mathrm{d}A \qquad \text{Eq. 2.24}$$

where $\dot{v}$ is the volumetric flow rate. Then, it is

$$\mathrm{d}m(t) = c_{mix}(t)\ \dot{v}\ dt \qquad \text{Eq. 2.25}$$

Let us recall Eq. 2.8, which we initially wrote to relate the residence time density function to the concentration of tracer in a pulse input experiment. It is clear that in the general case of velocity and concentration dependent on the radial position the quantity that one needs to use to obtain $E(t)$ must be the mixing-cup concentration (Levenspiel et al., 1970). Accordingly, the analytical instruments used for detecting the concentration of tracer in residence time distribution experiments should measure the mixing-cup concentration. However, the concentration that most instruments measure is the through-the-wall average concentration, which is defined as:

$$c_{tw}(t)\ A \equiv \int_A c(r)\mathrm{d}A \qquad \text{Eq. 2.26}$$

From this brief discussion, it appears clear that if we use Eq. 2.8 replacing $c_{mix}(t)$ with $c_{tw}(t)$, we make a mistake under the assumptions made above.

However, when the spread of tracer in the radial direction takes place in a time much smaller than the vessel mean residence time, diffusion flattens radial concentration gradients. If this is the case the concentration does not depend on the radial position; therefore, both Eq. 2.24 and Eq. 2.26 reduce to

$$C_{mix}(t) = C_{tw}(t) = C(t) \qquad \text{Eq. 2.27}$$

As a result, if the concentration is evenly distributed over the cross section where the detection takes place, both mixing-cup and through-the-wall concentrations lead to the same result (Minnich et al., 2010).

2.2.5 Choice of tracer and detection system

The reliability of RTD experiments strongly depends on the correct choice of the tracer. This must have some properties that make it detectable by an analytical instrument. At the same time, it should behave very similarly to the fluid it represents (the mother fluid) in terms of flowing properties. In other words, the tracer should present the following attributes (Fogler, 2006):

- chemically inert with respect to the mother fluid;
- identical physical properties (i.e. density, viscosity, diffusion coefficient) as the mother fluid;
- completely miscible with the mother fluid;
- non-interactive with the vessel walls;

If these requirements are all satisfied the tracer is said to be *perfect.* However, the more similar the tracer is to the mother flowing medium, the more complicated its detection (Nauman and Buffham, 1983). Therefore, the choice of the tracer and in turn of the detection method is commonly a compromise between different solutions.

Various options are possible for the detection of the concentration of tracer over time. The most used techniques resort to radiation emission, conductimetry and optical detection.

Radioactive tracers can be considered perfect tracers since they behave exactly as their non-radioactive counterpart (the mother fluid). However, their activity is limited over time; this restricts their applicability. In fact, radioactive tracers must have half-lives (i.e. the time required for the radioactive activity to decrease by half) much greater than the duration of the experiment. Also, experiments involving them require thorough risk assessment and often expensive equipment. For this reason, the choice often falls on *less perfect* tracers and in turn on less sophisticated detection techniques.

In liquid systems, electrolytes solutions are employed in conjunction with conductivity meters, while dyes are detected by means of different optical techniques (e.g. absorbance, fluorescence, reflectance, etc.). The latter option is often preferred as dyes have the advantage of being optically visible. Additionally, optical-based detection systems are non-intrusive, and therefore prevent undesired disturbance to the flow. However, a key requirement for optical-based detection systems is the *linear response of the detector with the concentration of tracer*. Linearity can be achieved by working at low tracer concentrations.

A recurring and common criticism to such systems is that they usually provide spatial averaged composition (through-the-wall concentration) as opposed to flow-weighted measurements (mixing-cup concentration). In fact, although possible, the design of optical-based systems for measuring the mixing-cup concentration is complex and often inaccurate. However, we have seen that when the diffusion time is much smaller than the mean residence time, the tracer has enough time to equally distribute over the cross section. Therefore, in certain conditions the adoption of through-the-wall measurements represents a valid option.

2.2.6 Absorbance based detection systems

Absorbance measurements represent a well-established class of optical detection techniques for RTDs. Such systems are constituted of a light emitter and a receiving sensor located at a given distance (l) with the fluid placed in-between. The signal generated by the sensor depends on the intensity of light passing through the flowing

medium, which in turn is subject to the concentration of tracer. The more concentrated the flowing medium is the less light reaches the sensor and the smaller the recorded intensity is. The absorbance is so defined:

$$A = -\log_{10}\frac{I}{I_0} = -\log_{10} T \qquad \text{Eq. 2.28}$$

Where I represents the intensity of light recorded by the sensor, I_0 is the intensity generated by the light emitter and $T = I/I_0$ is called transmittance. In the ideal case of light passing through the medium without being absorbed or reflected, the sensor would read I_0, therefore the absorbance would be zero whilst the transmittance unity.

At low concentrations of tracer there exists a linear relationship between the absorbance and the concentration. This relation is expressed by the Lambert-Beer law:

$$I = I_0 10^{-\epsilon l c} \qquad \text{Eq. 2.29}$$

where ϵ is the extinction coefficient of the tracer adopted, l is the pathlength or the distance between the emitting light and the receiving sensor, while c is the concentration of tracer one is measuring. Eq. 2.29 leads to

$$A = \epsilon\, l\, c \qquad \text{Eq. 2.30}$$

A plot of A against c is characterized by a straight line up to a value $\bar{c}$ above which the correlation becomes non-linear. Such a graph must be constructed to establish the value of $\bar{c}$ for any specific system. This can be done by sampling known concentrations of tracer, in a process we will later refer to as calibration.

The Lambert-Beer law expresses the attenuation of light intensity as a result of absorption taking place in the medium separating the emitter from the sensor. It should be noted that the extinction coefficient strongly depends on the wavelength of the electromagnetic radiation. Different chemical species have different absorption spectra, meaning that the light is more intensely absorbed in specific ranges of wavelength. Absorbance measurements are specifically designed so that the absorption contribution of the medium, in which the tracer is suspended, is negligible. In other words, the wavelength of the radiation is chosen such that the extinction

coefficient of the tracer is much greater than that of the suspending medium. Under these circumstances, when the tracer is not present ($c = 0$) the intensity attenuation is negligible and one can assume that the receiving sensor detects I_0. As a result, it is correct to say that the incident light intensity (I_0) corresponds to the intensity detected when the concentration of tracer in the medium is zero. The validity of this assumptions can be easily verified through calibration experiments: sampling different tracer concentrations one should obtain a linear curve (for small c) passing through the origin.

As a result, RTD detection systems based on absorbance must be operated in the region of validity of the Lambert-Beer law. To say it differently, low concentrations of tracer need to be employed. On the one hand, one would prefer to operate at diluted conditions as to make sure that the flowing properties of the tracer approach closely those of the carrier fluid. On the other, the sensitivity of the detector may be poor when working with small concentrations. In order to maximize the signal-to-noise ratio, one is to make the difference $I - I_0$ (the signal) dominant over the amplitude of the noise, which is an intrinsic property of the detector. If the signal is to be maximized one should change either the extinction coefficient or the pathlength. The latter is dictated by the peculiarities of the system of interest, specifically for RTD measurements. Conversely, the extinction coefficient for a chemical species depends primarily on the wavelength of the excitation light. It is therefore important to be able to work in a narrow range of wavelengths corresponding to the maximum value of the extinction coefficient. Doing so, one can maximize the signal without the need of adopting large concentrations. As a result, one should be able to set the operating wavelength of the optical detector so as to match the peak of the extinction coefficient of the tracer.

As discussed above, the easiest and most straightforward ways to realize RTD experiments and in turn obtain the residence time density function are the pulse and the step input experiment. When performing pulse input experiments, often one needs to employ concentrations of tracer quite larger than $\bar{c}$ to get an appreciable signal at the detection point. This is particularly encountered when dealing with significantly dispersive vessels. If the RTD system is characterized by two detection points, the one closest to the injection point may experience non-linear effects as a result of the high

concentration adopted. Furthermore, even when working with a single detector, the effect of the tracer flowing properties may be detrimental on the measured RTDs. Conversely, in pulse input experiments the maximum tracer solution is continuously injected into the vessel, as opposed to a single shot in pulse experiments. This makes it possible to adopt much smaller concentrations; thus, step input experiments are more reliable when one resorts to absorbance-based detectors.

In conclusion, although the optimal choice of tracer (and in turn its extinction coefficient), optical sensor and other parameters is complex, absorbance based systems have been extensively used to measure RTDs experimentally, particularly for microfluidic devices (Adeosun and Lawal, 2009; Bošković et al., 2011; Cantu-Perez et al., 2010; M. Günther et al., 2004).

2.2.7 Numerical approaches to model RTDs

Residence time distributions can be predicted numerically. Predicting models offer better flexibility as compared to standard experimental procedures and, at the same time, constitute powerful design tools. Furthermore, as the calculating capacity of modern computers increases, the accuracy and the complexity of systems we are able to investigate improves.

When performing experiments, one operates the flowing system at steady state. The evolution of the concentration of the injected tracer is then tracked in the effluent stream over time. Similarly, one can mimic stimulus-response procedures by carrying out numerically time-dependent studies. In fact, the velocity distributions of the flowing systems can be calculated by means of computational fluid dynamics (CFD). The numerical solution of the continuity and momentum balance equations represents a well-established procedure nowadays thanks to the availability of many commercial codes. The majority of them are based on finite element schemes, where the geometrical domain of the flowing system is divided in several sub-domains (computational cells) and the differential equations reduce to difference equations. CFD codes are particularly reliable and powerful when dealing with laminar flow systems as opposed to turbulent flows, for which computationally demanding sub-models are required to solve flow distributions (Kwak et al., 2005). However, the

precision of numerical solutions strongly depends both on the geometrical complexity and on the dimensions of the system to model. The calculation of the velocity distribution at steady-state represents the first step to predict numerical RTDs. In the second step, a virtual tracer is introduced in the computational domain and tracked over time. To our knowledge, two different methods have been proposed in the literature.

The first method, referred to as *fully-CFD,* solves the convection-diffusion equation my means of CFD. The governing equation is here reported

$$\frac{\partial C_A}{\partial t} + \boldsymbol{u} \cdot \nabla C_A = D_{AB} \nabla^2 C_A \qquad \text{Eq. 2.31}$$

where C_A is the tracer concentration, $\boldsymbol{u}$ is the fluid velocity vector which is a function only of position and D_{AB} is the binary diffusion coefficient of species A (the tracer) into the species B, the carrier fluid. Zero-flux is normally assigned at the walls to model wall impenetrability. At the inlet boundary a given time-dependent law is imposed $C_{A,in} = C_{A,in}(t)$ for any $t > 0$ so as to mimic a transient response experiment. The time evolution of the scalar variable at the outlet boundary is used to reconstruct the RTD. Both mixing-cup and through-the-wall concentrations can be calculated since the local velocity is known across the outlet boundary. Retrieving the local velocity distributions to use in the time-dependent study does not represent a difficulty in terms of implementation of the model. In fact, the solution of the species transport equation is commonly included in commercial CFD codes. However, the main disadvantage of the fully-CFD method lies in the high sensitivity of the results to numerical diffusion. This artificially increases the real diffusion transport of the tracer species, expressed by the term on the right-hand side of Eq. 2.31, making it impossible to discern individual contributions. To reduce undesirable numerical effects, one must adopt small computational cells and time-steps as well as high order resolution schemes. However, this limits the applicability of the method as the calculation times and computational capabilities may become unbearable (Arampatzis et al., 1994).

Differently, one can adopt a Lagrangian point of view and track the motion of the tracer particles as they move in the computational domain. This method, referred to as

particle tracking, adopts notional particles to mimic the RTD. The equation of motion of the generic particle i can be expressed as

$$\boldsymbol{x_i}(t + \Delta t) = \boldsymbol{x_i}(t) + \boldsymbol{u}(\boldsymbol{x_i}(t))\, \Delta t + \boldsymbol{\xi} * \sqrt{2 D_m \Delta t} \qquad \text{Eq. 2.32}$$

where $\boldsymbol{x_i}(t)$ is the vector position of the particle at any time t, $\boldsymbol{u}(\boldsymbol{x_i}(t))$ is the fluid velocity vector at $\boldsymbol{x_i}(t)$, $\boldsymbol{\xi}$ is a random number normally distributed with zero mean and unit variance, D_m is the diffusion coefficient and Δt is the computational time-step. At any time $t + \Delta t$ the position of each particle $\boldsymbol{x_i}$ can be calculated from $\boldsymbol{x_i}(t)$ displaced by the convection term plus an additional term that accounts for diffusion. If one performs the particle tracking over a statistically high number of particles and records the time spent within the computational domain, the RTD can be easily derived. The solution of the equation of motion is easy to solve and is not prone to numerical errors, as it is in the fully-CFD method. However the treatment of the behaviour of particles at the boundaries is not trivial (Nauman, 1981). For instance, specular reflection needs to be implemented to impose wall impenetrability. This implies communication between the code used to calculate the velocity distribution and the particle tracking algorithm. However, many of the available CFD codes do not include particle tracking modules accounting for diffusion. Although the mathematics of the particle tracking method are relatively simple and in turn the computational demand is significantly lower than the fully-CFD method, the implementation of this model is complex due to the boundary conditions.

As part of this work, the *particle tracking* approach was employed to model RTDs of straight pipes operated in the pure convection regime. The objective of this study was to explore the possibility of adopting the modelling approach for RTD characterization of microfluidic devices using the commercial software COMSOL. The results of our validation are reported in Appendix C.

2.3 The axial dispersion model

The most used and simplest model to describe flow systems where both convection and diffusion are important is the axial dispersion model (Aris, 1956; Dankwerts,

1953; Levenspiel et al., 1956; Taylor, 1953). The model is based on the following equation:

$$\frac{\partial C}{\partial t} + u\frac{\partial C}{\partial z} - D_{ax}\frac{\partial^2 C}{\partial z^2} = 0 \qquad \text{Eq. 2.33}$$

where C, the concentration of tracer, is a function of time and of the axial coordinate of the system z, D_{ax} is the axial dispersion coefficient and u is a constant mean axial velocity, which does not depend on z. The model superimposes a one dimensional dispersion process on a plug-flow. For this reason, in many textbooks the axial dispersion model is also referred to as the axial-dispersed plug-flow model. The axial dispersion coefficient is assumed to be independent of both the axial position and the concentration of tracer. It represents the rate of axial dispersion in the vessel. To characterize axial dispersion under different conditions, we adopt dimensionless numbers. The Eq. 2.33 is usually found in non-dimensional form:

$$\frac{\partial C}{\partial \vartheta} + \frac{\partial C}{\partial \xi} - \frac{1}{Pe_L}\frac{\partial^2 C}{\partial \xi^2} = 0 \qquad \text{Eq. 2.34}$$

with $\vartheta = t/\tau = tu/L$ and $\xi = z/L$, where L represents the length of the vessel. It is clear that the model depends on a single parameter known as the Peclet number, $Pe_L = uL/D_{ax}$. Note that in the literature different definitions of this parameter are present; these differ in the choice of the characteristic length (diameter or length of the vessel) and of the diffusion coefficient (molecular or axial diffusion coefficient). Analytical solutions of the RTD subject to several boundary conditions are available in the literature (Levenspiel, 1999; Wen and Fan, 1975). By matching the experimental data obtained from RTD experiments with the analytical solution, one can estimate the axial dispersion coefficient that defines the extent of hydrodynamic dispersion. To do so it is good practice to work with appropriate dimensionless groups.

The inverse of Pe_L is the *vessel dispersion number*. This is a measure of the spread of tracer in the whole vessel and is so defined:

$$N_L \equiv \frac{D_{ax}}{uL} = \frac{L/u}{L^2/D_{ax}} \sim \frac{t_{conv}}{t_{diff}} \qquad \text{Eq. 2.35}$$

where L is the overall length of the tubular vessel. N_L represents the ratio of the convection time to the dispersion time. Indeed, L^2/D_{ax} is the time needed for the tracer to spread over a length L and we refer to it as dispersion time. The ratio L/u is the characteristic time for convection and corresponds also to the available time for any dispersion process to occur. When $N_L \gg 1$ the time available is much greater than the characteristic time of diffusion; therefore, the tracer will have time enough to spread over a length comparable with the length of the vessel. Conversely, when $N_L \ll 1$ the time available to the tracer for spreading over a length comparable to the length of the vessel is not enough. As a result of this, the higher the vessel dispersion number is the broader the RTD will be. N_L is widely used to characterize hydrodynamic dispersion and specifically to compare dispersion performances of vessels having different lengths. In some cases a similar group is reported, defined with the diameter of the pipe d_t as characteristic length:

$$N_d \equiv \frac{D_{ax}}{u d_t} = \frac{d_t/u}{d_t^2/D_{ax}} \sim \frac{t_{conv}}{t_{diff}} \qquad \text{Eq. 2.36}$$

Similarly, we can interpret this dimensionless group in terms of the ratio of characteristic times: convection and diffusion. The diffusion time is defined as the time needed for the tracer to spread over a distance equal to the diameter of the tubular vessel (or hydraulic diameter for any other cross-sectional shape): d_t^2/D_{ax} . The convection time in this group is d_t/u. This is not prone to a physical interpretation as the convection time of the previous group representing the available time in the vessel. Therefore, N_d does not provide an overall measure of the dispersion behaviour of the vessel. However, it is widely used to characterize dispersion in dimensionless flow regime maps as a function of Re.

It should be noted that both N_L and N_d are defined in terms of the axial dispersion coefficient (not of molecular diffusivity). Conversely, the Bodenstein number is so defined:

$$Bo = Re\ Sc = \frac{\rho u d_t}{\mu} \frac{\mu}{\rho D_m} = \frac{u d_t}{D_m} \qquad \text{Eq. 2.37}$$

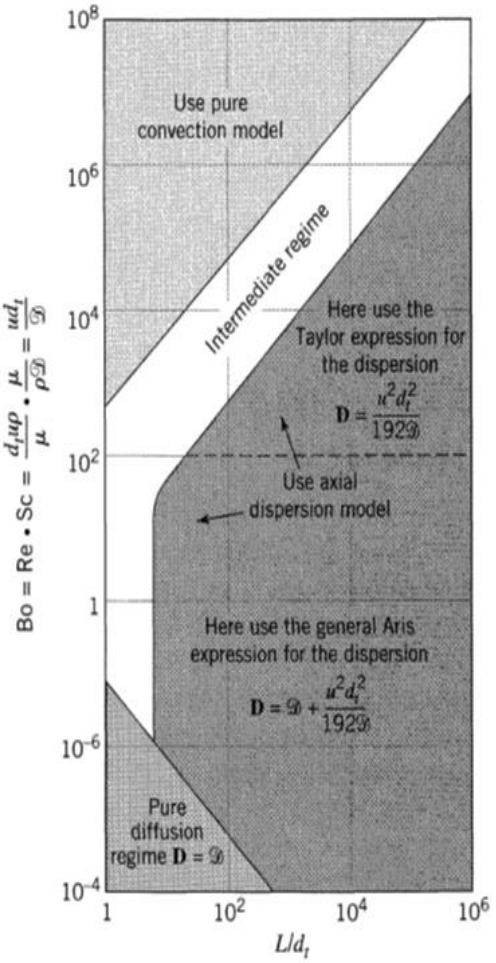

Figure 2.4 – Map suggesting flow model to adopt for straight pipes. The operational point can be found on the map knowing the aspect ratio of the pipe and Bo (Anthakrishnan et al., 1965).

where D_m is the molecular diffusion coefficient, Re the Reynolds number and Sc the Schmidt number. This number represents the ratio of the rate of convection to the rate of diffusion. At low Bo molecular diffusion predominates over convection and viceversa.

The axial dispersion model can be applied to both turbulent and laminar flows. However, while in the first case there are no limitations, for laminar flow the model holds only when $1/Bo$ and L/d_t are sufficiently large. In other words, the time scale of the molecular diffusion must be smaller than the mean residence time of the vessel ($\bar{t} = u/L$). In liquid systems very long pipes are needed for the model to be applicable (Figure 2.4).

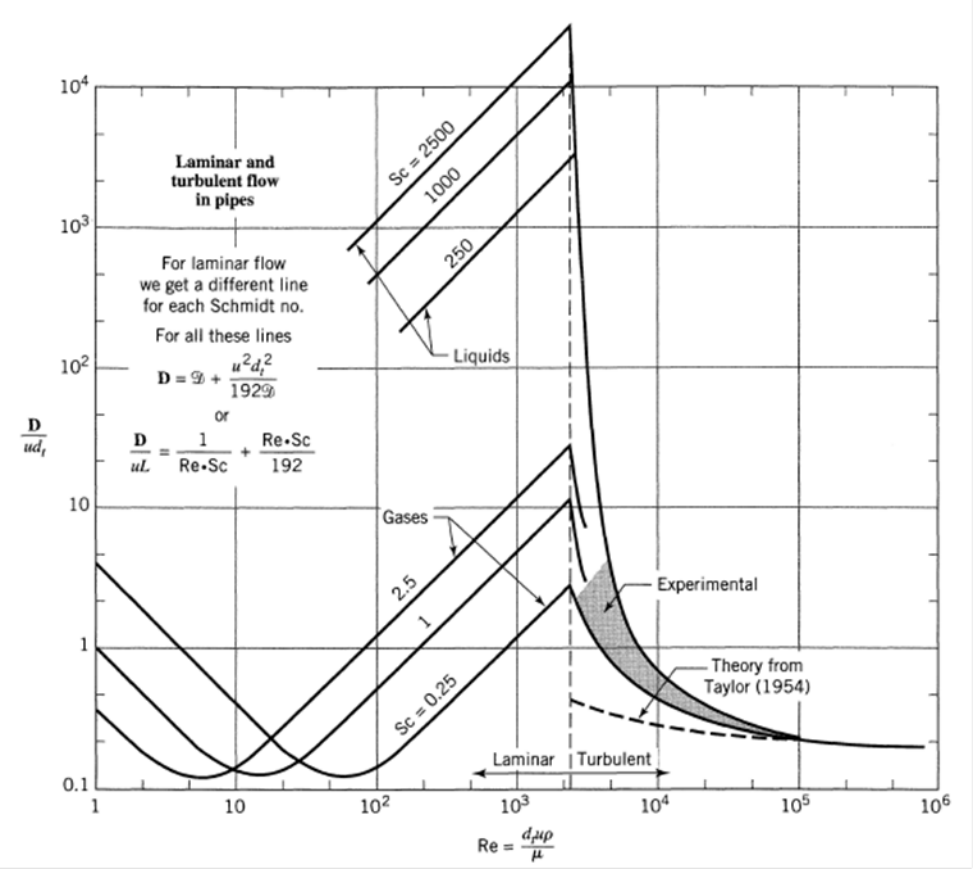

Figure 2.5 - Correlation for vessel dispersion number of straight tubes under both turbulent and laminar regime (Levenspiel, 1999).

Correlations are available for the vessel dispersion number of straight pipes as a function of Reynolds number (Figure 2.5). In laminar regime the dispersion number strongly depends on the Schmidt number. At very low Reynolds number molecular diffusion is the only dispersive mechanism and if the diffusion rate increases (i.e. smaller Schmidt number) the overall dispersion is promoted. At higher flowrate the effect of molecular diffusion is exactly the opposite: for a given Reynolds number, systems with smaller Schmidt number are less dispersive. In laminar regime we can observe a minimum value of the vessel dispersion occurring at different Reynolds numbers depending on Sc. With the transition to turbulent regime the dispersion characteristics become less and less dependent on the diffusion behaviour of the system. A peak can be observed in the transitional regime. For Reynolds numbers larger than 2000 the main dispersive mechanism is turbulence and N_d becomes a monotonic decreasing function of the Reynolds number (Wen and Fan, 1975). In this

regime, experimental data are concentrated in a narrow region, confirming the independence of dispersion on the diffusional behaviour of the system.

2.4 RTD in microfluidics

Internal diameters of microchannels range from tens to a thousand of microns, while the operative flowrates are up to a few milliliters per minute. As a consequence the flow in microfluidic devices is laminar. Accordingly, the cross-sectional velocity profile is parabolic along the whole length of a straight channel. Elements of fluid near the walls experience low local velocities, whereas the velocity of the material in the centre region is as large as twice the mean velocity. This velocity gradient leads to dispersion along the channel, i.e. elements of fluid entering at the same time into the channel reside in it for different times. We refer to this contribution as laminar or convective dispersion. The driving mechanism of mixing is molecular diffusion, which (as discussed in section 2.2.4) plays a role in the hydrodynamic dispersion. As a result, RTD studies on microchannels, in particular when they are used for chemical reaction or synthesis, assume crucial importance for their optimal design.

In recent years, there has been an increasing amount of literature on this topic. Both numerical and experimental studies have been conducted to characterize the hydrodynamics of microchannel devices. In this section we will focus on the experimental procedures proposed and the observed evidence. Note that a significant number of studies refer to multiphase flow in microchannels, in particular two-phase segmented flow. In addition to typical applications, such as interface reaction, this type of flow is adopted to reduce the hydrodynamic dispersion in microfluidics. Although in most cases the experimental procedures used to study the RTDs are similar and completely interchangeable, we prefer to treat in two different subsections the single-phase and multi-phase studies. In conclusion, the mean objective of this literature survey is to review the experimental setup as well as modelling technique adopted to perform RTD experiments on microfluidic devices. This will help us to develop our own methods of analysis. We also report the most significant results in this field to use as a reference.

2.4.1 Single-phase studies

One of the first experimental works in the field was proposed by Günther, M et al. (2004). They developed a method for measuring RTDs in microreactors using a flow-cell for the detection of the concentration of a dye (malachite-green) adopted as tracer. The detection was based on light absorption. Two different light sources were investigated: the TELUX$_{TM}$-LED appeared to work better than an ordinary LED in terms of signal-to-noise ratio. A T-piece like injector was used for the introduction of the tracer. The experimental setup was tested using a PTFE tube with an inner diameter of 0.5 mm. Pulse experiments were carried out and the non-perfect pulse injection was corrected with a procedure involving convolution-deconvolution with the axial dispersion model (ADM) as fitting model. Nevertheless, the inlet signal was not taken simultaneously with the outlet detection but only once for each flow rate investigated. The testing work showed that the fitting with the ADM, although not perfect, was acceptable. The measured curves are slightly asymmetric due to the tail arising from the laminar flow pattern. The authors proposed to improve the setup both adding a detection unit at the inlet and using a different flow model for the fitting procedure.

Some of the proposed improvements were later introduced in the setup of Bošković and Loebbecke (2008). The measurements were carried out by monitoring spectroscopically the concentration of a dye at both the inlet and outlet of three different micromixers. The tracer was injected into the carrier fluid with a HPLC valve. The experimental setup was developed to investigate different microchannel designs. For this reason the injection and the outlet detection were designed to be placed externally using tubing connections. They used the Semi-Empirical Model (Ham and Platzer, 2004) as well as the ADM for the convolution-deconvolution procedure. It was shown that the former better mimics the flow behaviour in terms of the shape of RTD in microreactors. This result is more evident for higher flow rates. A comparison between direct deconvolution and convolution-deconvolution (referred to as time-domain fitting) was conducted: the former, significantly affected by numerical noise, was used to validate the curve obtained via fitting (Figure 2.6). Additionally they observed the RTD approaching a narrower and more symmetric shape when working with higher flowrates, for all the microreactors studied. In a later study a similar setup

was adopted to compare the hydrodynamics of different microfluidic mixing structures (Bošković et al., 2011). They conducted a specific study to address the affinity of different dyes to TEFLON capillaries used for connections. They found the Basic Blue 3 to show no interaction with the walls of PTFE and PFA capillaries.

Adeosun and Lawal (2009) carried out pulse experiments in a T-junction and measured the RTD curve by means of UV-vis absorption spectroscopy. Again the convolution-deconvolution technique was necessary to take into account the spreading of the tracer in the section between the injection and the inlet boundary. It was found that the semi-empirical model better fits the experimental curve when compared with the ADM.

Lohse et al. (2008) presented a novel and non-instrusive method for determining the RTD in microreactors. It is based on the introduction of a tracer which is a non-fluorescent precursor dye. At the inlet the flow medium with the tracer is exposed to a pulse or a step signal of UV-light and so the dye is activated turning into a detectable tracer. In this way either a perfect pulse or step input can be achieved and hence there is no need to deconvolute the outlet time-response. Two standard injection procedures are investigated as benchmark: pressure induced injection (in a T-shaped junction) and

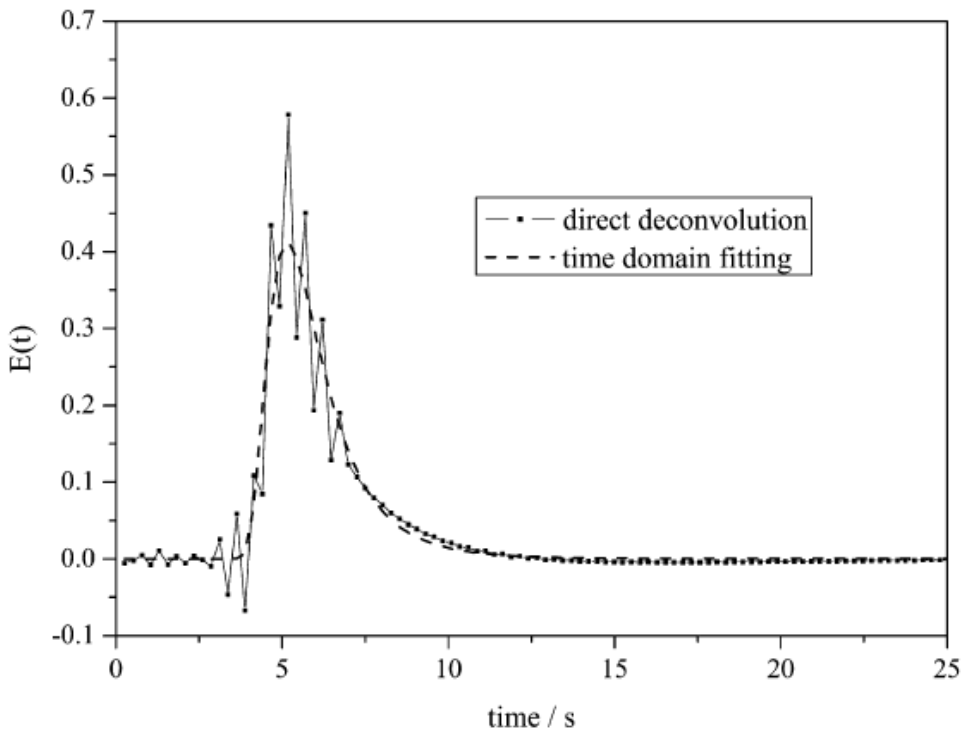

Figure 2.6 - Comparison of time domain fitting and direct deconvolution for an RTD measurement (Bošković and Loebbecke, 2008).

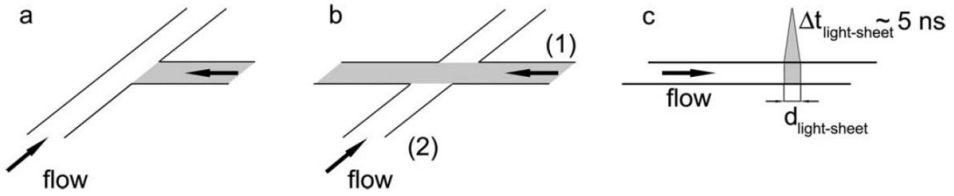

Figure 2.7 - Schematics of different tracer injections: (a) pressure induced in T-junction; (b) injection into stagnant in X-shaped junction; (c) novel technique (Lohse et al., 2008)

injection into stagnant fluid (X-shaped), as showed in Figure 2.7. In the T-junction, a steady-state flow was achieved in the main channel and then a small volume of tracer was injected pressure-wise from the side channel. In the x-shaped configuration the tracer was introduced into stagnant carrier fluid, whose flow was then restarted. Lohse et al. (2008) demonstrated the advantages of using the non-intrusive injection in terms of homogeneity of concentration across the channel at the inlet, possibility of fulfilling mixing-cup detection and the accuracy of measured RTD curves, which do not need further numerical manipulation. However, this injection technique requires sophisticated equipment and needs to be specifically designed for the microfluidic system to be intvestigated. This makes it impractical if one is to develop a flexible setup.

The experimental setup of Cantu-Perez et al. (2011, 2010) was characterized by on-chip detection by means of a linear diode array detector. Pulse injections of tracer (Parker Blue dye) were fulfilled with a 6-port sample injection valve. In this way the tracer was introduced homogeneously over the cross section of the channel. Nevertheless, the deconvolution was necessary because of the spreading of tracer in the inlet section. A direct deconvolution by means of Fast Fourier Transform was performed with the aid of signal filters and curve smoothing to avoid problem related to the noise of signal. They found a good agreement between the analytical and experimental curves.

2.4.2 Segmented flow studies

One of the solutions adopted to reduce the hydrodynamic dispersion in microchannels relies on the introduction of an immiscible phase. The main flow is fragmented in

small segments separated one from the other by the auxiliary phase. For this reason we refer to such a type of flow as segmented flow. This was first observed and characterized by Taylor (1960) half a century ago at the macroscopic level, but his observations still represent the fundamentals of this branch of multiphase flow.

Ideally, the segmented flow can be seen as a train of small batch reactors passing through a pipe or a small channel, separated one from the other. However, it is not so easy to avoid completely the connection between the liquid slugs as these may coalesce. Also, depending on the properties of the material channels and, surely, of the flowing material (i.e. density, surface tension) there will be a more or less thin film of fluid wetting the walls of the channels (Figure 2.8). Furthermore, when the cross section of the channel is rectangular or, in general, exhibits sharp corners, the presence of menisci is an additional contribution to mixing between slugs, hence to axial dispersion. Ultimately, the specific design and properties of the channel (dimensions, wettability, etc.) together with the operating conditions (e.g. flow rate, gas-to-liquid ratio) play a crucial role on the extent of dispersion. The effect of these variables has been investigated in the last years by means of RTD experiments.

Günther, A et al. (2004) used micro particle image velocimetry (µPIV) and fluorescent microscopy techniques to characterize the behaviour of segmented gas-liquid flow in both straight and meandering channels. They also compared the RTD of the meandering channel with the one obtained without feeding the gas (single-phase). A new technique for the injection of the tracer was presented. They attached a piezoelectric disk to the chip, in particular, on top of the tracer reservoir and applied a

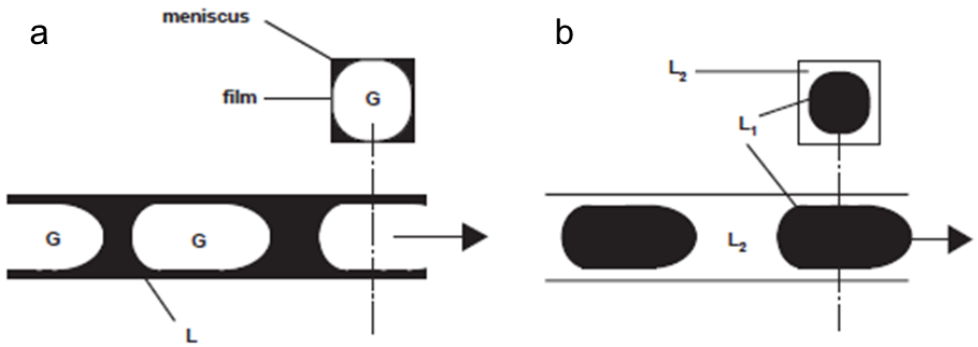

Figure 2.8 - Schematic example of segmented flow in rectangular channels: gas-liquid with aqueous liquid phase and hydrophilic walls (a); liq-liq segmented flow with L2 organic liquid and hydrophobic walls (Trachsel et al., 2005).

direct current voltage to it. This would bend the disk pushing tracer to move from the reservoir to the channel and, hence, producing a pulse input of tracer (Figure 2.9). Rhodamine-B was used as tracer and detected by through-the-wall procedures. It was observed that the multiphase flow narrows down the residence time distribution as compared to the single-phase in the same channel.

Trachsel et al. (2005) studied the gas-liquid segmented flow in PDMS microchannels with hydrophilic walls. Similarly, they used the aforementioned on-chip piezoelectric injector and showed its capability of achieving sharp pulse input. The ADM was adopted as fitting model for the convolution-deconvolution procedure. The RTD curves obtained with deconvolution were in perfect agreement with the measured ones. This clearly proves the accuracy of the embedded injection method. Again, the variance of the RTD in segmented flow is smaller as compared to the one measured for single-phase experiments.

A way to positively affect the RTD in rectangular microchannel is the optimal tuning of the ratio of liquid-to-gas flowrate ($\dot{v}_l\ /\dot{v}_g$), as discovered by Kreutzer et al. (2008). They studied the effect of operative conditions of gas-liquid segmented flow on the broadening of the residence time distribution in a PDMS microchip. It was found that the influence of $\dot{v}_l\ /\dot{v}_g$ is stronger than the flowrate itself. However, for smaller residence time (i.e. increasing $\dot{v}_l$ keeping constant $\dot{v}_l\ /\dot{v}_g$) the width of the distribution is narrower.

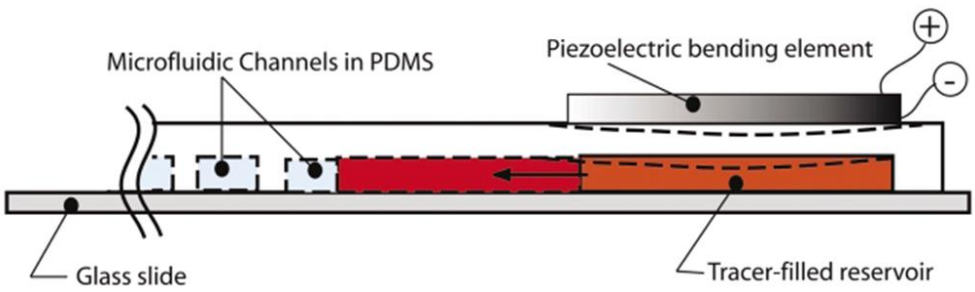

Figure 2.9 - Cross- section schematic view of the device for the piezoeletctrically induced injection of tracer (A. Günther et al., 2004).

2.5 Secondary flow to reduce axial dispersion

Flows in tridimensional domains comprise two contributions: a *primary flow* occurring parallel to the main direction of the fluid motion and a *secondary flow* acting perpendicularly to this. Secondary flows arise from drag effects in proximity of wall surfaces. Examples of secondary flows can be observed in curved pipes and in spinning fluid, e.g. the tea cup experiment (Taylor, 1968).

Secondary flow in curved pipes was firstly theorized by Dean who investigated the flow in helically coiled circular tubes (Dean, 1928, 1927). The dimensionless group used to characterize this flow behaviour, encountered in helically coiled tubes, is called Dean number:

$$De = \frac{Re}{\lambda^{0.5}} = \frac{\rho u d_t}{\mu}\sqrt{\frac{d_t}{D_c}} \qquad \text{Eq. 2.38}$$

where λ is the ratio of the diameter of curvature (or equivalently the diameter of the coil D_c) to the diameter of the tube (d_t), ρ and μ respectively the density and dynamic viscosity of the fluid and u the mean axial velocity. We refer to λ as coil-to-tube diameter ratio. We can give to De a physical interpretation in terms of the balance of forces due to inertia and centrifugal acceleration and the viscous forces. Let us rearrange the terms as follows:

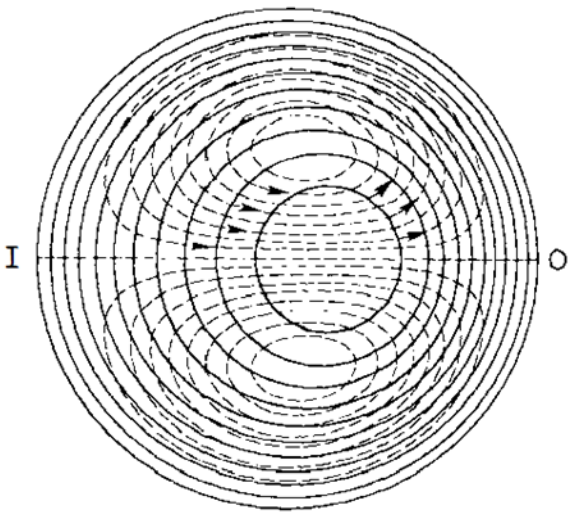

Figure 2.10 - Contours of axial velocity of curved pipes at low Dean number (continuous line) and streamline of flow in transverse direction (dashed line). (Berger et al., 1983)

$$De = \frac{\sqrt{\rho \frac{u^2}{\lambda}\ \rho u^2}}{\mu u / d_t} \propto \frac{\sqrt{(centrifugal\ force) x (inertial\ force)}}{(viscous\ force)} \qquad \text{Eq. 2.39}$$

In the above we have rearranged the terms so that $\rho \frac{u^2}{\lambda}$ is a measure of the centrifugal force, ρu^2 represents the momentum flux (and it is conceptually related to inertia) and $\mu u / d_t$ is an estimate of the wall shear stress (viscous force). As a result, for small Dean numbers ($De \ll 1$), viscous forces are dominant and the secondary flow is absent. Conversely, as De increases centrifugal and inertial forces prevail over drag leading to the development of a secondary flow. The Dean number expresses the magnitude of secondary flow in curved pipes and helically coiled tubes.

In his pioneering work, Dean obtained the analytical solution to equation of motion in the case of incompressible laminar flow and small curvatures (high λ). The non-dimensional solution depends exclusively on De. The action of centrifugal force due to the curvature of the tube generates two counter-rotating vortices, which in turn promote transverse (or secondary) mixing. The centrifugal force acts strongly on the fluid that is moving near the centre of the tube or channel, where the axial velocity is greatest. The fast moving fluid is forced to move outward and is continuously replaced by fluid moving inward from regions near the wall. For this reason the maximum of axial velocity is shifted toward the outer wall (Figure 2.10).

2.5.1 Helically coiled tubes (HCTs)

The presence of radial mixing contributes to the reduction of hydrodynamic dispersion (i.e. narrower RTDs). Many works, both theoretical and experimental, have been devoted to the study of these effects in HCTs. Ruthven (1971) calculated the RTD under the range of applicability of Dean's solution and diffusion-free conditions ($De < 17$). He found that the RTD does not depend on the curvature ratio and, although qualitatively similar, it is narrower than that of a straight tube. However, Ruthven's results were restricted to high coil-to-tube diameter ratios (for Dean's solution to be

applicable). These observations were partially validated by the experimental work of Trivedi and Vasudeva (1974). Step input experiments were performed on coiled tubes. For De up to 6, experimental RTDs were found to match reliably Ruthven's results. However this was not the case for higher Dean numbers and the authors proposed a restriction on the range of applicability of Ruthven's RTD. Few years later Nauman (1977) conducted a more detailed theoretical study on diffusion-free RTDs in helical coils. He proposed a corrected version of the RTD, showing some errors in the previous works. Both theoretical and experimental studies demonstrate that narrower RTDs can be obtained in HCTs as compared to straight pipes under conditions of negligible diffusion.

The first experimental study on RTDs of HCTs under significant molecular diffusion was published by Trivedi and Vasudeva (1975). In this work, a wide range of geometric and operative parameters was investigated by means of step input experiments. They adopted the axial dispersion model to match the measured *F* curve (cumulative distribution) with analytical solution RTDs of the model and therefore quantify the extent of axial dispersion. The matching resorts to best curve fitting of the experimental curves with the theoretical ones. They also proposed a correlation to verify the conditions of applicability of the axial dispersion model in helically coiled tubes:

$$\tau_{ADM} = \frac{\bar{t}}{d_t^2 / 4D_m} > 6/Re \qquad \text{Eq. 2.40}$$

valid for $0 < \lambda < 280$ and $Re < 1000$, where $\bar{t}$ is the mean residence time, d_t is the internal diameter of the pipe and D_m the molecular diffusion coefficient. The first term on the left hand side of Eq. 2.40 represents the ratio of the characteristic time for convection and radial transport by diffusion. It can be verified that the conditions under which the axial dispersion model can be applied are less strict in HCTs than straight tubes over the range investigated. For straight tubes Anthakrishnan et al. (1965) calculated that $\tau_{ADM} > 0.8$ is the condition for the applicability of the model. Differently from straight tubes, where the only transport mechanism in radial direction is diffusion, in helically coiled tubes convection plays a significant role, as effect of Dean roll-cells, in homogenizing the concentration of tracer over the cross-section. As

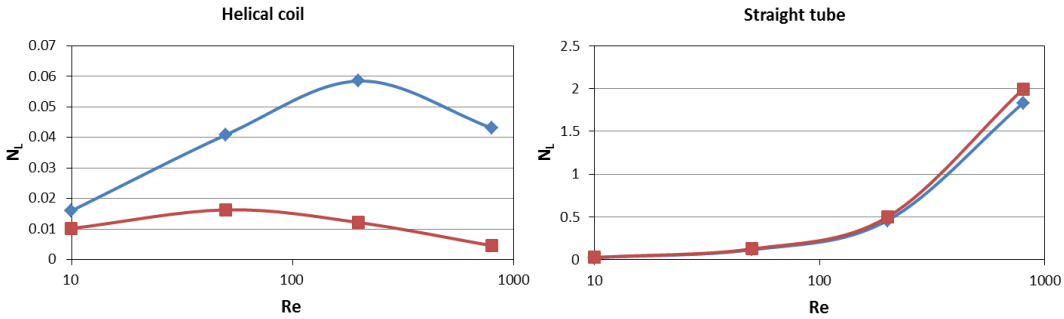

Figure 2.11 - Axial dispersion number against Reynolds number for helical coils (blue λ=280, red λ =15.6) and straight tube (colours according to respective length of HCT). (Trivedi and Vasudeva, 1975)

a result, depending on Re (and in turn on the magnitude of secondary flow) the applicability of ADM is extended.

Trivedi and Vasudeva (1975) reported the values of the ratio ud_t/D_{ax}, which they refer to as *effective Bodenstein number* (the inverse of $N_d$defined in section 2.3), for different Reynolds number. It was not observed a clear correlation between the two quantities. A different way to analyze dispersion under significant molecular diffusion, suggested by Erdogan and Chatwin (1967), was also adopted: $K = D_{ax}D_m/u^2d_t^2$ was plotted as a function of Re. Depending both on Re and λ the variation of K ranged between 2 to 7-fold. The values of K against De lie on a single curve for different coil-to-tube diameter ratios. This result is in agreement with Dean's work, who found that the flow field is defined exclusively by De for small values of De or large λ. The comparison between the vessel dispersion number (N_L) of straight channel and helical coils was reported for two coil-to-tube diameter ratios as a function of Re. The axial dispersion number reduces significantly when coiling the tube, the reduction being higher for smaller λ (Figure 2.11). For straight tubes vessel dispersion numbers increase monotonically with Reynolds and reach a maximum in correspondence with the transition to turbulence. The trend reported for HCTs presents a maximum, which is shifted toward higher Reynolds when the coil-to-tube diameter ratio is greater. This result is surprising, as the presence of a maximum implies that there exists a value of Re for which a change in the dispersive behaviour occurs. The authors did not provide a sufficient physical explanation to these observations.

Janssen (1976) investigated numerically the effect of coiling on longitudinal dispersion. In this work, the ratio between the dispersion coefficient of helical coils

and that of straight tubes is presented as a function of the dimensionless number De^2Sc, which is used to discriminate between dispersion and diffusion processes. If De^2Sc is less than 100, molecular diffusion dominates and longitudinal dispersion is comparable with that of straight tubes. For higher values, the effect of secondary flows is enhanced resulting in a reduction of the dispersion coefficient. They predicted that a continuous reduction of axial dispersion coefficient is expected using Dean's solution for De up to 17. Similar results were also reported in the work of Johnson and Kamm (1986). They used *Monte-Carlo* simulations to calculate the solution of the dispersion equation in helical coils and showed the relationship between dispersion coefficient and De^2Sc. Theoretical work did not confirm experimental observations of Trivedi and Vasudeva (1975); however, numerical works were limited to the applicability of Dean's solution.

Few years later, Castelain et al. (1997) conducted an experimental study on the axial dispersion of helical coils built by assembling 90 degree stainless steel elbows. The concentration of the injected tracer was measured over time both at the inlet and the outlet by means of conductivity meters. They adopted the axial dispersion model together with a fitting procedure based on the minimization of least squares of a function written to include the Fourier series of the detected curves and the transfer function of the model. Two fitting parameters were estimated: $\bar{t}$ and $1/N_L$. They carried out experiments at high values of Reynolds numbers in both laminar and fully turbulent regime. They reported that the transition between laminar and turbulent regime is smoother and delayed in helical coils ($8000 < N_{Re} < 1000$) as compared

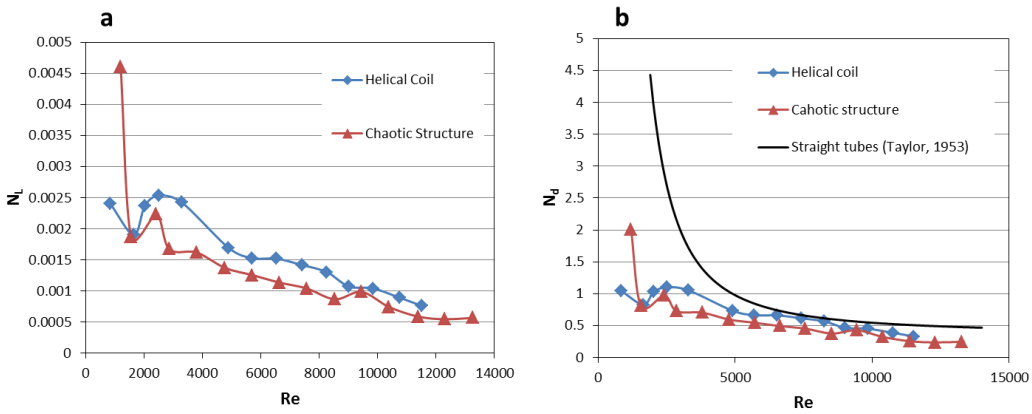

Figure 2.12 – Experiments in HCTs and twisted pipes: (a) Axial dispersion number against Reynolds number; (b) Dispersion number based on internal diameter against Reynolds number (Castelain et al., 1997).

to straight tubes ($N_{Re} \approx 2800$). The values of $1/N_L$ decreased with Re and were in good agreement with the theoretical prediction of Taylor (1953) for straight tubes (Figure 2.12). The agreement improved at higher degree of turbulence. This is an indication that the effect of coiling on dispersion vanishes as the flow becomes more and more turbulent. Therefore, the reduction of axial dispersion promoted by secondary flow in helical coils as compared to straight tubes is significant primarily in laminar flow.

2.5.2 Coil flow inverters (CFIs)

Saxena and Nigam (1984) firstly proposed flow inversions in helically coiled tubes to further narrow the RTD. By introducing bends on HTCs they observed an improvement of hydrodynamic dispersion under both diffusion-free conditions (fully convective regime) and significant molecular diffusion as compared with a straight helical coils (Figure 2.13). Specifically, they showed that a sudden shift of the direction of action of centrifugal force (always perpendicular to the axis of the coil) is more effective than a gradual rotation, which can be achieved by coiling a helical coil. The experimental procedure adopted was described in detail in a previous work (Trivedi and Vasudeva, 1974). It resorts to step input experiments achieved by simply switching the carrier fluid to a tracer solutions (Congo red dye). The working fluid is a solution of water and diethylene glycol (DEG), the concentration of which is varied to change the Schmidt number and in turn the diffusional behaviour of the system.

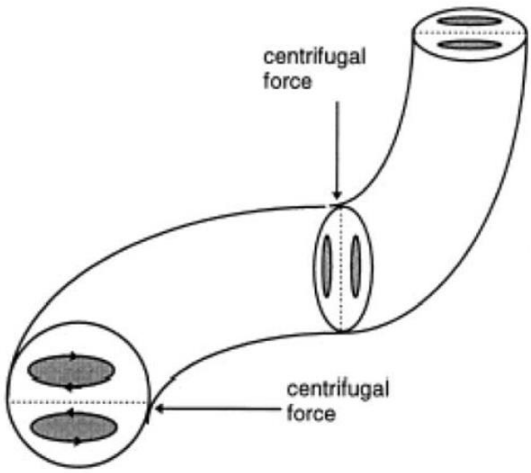

Figure 2.13 - Drawing of 90 degree bend and shift of Dean-roll cells (Castelain et al., 1997).

They measured the optical density of the exiting fluid and since there was a linear relationship between density and concentration of tracer, no further processing was needed to obtain the *F* curve.

Under diffusion-free conditions (80% aqueous solution of DEG) they studied the effect of the positions of a single 90 degree bend along the coil, the angle of a single bend located centrally and the overall number of bends. By varying the length of the coil before and after the bend, they observed that the inverter was most effective in reducing axial dispersion when the bend was placed in the centre. Therefore, coiled flow inverters should be constructed keeping constant the number of coils on each arm, or to say it differently, each bend must be equally spaced along the inverter. A 90-degree angle maximizes the effect of the inversion as it produces a complete inversion of the direction of action of the centrifugal force. Increasing the number of bends, they observed a continuous narrowing down of the RTD. However, for $n_{bends} < 7$ the difference with the RTD of a straight helix is minor. For the highest number of bends investigated ($n_{bends} = 57$) the dimensionless time ($\vartheta = t/\bar{t}$) at which the first element of fluid reaches the outlet was 0.85 as compared with 0.5 for a straight channel and 0.6 for a straight helix. This suggests that the RTDs are significantly narrower when increasing the number of bends. The maximum number of bends was constraint by a

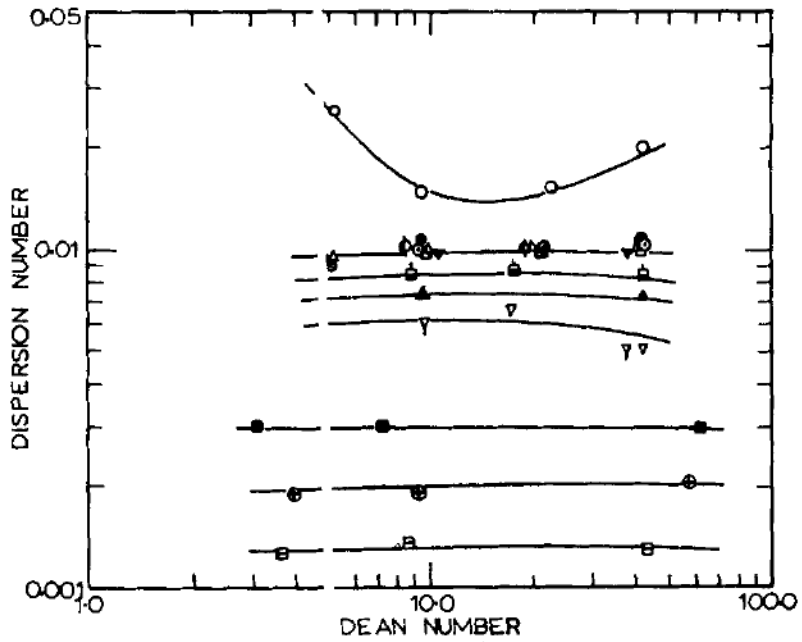

Figure 2.14 - Axial dispersion number against Dean number reported by (Saxena and Nigam, 1984)

minimum number of coils for each arm to ensure a fully developed secondary flow, for a fixed total length of the tube. In this study the maximum number of bends was obtained with 5 turns on each arm. In the case of negligible diffusion they studied the effect of Dean number on RTDs. For a straight helix the diffusion-free RTD does not change when De is increased above 1.5. When introducing flow inversions this threshold parameter is higher: in an inverter with 15 bends for $De > 3.0$ they observed a unique RTD. The narrowing of the residence time is due to flattening of velocity profile in the transverse direction. Two mechanisms contribute to this end: (a) secondary flow (b) interchanging of velocity between elements of fluids at the bends. Both mechanisms are active for $De < 1.5$ because the secondary flow is not still completely developed. For $1.5 < De < 3$ the secondary flow is fully developed (i.e. does not change as De increases) and the interchange of fluid elements with different residence time (not dependent on De) further narrows down the RTD.

In case of significant molecular diffusion the experimental *F* curves were fitted with the analytical expression of Taylor's axial dispersion model. The curve fitting was used to estimate the axial dispersion coefficient. Vessel dispersion numbers appear to be independent of Dean numbers in coiled flow inverters (Figure 2.14). The values of N_L were reported also for HCT: the correlation with Dean number showed a minimum, which is in contrast with the work of Trivedi & Vasudeva (1975). As the number of inversions increases the overall axial dispersion reduces. In this work a correlation for dispersion numbers holding for coiled flow inverter having equispaced 90 degree bends was proposed:

$$N_L = 0.016\left(\frac{1}{n_{bends}+1}\right)^{0.58} \qquad \text{Eq. 2.41}$$

To our knowledge this represents the only available correlation for axial dispersion in coiled flow inverters for single-phase liquid flow.

In more recent years CFIs have been studied under different perspectives: velocity flow field, mixing and heat transfer efficiency and hydrodynamic dispersion in gas-liquid flow. Although most of these aspects may not be directly related to the hydrodynamic dispersion in single-phase flow, we report key-results of such studies.

Kumar and Nigam (2005) studied velocity and temperature profiles in CFIs by means of computational fluid dynamics. Their analysis was mostly qualitative and aimed to demonstrate that the presence of bends (e.g. flow inversions) on helically coiled tubes generates a so-called alternating Dean flow. In this flow regime Dean roll cells (secondary flow vortices) rotate after each bend. After a 90-degree bend the Dean roll-cells regenerate on a perpendicular plane with respect to the previous one. Half linear length of a single coil is needed for the secondary flow to fully develop in a straight helix and the same length for the Dean vortices to regenerate after each bend, for the parameters investigated. Once fully developed, the transverse velocity profile both on horizontal (same direction as centrifugal force) and vertical centreline do not change with the number of bends. The change of orientation of Dean vortices enhances radial mixing and in turn flattens the radial temperature profile. They studied the effect of De on heat transfer of a 7 bend CFI and compared with a straight helix in terms of fully developed Nusselt number. In all cases they predicted the CFI to perform better than the helical coil without bends. In a later work, these numerical results were also supported by experiments on a heat exchanger designed as a CFI (Kumar et al., 2007).

Kumar and Nigam (2005) for the first time referred to flow inversions as geometrical perturbations leading to chaotic flow. In classic Dean flow the trajectories of flowing particles are regular; in other words each particle experiences always the same trajectory for a fixed initial condition. If a geometrical perturbation is introduced, such as a flow inversion with an angle $0° < \varphi < 180°$ the flow can become mixed or fully chaotic. A mixed flow is characterized by both regular and chaotic zones. This regime was firstly observed by Jones et al. (1989) in their numerical work on twisted pipes. Castelain et al. (1997) created chaotic advection structures by changing the relative angle between 90-degree elbows used also to construct helical coils. The chaotic system presented axial dispersion numbers smaller than the helical coil structure for $Re > 2500$ (Figure 2.12). The chaotic structures differ from coiled flow inverters because a fully developed secondary flow is never established before changing the direction of action of the centrifugal force.

Mridha and Nigam (2008) numerically investigated the mixing efficiency of CFIs by looking at concentration distributions in cross sectional planes. Their model resorts to the numerical solution of Navier-Stokes equations coupled with the species transport

equation in three dimensions. A virtual interface was set at the inlet cross section; in particular, it was orientated perpendicularly to the direction of secondary flow. The contours of axial velocities reveal in all cases (straight helix; CFI with one, two and three bends) a rotation with respect to the direction of action of the centrifugal force on the last arm of the structure. The authors explain this phenomenon as the effect of torsion, which is a rotational force generated by the existence of a finite axial pitch (e.g. distance between two successive coils). The comparison of concentration contours reveals that both the number of bends and the Reynolds number improve the mixing efficiency. Similar results were obtained in a later work using a different modelling approach (Mandal et al., 2011).

The liquid-phase hydrodynamics of gas-liquid flows in CFIs was studied by means of experimental RTD (Vashisth and Nigam, 2008). The experimental procedure used is similar to that adopted by Saxena and Nigam (1984): step input experiments and application of a flow model to obtain dispersion characteristics. A modified axial dispersion model was adopted: laminar flow model to account for liquid moving in the viscous sub-layer close to the walls of the channels and axial dispersion model for the portion of liquid moving close to the gas-phase. They observed that the liquid-phase dispersion can be reduced by increasing the Dean number, decreasing the axial pitch or the curvature ratio. These results are qualitatively similar to those observed for single-phase flows.

More recently CFIs have been employed as microreactors for polymerization processes. Mandal et al. (2010) performed CFD simulations to model the free-radical polymerization of styrene. They observed higher conversions and enhanced polymerization performances when using the CFI as compared with a straight channel reactor. They also found that the diffusional behaviour of the fluid affects the conversion, for the flow inversions are more effective for less viscous fluids. They proposed CFIs as efficient microreactors to be adopted in polymerization processes. Similarly, Parida et al. (2014) conducted experimental studies in CFIs and HCTs to highlight the effect of radial mixing on the synthesis of branched and linear polymers. It was observed that the control over the polymerization process, limited by increased viscosity at high conversions, could be improved in CFIs as compared to HCTs, confirming the numerical findings of Mandal et al. (2010).

2.5.3 Parameters affecting dispersion in CFIs

While the design of helically coiled tubes is relatively simple, many design parameters can affect the hydrodynamic dispersion in CFIs. Here a description of the geometrical parameters as well as the non-dimensional numbers involved is reported. Understanding their influence on the dispersive behaviour of CFIs is crucial to identify the optimal design in terms of minimization of axial dispersion. A schematic representation of a 90-degree bend characterizing CFIs is reported in Figure 2.15.

Number of bends (n_b). For a given length of helically coiled tube the number of bends can dramatically change the dispersive behaviour as effect of chaotic advection occurring at the bends. The Dean roll-cells induce regular patterns on the trajectory of fluid particles. Thus, portions of fluid are still prevented to mix with regions close to walls of the tubes, characterized by small axial velocity. Introducing geometrical disturbances, such as flow inversions by means of bends on helically coiled tubes, one can create chaotic advection and in turn disrupt the parabolic velocity profile. A

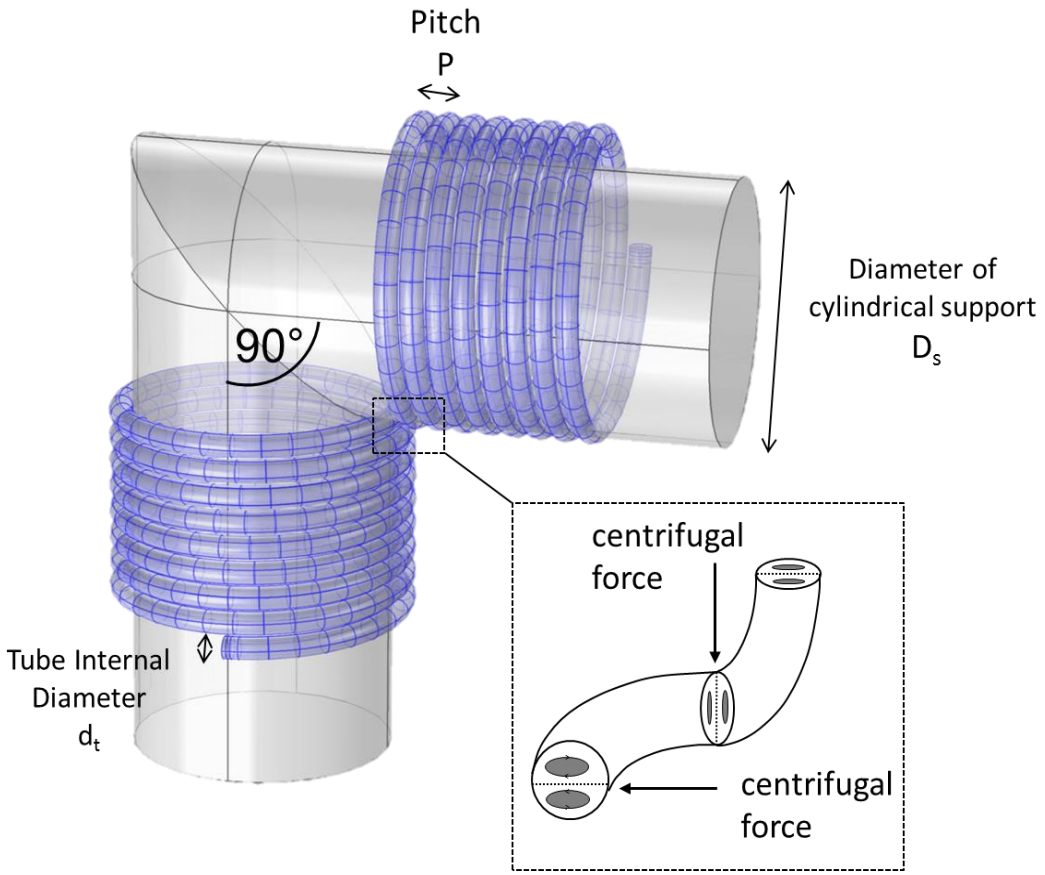

Figure 2.15 – Schematic representation of a 90-degree bend in a CFI. In this example each section of helical coil is characterized by n_t = 8.

continuous narrowing down of the RTD is observed when increasing the number of bends (Saxena and Nigam, 1984). The maximum number of bends is dictated by total numbers of turns. In theory one could construct a CFI with as many bends as the number of turns minus one; however, this can be very impractical and lead to very bulky structures.

Number of turns (n_t). The number of turns on each section of straight helical coil is clearly related to the number of bends that one can attain for a given length. A sufficient number of turns also is important to guarantee a fully developed secondary flow for the flow inversions to be most effective. The length necessary for a fully developed secondary flow depends on the coil-to-tube diameter ratio, axial pitch and the Reynolds number. In most cases the choice on the number of turns is dictated by geometrical constraints, such as the available length on the cylindrical structure.

Axial pitch (p). The distance between consecutive turns is called axial pitch and defines the effect of torsion on the secondary flow. Increasing the axial pitch, the effect of centrifugal force on the flow vanishes and the Dean roll-cells disappear, thus approaching the velocity profile of straight tubes. Note that, in the limiting case of infinite axial pitch, the presence of bends would create localized spots where the curvature induces the formation of secondary flow. However, this would not be able to fully develop, being actually poorly effective on the dispersion behaviour. As a result, the axial pitch must be as small as possible to maximize the reduction of axial dispersion.

Bend position. Bends must be located at regular intervals of helical coil section as observed by Saxena and Nigam (1984).

Bend angle and spatial orientation. The role of bends is to change the orientation of the Dean roll-cells in the cross section of the tubing. To this scope a 90-degree angle needs to be induced between two consecutive helical coil sections to maximize the change of orientation. The spatial orientation of this angle is not important and CFIs can be designed so that the axis of the cylindrical support lies on a plane. However, this would reduce the degree of compactness of the structure.

Coil-to-tube diameter ratio (λ). This dimensionless number defines the effect of centrifugal force on the flow. It is so defined:

$$\lambda = \frac{D_s + {d_t}/{2} + w}{d_t} = \frac{D_c}{d_t} \qquad \text{Eq. 2.42}$$

where D_s is the diameter of the cylindrical support, d_t is the internal diameter of the tube and w the wall thickness of the tube. Decreasing λ results in the centrifugal force being stronger as effect of the increased curvature of the tube. The coil-to-tube diameter ratio is a crucial design parameter; however, the studies devoted to its effect on the hydrodynamics are limited, particularly on CFIs.

Reynolds number ($\boldsymbol{Re} = \frac{\boldsymbol{\rho u d_t}}{\boldsymbol{\mu}}$). The beneficial effects of secondary flow on the reduction of axial dispersion are attractive only in the laminar flow regime. In this regime the dispersion behaviour of coiled tubes as a function of the Reynolds number appears to be qualitatively different as compared to that in straight tubes.

Dean number ($\boldsymbol{De = Re\lambda^{-0.5}}$). As discussed above the Dean number expresses the balance between inertial, centrifugal and viscous forces. As De becomes less than unity, viscous forces become dominant and the effect of centrifugal force vanishes. There exists a critical value of Dean number (or Reynolds number for any fixed λ) above which the effect of secondary flow enhances the reduction of axial dispersion. However, data in the literature do not identify univocally this value.

Chapter 3

Development of an experimental platform to measure RTDs in microfluidic devices

3.1 Introduction

In this chapter, the work done to develop an experimental procedure to study RTDs in microfluidic devices. Our aim is to design a flexible and reliable platform to measure RTDs of microfluidic devices, both for chip-based and capillary systems. In a first stage, the detection system was built using inexpensive in-house made sensors and flow cells. The system was tested performing experiments in capillary tubes. In a second stage, a more reliable and flexible platform was designed, relying on commercial spectrometers. Optical detection is the most adopted technique for RTD experiments in microfluidics. The reduced optical path-lengths and visual transparency that often characterize microfluidic devices make it also the most practical approach. The choice made for the development of our own experimental setup relies on absorbance measurements. It is therefore useful to discuss the conditions under which absorption-based detection can be employed to accurately determine the concentration of a tracer as part of RTD measurements.

3.2 RTD system with in-house made sensor

Several solutions have been proposed to develop RTD detection system for microfluidic devices, as discussed in section 2.4. However, a standard procedure has not been established. The majority of experimental setups are designed to carry out measurements on specific devices; this is particularly the case for compact chip structures. Furthermore, sophisticated techniques for the injection of tracer may be complex to implement. We aim to develop a system allowing to conduct measurements

on different microchannel devices using standard injection techniques. In this section, the work performed to develop both experimental and post-processing procedures using inexpensive in-house made detectors is discussed.

3.2.1 Description of the detection system

In-house made detectors based on through-the-wall light absorption were employed (Alexoff et al., 1995). An infrared light LED (880 nm) and a photodiode were placed in opposite ends of a 1/8" PEEK cross (Upchurch), while the other two ports were drilled out to let the TEFLON capillary pass through (Figure 3.1).

The photodiode detects light only in the infrared wavelength region: variations of external light reaching the photodiode do not affect the signal. The light generated by the LED travels through the wall of the capillary, through the fluid inside the tube, again through the wall of the tube before reaching the photodiode. The photons hit the latter producing a voltage signal that is generated and collected with the aid of an acquisition card (NI USB-6008) connected to a computer. The signal produced depends on the intensity of light reaching the photodiode, which in turn is a function of both the intensity of light emitted by the LED and of tubing materials as well as the fluid flowing in it. Standard PFA or PTFE tubing were used, for this materials present better transmission of light compared to other TEFLON-based tubing. This allows

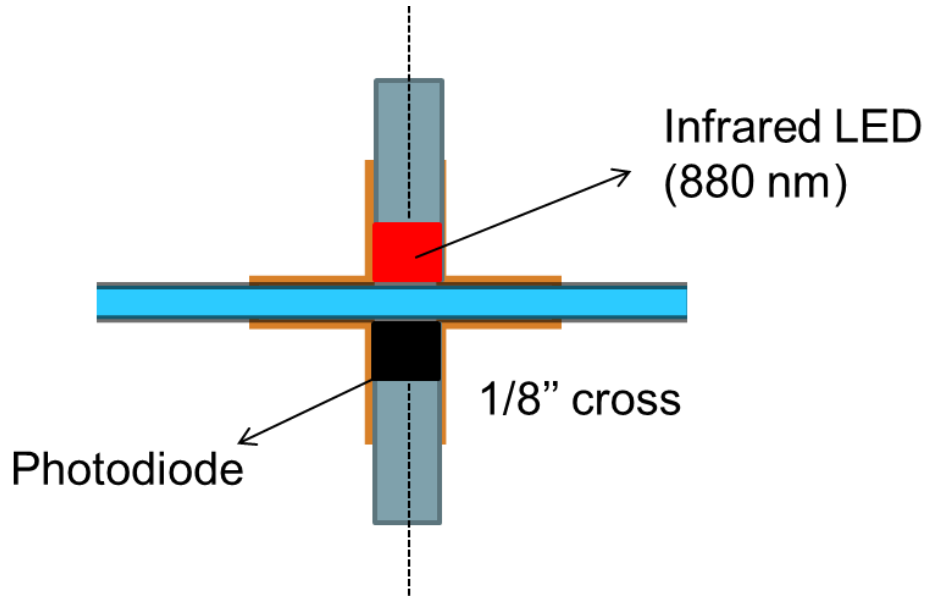

Figure 3.1 - Simplified schematic of the section of the in-house made sensor.

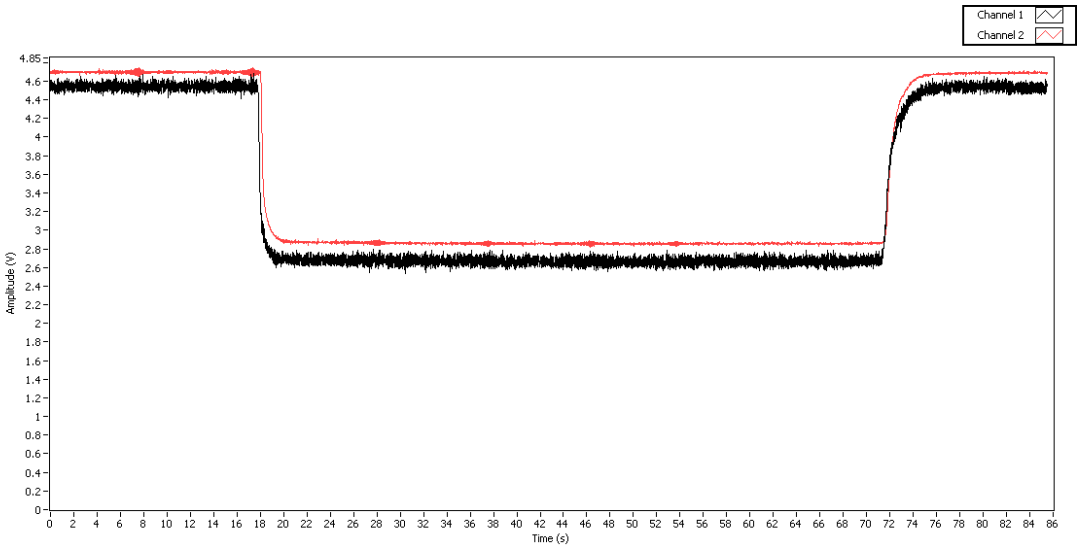

Figure 3.2 - Example of time-series data. Here Channel 1 and 2 refer to Sensor 1 (S1) and Sensor 2 (S2) respectively.

higher fractions of light to reach the photodiode, resulting in higher signal-to-noise ratio. It should be noted that the signal is not smooth. Due mostly to the acquisition apparatus, a noisy signal was collected. Two sensors were built to perform measurements with two detection points at the same time. However, from the example of raw signal reported in Figure 3.2 it can be seen that the sensors behave differently in terms of noise, because of intrinsic manufacturing differences.

Copper sulphate was adopted as tracer, as its absorption spectrum shows a maximum in the infrared region. This is an electrolyte soluble in water (S = 32 g $CuSO_4$ / 100 g H_2O at 20 °C). Note that the choice of this tracer was dictated by the characteristic emission/absorption wavelength chosen for our sensors. It is in fact not easy to find tracer absorbing in the infrared region and, at the same time, being characterized by flow properties suitable for aqueous systems.

The main advantage of the system proposed is the possibility of using the sensors in a flexible way. Measurements take place through the walls of capillaries adopted for standard connections in microfluidics. This allows to easily place the sensors close to the boundaries of the device to investigate and in turn perform reliable measurements. On the other hand, our detectors are not as much flexible in terms of the choice of tracer. If for any reasons one has to change tracer both the photodiode and the emitting light need to be replaced according to the absorbance peak of the new tracer. Note that,

when working with detectors active in the visible, one is to make sure that the detection cell does not permeate ambient light. This can be achieved by changing the material of the optical cell or sealing with suitable material the available cell.

3.2.2 Absorbance calibration

The response of the sensors to different concentrations of tracer is discussed in this section. Note that calibration is very important as the validity of the Lambert-Beer law needs to be verified (see 2.2.6).

The voltage signal (V) generated by the infrared photodiode is directly proportional to the intensity of light (I). Eq. 2.28 can be rewritten:

$$A = -\log {}^{V}/_{V_{c=0}} = \gamma c \qquad \text{Eq. 3.1}$$

where $\gamma = \epsilon l$ is so defined because the length between the light source (LED) and the detector is fixed. A series of calibration experiments were carried out to establish the region of validity of the Lambert-Beer law. Solutions of $CuSO_4$ ranging between 0.01 and 1.2 M were sampled. The reference signal ($V_{c=0}$) was recorded for each sensor pumping deionized water through the capillary in the setup showed in Figure 3.3. The sensors were secured to the working bench as any accidental movement of the cables would change the incident light and in turn affect the measurements. The capillary was secured using ferrules on both sides of the cross.

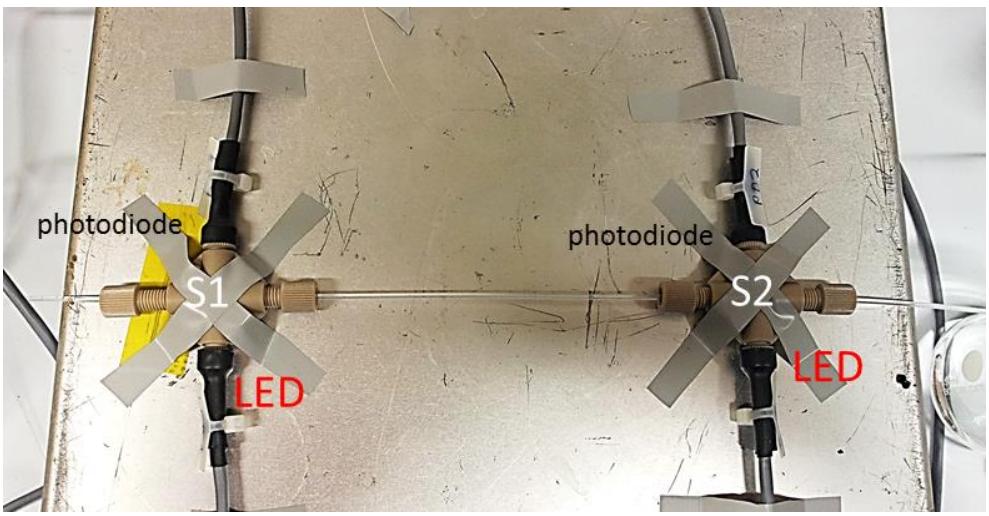

Figure 3.3 - Setup used for the calibration of the sensor.

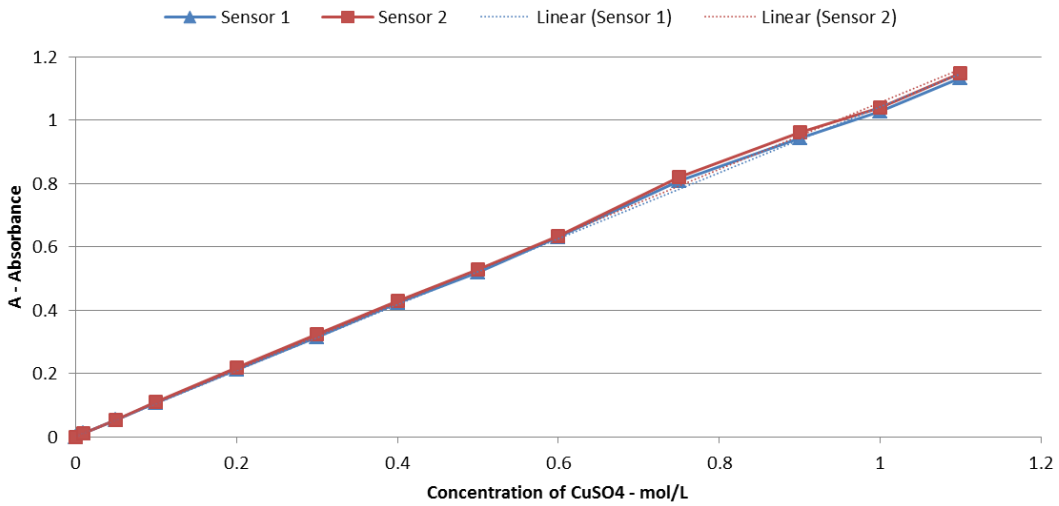

Figure 3.4 - Absorbance curve and linear fit for both sensors.

Figure 3.4 shows the plot of absorbance against concentration. It can be clearly observed a linear trend for concentration up to 0.5 M. The line intercepts the origin confirming the assumptions of section 2.2.6. Above this value, although still reasonably on a straight line, data appear more scattered. We can also observe that the slopes of the curves are slightly different between the two sensors. A given concentration of copper sulphate would generate slightly different absorbance measurements.

As a result of our calibration experiments, tracer concentrations below 0.5 M must be adopted to work under validity of the Lambert-Beer law. Despite so, different absorbance measurement are produced by the two sensors. For this reason, a calibration must be carried out before experiments to determine γ, so that from the absorbance measurement one can calculate back the dye concentration:

$$C = \frac{A}{\gamma} \qquad \text{Eq. 3.2}$$

where we use capital letter for calculated concentrations.

3.2.3 RTD data post-processing

In this section the analysis procedure to obtain the RTD from time-series data generated from the sensor is described in detail. A MATLAB script was developed to

acquire the signal data and perform the analysis so as to derive the RTD. The script was written specifically to perform step input experiments.

Firstly, data from the sensor are generated in a *txt* file, which is then converted into a data matrix. The acquisition process generates data aliasing. For this reason, a piece of code was written to remove duplicates. It is necessary before starting the analysis procedure to insert input values for the injection time (the time at which the injection starts) if different from zero and the acquisition frequency. The acquisition frequency cannot be higher than that at which the voltage signal was taken. A plot of $V(t)$ is automatically generated (example in Figure 3.5). Observing this plot the user can insert time ranges to calculate $V_{c=0}$ (reference signal) and $V_{c_{max}}$ (calibration signal). The latter is the signal when tracer solution at the selected concentration flows. When using tracer solutions below 0.5 M the linear relationship between absorbance and concentration allows performing a calibration with just two points:

$$\overline{\gamma} = \frac{-\log(V_{c_{max}} / V_{c=0})}{c_{max}} \qquad \text{Eq. 3.3}$$

The reference signal is then used to calculate the transmission ratio ($T(t)$) and in turn the absorbance ($A(t)$). A signal smoothing algorithm is applied to the raw signal in order to reduce the noise. This is a simple algorithm averaging data over a number of points, which can be chosen by the user. The averaging number of points must be large

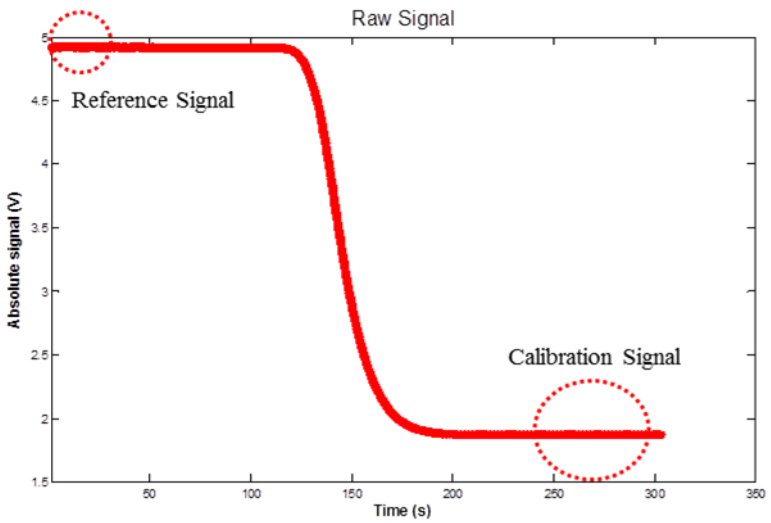

Figure 3.5 - Example of plot of V against time used for direct calibration.

enough for the smoothing to be effective, but small compared to the time scale characterizing the RTD rate of change. The time-range moving window for the smoothing is to be chosen carefully to avoid significant alterations of the curve.

Using the calibration parameter the concentration curve can be retrieved:

$$C(t) = \frac{-\log(V(t)/V_{c=0})}{\overline{\gamma}} = \frac{A(t)}{\overline{\gamma}} \qquad \text{Eq. 3.4}$$

At this point $C(t)$ corresponds to $C_{step}(t)$ that we defined in 2.2.2. Normalization is needed to obtain the F curve. The residence time distribution function is calculated by numerical differentiation, using a finite forward-difference method:

$$E(t_i) = \frac{\Delta F}{\Delta t} = \frac{F(t_{i+1}) - F(t_i)}{t_{i+1} - t_i} \qquad \text{Eq. 3.5}$$

The signal smoothing function is applied again as differentiation amplifies the noise. The last steps of our procedure analysis consist of calculations. The mean residence time is calculated as

$$\overline{t} = \int E(t)t \, \mathrm{d}t = \sum_i E(t_i)t_i \, \Delta t \qquad \text{Eq. 3.6}$$

With the mean residence time we can also calculate the residence time density function in the dimensionless domain, E_ϑ.

3.2.4 Validation experiments

RTD experiments were carried out in a straight capillary with known length. The objectives of this study were:

- to test the apparatus when performing step input experiments;
- to check the repeatability of experiments;
- to investigate the effect of concentration of tracer solution on RTDs.

The RTD was measured in a 3.6 m PFA capillary (1/16'' OD, 1 mm ID), on the setup shown in Figure 3.6. A syringe pump (Mitos Duo XS-Pump, Dolomite) was adopted

to feed the carrier fluid (deionized water) as well as the tracer (aqueous solutions of $CuSO_4$). The pump was equipped with two syringes that could be operated separately. The injection of the tracer was performed in a PEEK Y-junction: the flow of carrier fluid (deionized water) was stopped and almost simultaneously the tracer solution was pumped downstream. This allows us to assume that a perfect step is achieved at the junction, which corresponds to the inlet boundary of the channel. The absorbance detector was placed exactly at a length of 3.6 m from the Y-junction. The operating flow rate was 1 ml/min for both the tracer solution and carrier fluid. Three measurements were performed for each set of parameters to check the repeatability of the results.

The RTD of the straight channel when using a 0.25 M aqueous solution of $CuSO_4$ is shown in Figure 3.7. The curves appear acceptably repeatable, despite the fact that the injection time (t_0) was taken manually with the aid of a stop-watch. The calculated mean residence time $\bar{t}$ is 108 s, which is slightly larger than the time-space τ =106 s. This may be due to the manual recording of the injection time or to interaction between the tracer solution and the walls. The latter is suggested by the shape of the distribution presenting a long tail.

A series of experiments was carried out varying the concentration of tracer solution. The motivation of this study was to check whether varying the concentration of tracer the measured RTD would unexpectedly change. Solutions with concentration as low as 0.0625 M up to 1.0 M were used to measure the RTD in the straight capillary. The experimental RTDs were compared with the analytical solution of the axial dispersion model, which holds in our case ($Bo = 10^4, L/d_t = 3500$). It was adopted the

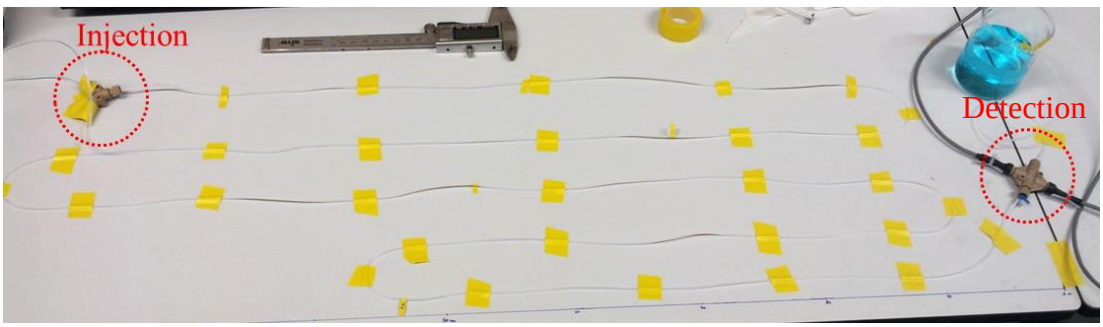

Figure 3.6 - Experimental setup for the RTD measurements in straight capillary.

analytical solution for large deviations from plug-flow ($N_L > 0.01$) and open-open boundary conditions as suggested by Levenspiel (1999):

$$E_{ADM} = \frac{1}{\sqrt{4\pi D_{ax} t}} exp\left[-\frac{(L-ut)^2}{4D_{ax}t}\right] \quad \text{Eq. 3.7}$$

where L is the length of the channel, u the cross-section average velocity and D_{ax} the axial dispersion coefficient, which can be calculated from the Taylor expression for dispersion:

$$D_{ax} = \frac{u^2 d_t^2}{192\, D_m} \quad \text{Eq. 3.8}$$

In Eq. 3.8 the only *unknown* parameter is the molecular diffusion. For this study we adopted the self-diffusion of liquid water ($D_m = 2.2 * 10^{-9} \mathrm{m}^2/s$) as it represents the limiting case at infinite dilution.

Contrary to what expected, different tracer solutions produce different RTDs, indicating that the concentration of tracer significantly affects the measurements (Figure 3.8). As the concentration of copper sulphate increases, the RTDs become

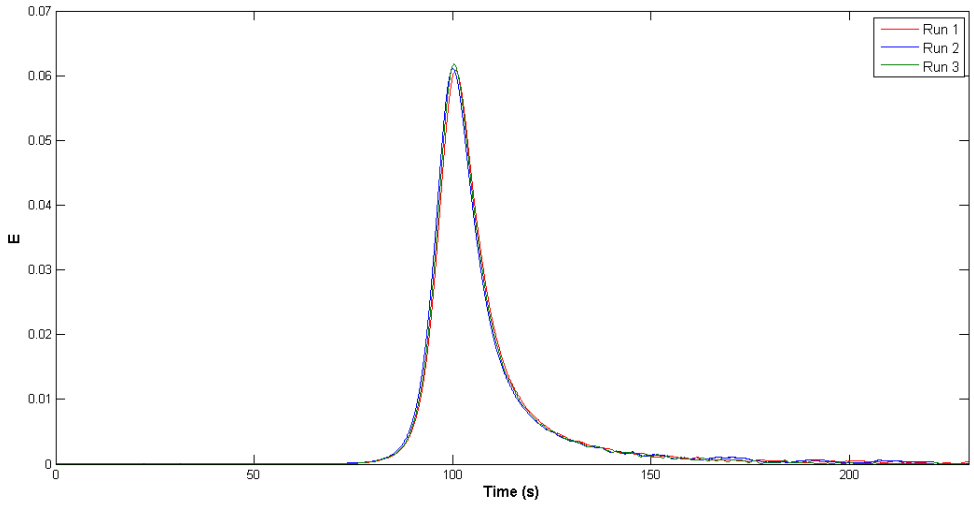

Figure 3.7 - Experimental RTDs of straight channels using an aqueous solution of $CuSO_4$ 0.25 M as tracer.

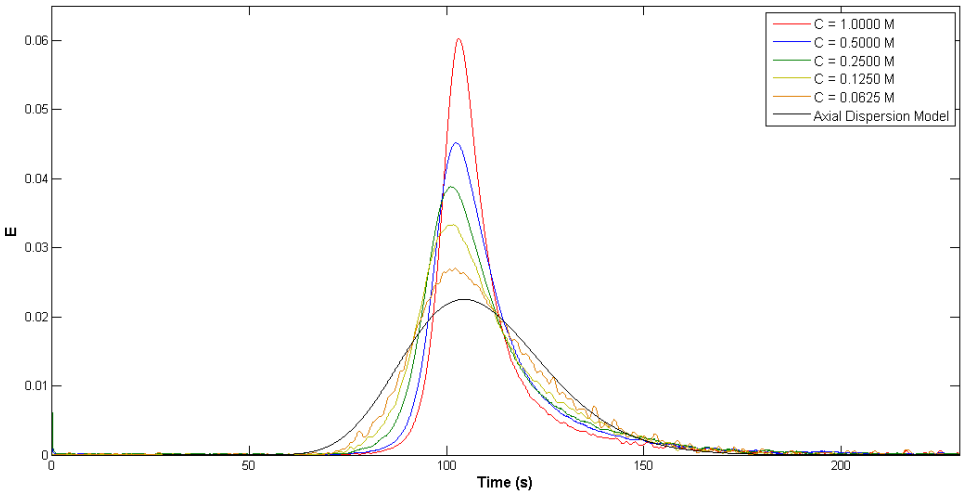

Figure 3.8 – Experimental RTDs varying the concentration of $CuSO_4$ in the tracer solution and analytical RTD.

narrower and narrower. When approaching pure water, the RTD gets closer and closer to the analytical solution predicted by the axial dispersion model. However, at the same time, the signal-to-noise ratio decreases, resulting in irregular curves. At a first glance, one could explain this behaviour referring to the different diffusivities of the tracer solutions. In fact, the mutual diffusion coefficient of $CuSO_4$ in water decreases with the concentration: diffusivities go from around $4.0 * 10^{-10} m^2/s$ at 1.0 M to $7.0 * 10^{-10} m^2/s$ at 0.0625 M (Lobo, 1993). One could conclude that as the solution gets concentrated the diffusion coefficient decreases resulting in narrower distributions. However, this is in contrast with our discussion in section 2.2.4. In laminar regime, faster molecular diffusion helps to reduce the axial dispersion. Indeed, diffusion and dispersion coefficients in Eq. 3.8 are inversely proportional: as D_m decreases (slower diffusion) the axial dispersion coefficient increases. It is clear that there must be an additional effect causing the behaviour observed. We could not find a satisfactory explanation to this result, but suspect that the main cause lies in the nature of the tracer and its interaction with TEFLON tubing walls. This anomalous behaviour was never reported before in the literature. Our observations suggest that care must be taken when performing RTD experiments in TEFLON tubing with aqueous solutions of copper sulphate as tracer.

However, as mentioned before, using a different tracer would imply a full modification of the sensors, which, in any case would work in a specific range of

wavelength. Standard dyes, adopted as tracers for RTD characterization in aqueous systems, have absorbance peaks in the visible. Working in the visible, however would cause problems related to the penetration of external light, whose changes in intensity could significantly affect the measurements. The existing optical cells are prone to external light permeability and would need to be thoroughly covered.

3.3 RTD system with commercial spectrometers

A different RTD experimental system, based on on-line UV-VIS spectroscopy, was designed. This system provides more flexibility in terms of the tracer to be adopted. A study was conducted to choose a suitable flow cell. A calibration was then performed to establish the range of tracer concentration to use for experiments in TEFLON capillaries. Finally, the system and the post-processing analysis were validated using theoretical solutions predicted by the axial dispersion model.

3.3.1 Description of the system

A description of the apparatus is provided in this section and a schematic representation of the system is reported in Figure 3.9.

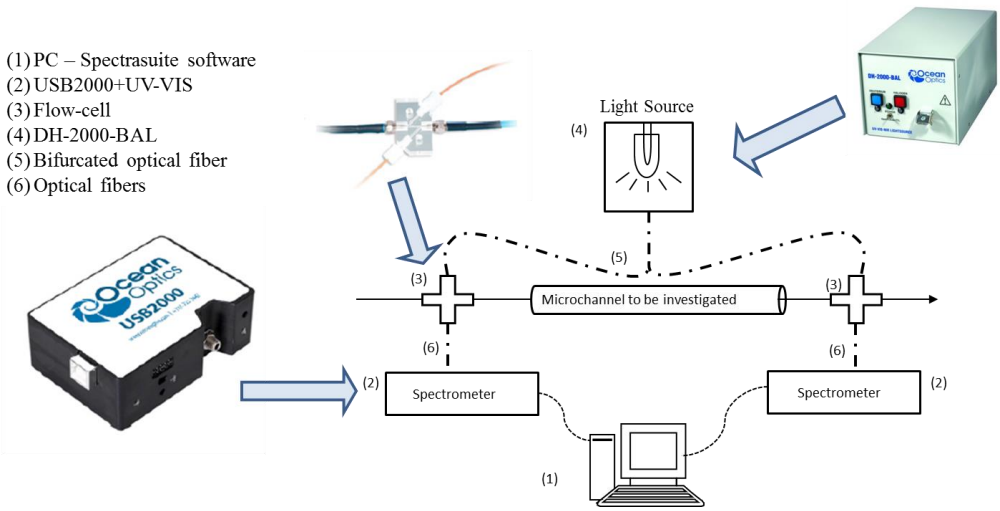

Figure 3.9 – Schematic representation of new RTD systems.

We here refer to the setup characterized by two detection points, needed when ideal injections cannot be realized. The development of this system was aimed at this general case. However, the experimental validation and the experimental work (Chapter 4) was performed using a single detection point at the outlet of the microfluidic system investigated, as perfect step inputs were possible in both cases.

The system consists of two commercial spectrometers (USB2000+UV-VIS, Ocean Optics), with operating wavelength range between 220 and 880 nm. Both the spectrometers were calibrated from the manufacturer to have identical response and therefore be suitable to perform synchronous measurements at two detection points. One end of a bifurcated optical fiber (Ocean Optics) is connected to the source light (Ocean Optics DH-2000-BAL) driving light to the flow cells. Two different flow cells were tested on this system: commercial z-shaped stainless steel (Z-Flow cell-SS, FIA Lab) and custom designed non-intrusive flow cells (in-house designed and manufactured by Cambridge Reactor Design). At the other end of the optical window, a 15 cm optical fiber connects the flow cell to the spectrometer. For all optical connections, we employ 600 µm fiber optics (Ocean Optics). The spectrometers allow performing absorbance measurements with the possibility of selecting the desired wavelength region according to the absorbance spectrum of the tracer.

In conjunction with the changes to the detection system a new techniques for the introduction of tracer was adopted. A six-port sampling valve (Rheodyne V-451) was used with a modified configuration to perform step input experiments (Nagy, 2011). The valve can also be used to realize pulse input experiments, if equipped with a suitable sample loop. A magnetic sensor was mounted on the valve handle and connected to the spectrometer. A signal is sent to the spectrometer, when the valve is switched, starting the acquisition and therefore the experiment. A substantial reduction of the switching time (i.e. time needed to switch from carrier fluid to tracer) is achieved with this approach, as compared to the Y-junction configuration, reducing the experimental error.

3.3.2 Selection of suitable flow cell

Experiments were carried out using the z-shaped flow cells purchased from Ocean Optics. As shown in Figure 3.10a the flow cell is comprised of two ports to which connect the tubing and two ports to secure the fiber optics. The fluid inside the cell follows a Z-shaped path and the distance between the terminations of the fiber optics is 10 mm. Silica glass windows separate the fiber optics from the fluid inside the cell. The light coming from the fiber optic attached to the source light travels through the 10 mm optical path and reaches the fiber optic connected to the spectrometer. We report a picture of the flow cell made of Plexiglas to show the internal path; however a stainless steel version was used for our experiments, to prevent external light from affecting the measurements (Figure 3.10b).

Experiments were performed in a PTFE capillary using a single flow cell placed at 350 cm distance from the injection valve. It was assumed that when switching the valve a perfect step is achieved. The nominal internal diameter of the PTFE tubing was 1 mm and the flow rate was kept constant at 2 ml/min. A 5 mg/L aqueous solution of Basic Blue was chosen allowing to work in the linear region of the Lambert-Beer law and, at the same time, a maximum value of absorbance around 1. Experiments were carried out in series with multiple injections. In this way we performed a series of experiments having both positive steps (switching from pure water to tracer solution) and negative steps (tracer to pure water). From the positive steps we obtain the *F* curve (cumulative distribution function) while with the negative steps we have the *W* curve

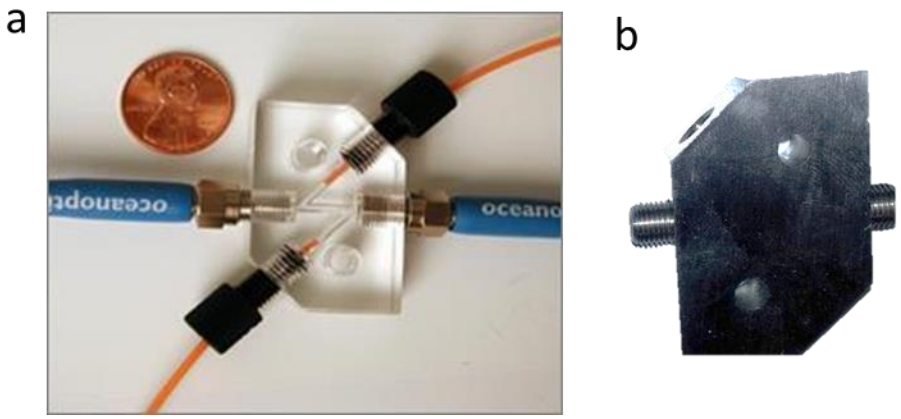

Figure 3.10 - Images of z-shaped flow cells: (a) Plexiglass from FiaLab website (b) Stainless steel.

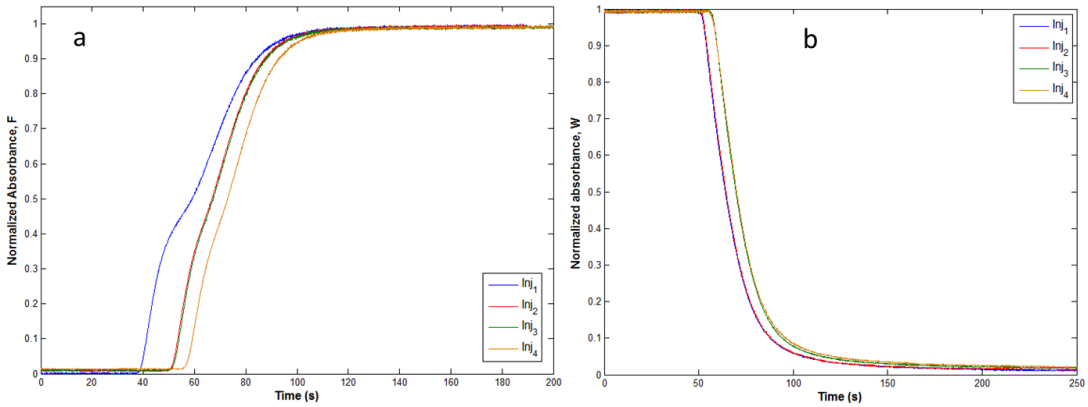

Figure 3.11 - Experiments with z-shaped flow cells: (a) F curves obtained with consecutive positive steps ; (b) W curves obtained with consecutive positive steps, different colors refer to consecutive injections as in the legend.

(wash-out distribution function). The comparison between these two curves can be used as a validation technique since the following relationship must hold (Nauman, 2008):

$$F = 1 - W \qquad \text{Eq. 3.9}$$

The comparison between four different positive step experiments is reported in Figure 3.11a. The graph reporting the normalized absorbance shows that poor reproducibility is obtained. The F curves present an unexpected curvature change in the central region, which also varies after each injection. The change of curvature appears less evident in

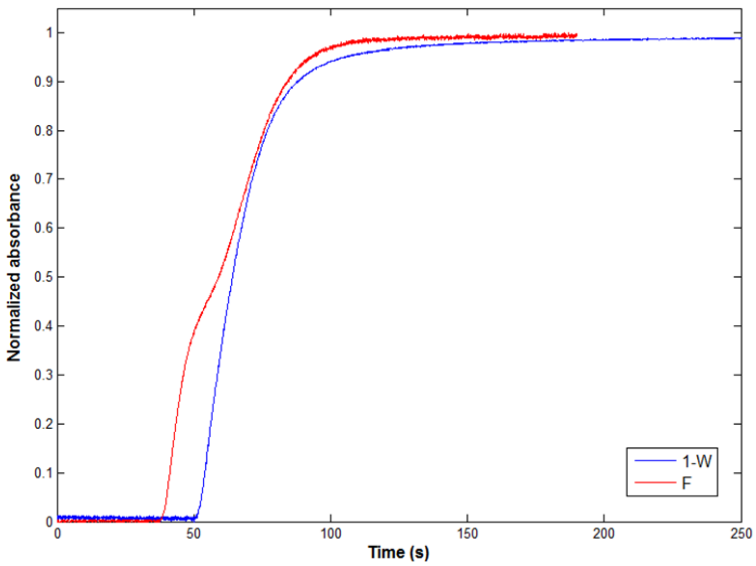

Figure 3.12 - Comparison between the results of positive and negative step experiments in Z-shaped flow cell.

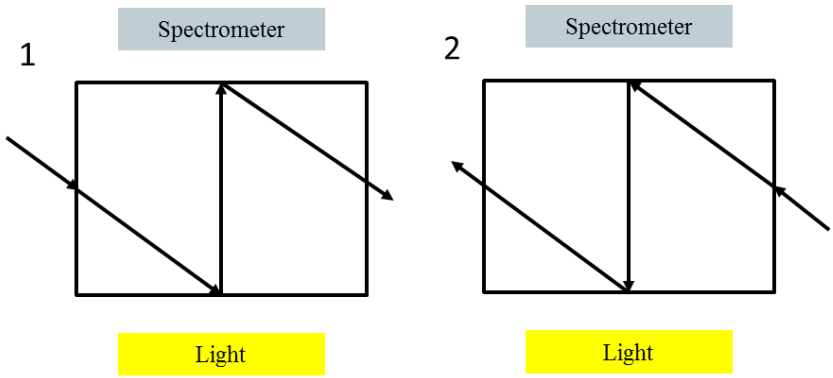

Figure 3.13 - Two possible setup configurations of the z-shaped flow cells. The arrows indicate the direction of the flow.

the curve produced with the fourth injection than the first one. It should be noted that this change of curvature would generate a second peak in the E curve, which may indicate the presence of a dead volume or interaction of the tracer with internal surfaces in the flow cell (Levenspiel and Turner, 1970). Differently, the curves obtained with negative injection do not present any unexpected behaviour (Figure 3.11b).

The difference between positive and negative steps appear clear in Figure 3.12, where a comparison between one of the F and $1 - W$ curves is plotted. It is clear that the relationship reported in Eq. 3.9 does not hold for this system. Additionally, two different configurations are possible when setting up the z-shaped flow cells depending on the relative positions of the inlet/outlet channel and those of the source light/spectrometer). When running experiments using configurations 1 or 2 (left-hand and right-hand side of Figure 3.13 respectively), different F curves were obtained. This may be due to dilution effects taking place in the small chamber inside the cell as well as interaction of the tracer with silica glass present in the cell.

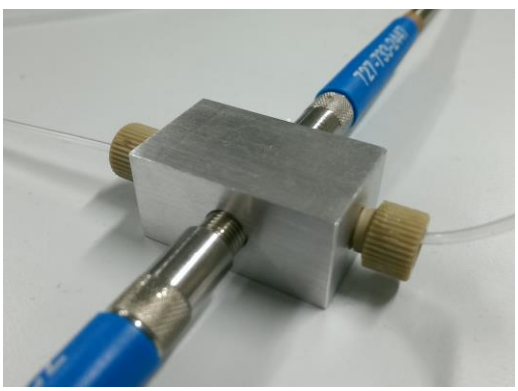

Figure 3.14 – Custom designed non-intrusive flow cell.

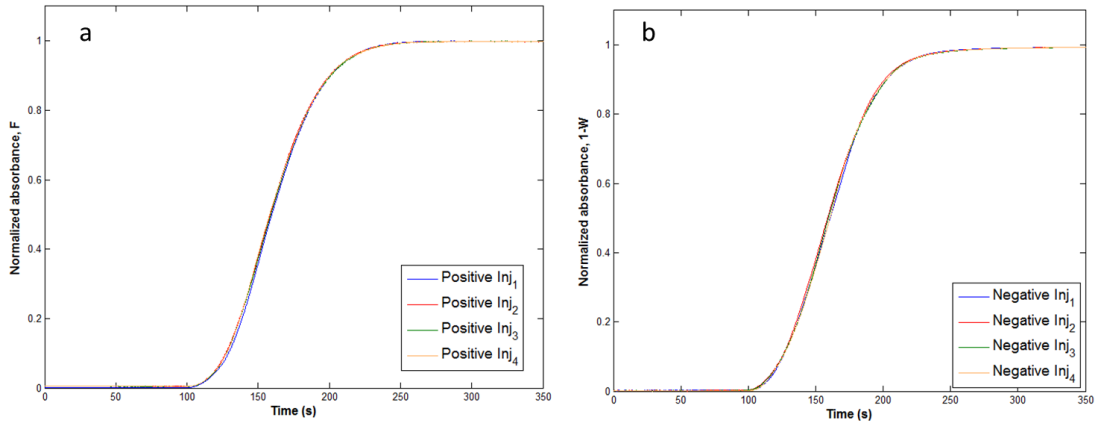

Figure 3.15 Experiments with non-intrusive cross-shaped flow cells: (a) F curves obtained with consecutive positive steps ; (b) W curves obtained with consecutive positive steps.

The results obtained with commercial z-shaped flow cells demonstrated that these devices are not suitable for reliable characterization of RTDs.

Flow cells similar to those adopted for the in-house made detectors were designed. The non-intrusive cell was a rectangular aluminum block with two crossing holes (Figure 3.14). At the two ends of the long hole standard ports allow securing the tubing (Teflon, OD 1/16 in.) passing through the cell. The shorter hole accommodates the light path with suitable connections to fit the optical fiber. Differently from the commercial Z-shaped flow cells, there is no need for silica glass windows as the terminations of the fiber optics are separated from the flowing fluid by the tubing walls.

Similar test experiments were conducted with multiple injections on the newly designed flow cells to check both the reproducibility and the difference between positive and negative step experiments (Figure 3.15). The normalized plot of F curves shows a smooth sigmoid for all the consecutive injections, which also demonstrates a high degree of repeatability. Similarly the washout curves, shown as $1 - W$, do not present any unexpected behaviour and appear repeatable. Figure 3.16 compares one of the F curves with one of the $1 - W$ curves, resulting in a close match, hence demonstrating the validity of Eq. 3.9 when employing custom designed non-intrusive flow cells.

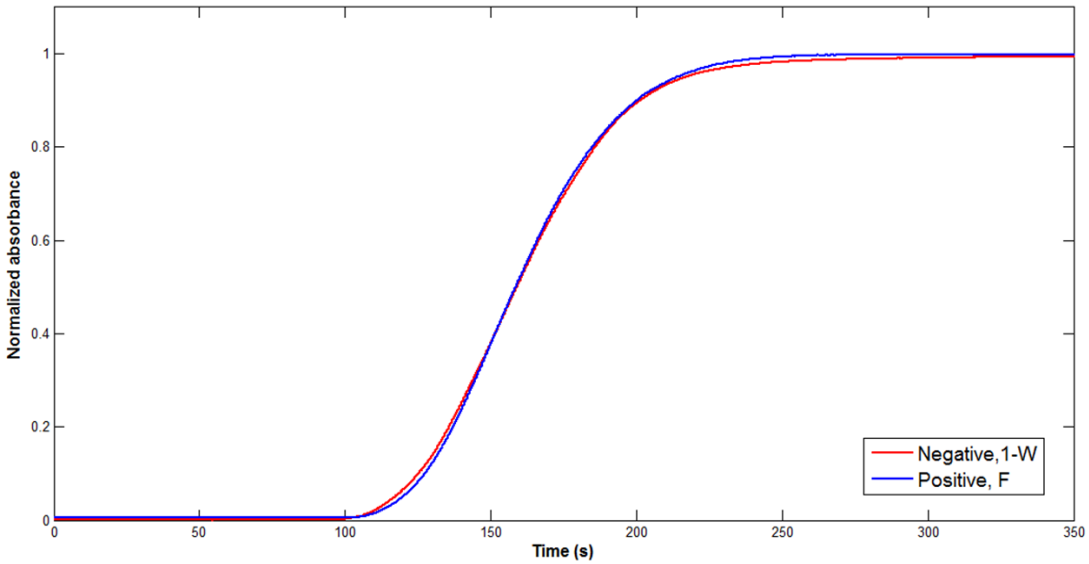

Figure 3.16 - Comparison between the results of positive and negative step experiments in non-intrusive cross-shaped flow cells.

This study was conducted to assess the performance of both commercial z-shaped and non-intrusive custom-designed flow cells. The former proved to be unsuitable for RTD measurements based on on-line UV-VIS detection supposedly as a result of dilution effects in the 10 mm chamber. Additionally, the z-shaped flow cells are intrusive, with wetting surfaces made of stainless steel and silica glass: performing RTD measurements in multiphase flow would not be possible due to the change in the wettability properties. The cross-shaped cell was designed specifically to avoid wetting parts and it has demonstrated to produce repeatable and robust measurements, regardless of the step input typology.

3.3.3 Absorbance calibration

Similarly to what reported in section 3.2.2 for the in-house made detection system, calibration experiments were carried out on the UV-VIS detection system and presented in this section. As previously pointed out, it is essential to carry out preliminary experiments to check the region of validity of the Lambert-Beer law sampling different tracer concentrations.

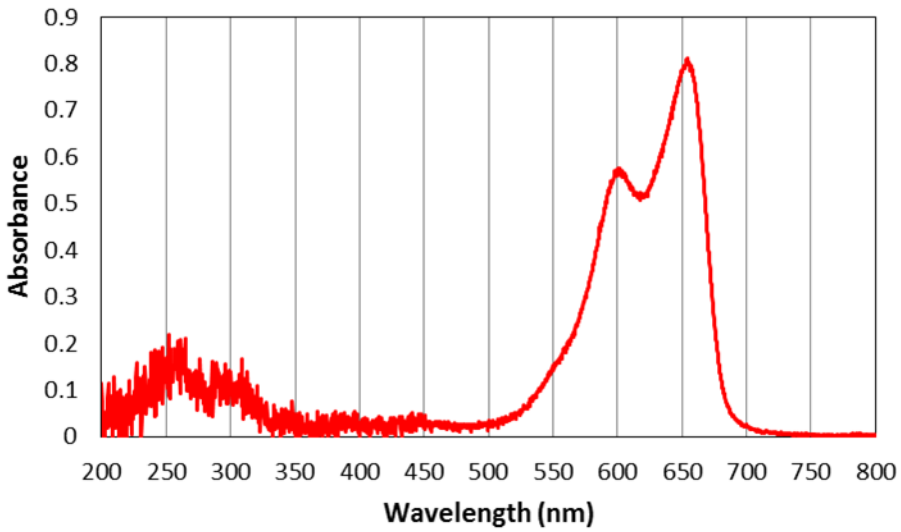

Figure 3.17 – Absorbance spectrum of Basic Blue 3 detected with in-line UV-VIS spectrometers.

As described in the previous section, the optical detection takes place in a non-intrusive flow cell where a fraction of the light is reflected by the capillary surfaces. However, depending on the internal diameter of the tubing adopted (i.e. thickness of tubing walls), a significant fraction of light is reflected inducing to use different concentrations of tracer solution. This needs to be sufficient to have acceptable values of absorbance in terms of signal-to-noise ratio, but low enough to be in the Lambert-Beer range.

Aqueous solution of Basic Blue 3 (Sigma-Aldrich, CAS 33203-82-6) were employed as a tracer. This is an organic dye highly soluble in water and it has been used in the past for RTD characterization (Bošković and Loebbecke, 2008). It was found that Basic Blue interacts poorly with the surface of Teflon tubing (both PFA and PTFE) as compared to other tracers. For this reason, it was chosen in this work. Basic Blue 3 presents the highest absorbance peak around 650 nm as showed in the absorbance spectrum in Figure 3.17. To obtain smoother absorbance readings, the absorbance was averaged over a narrow range of wavelengths around the peak (645-660 nm).

A test setup similar to that adopted for the in-house made detectors (Figure 3.3) was employed to perform absorbance readings with different tracer concentrations. Both the flow cells were connected to the spectrometers and readings were taken using different Teflon tubing. Preliminary tests were performed on both PTFE and PFA

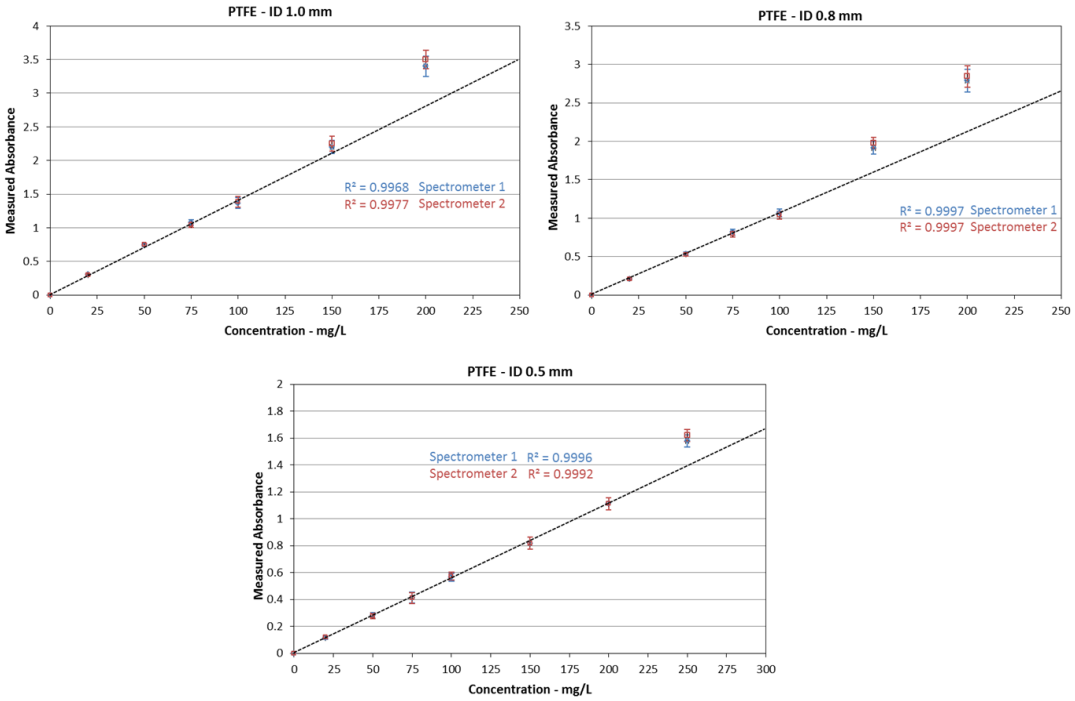

Figure 3.18 – Absorbance calibration in different PTFE tubing. The absorbance was sampled in both the spectrometers, here the data points refer to spectrometer 1 (blue) and 2 (red).

capillaries and the former appeared to produce less noisy absorbance measurements. PTFE was adopted for these calibration experiments with OD 1/16 and ID 0.5, 0.8 and 1.0 mm. The absorbance was measured in stagnant conditions and three readings were taken for any set of parameters.

Each reading produced slightly different absorbance values depending on the concentration as a result of increased noise for high values of absorbance (commonly above 1). On the graphs the standard deviation is shown as error bars (Figure 3.18). It can be observed that for the 1.0 mm tubing above 100 mg/L deviations from linear are encountered, while this critical value shifts toward higher concentrations with smaller internal diameter tubing. Both spectrometers produce very close absorbance readings

Table 3.1 – Chosen optimal values of concentration of Basic Blue 3. The values are chosen such that the Lambert-Beer holds and the signal-to-noise ratio is maximized.

Internal diameter (mm)	**1.0**	**0.8**	**0.5**
Optimal concentration of Basic Blue (mg/L)	75	100	200

at each concentration and tubing considered. This is particularly important for measurements with two detection points. Chosen values of optimal tracer concentration for each internal diameter considered are reported in Table 3.1. The values were chosen such that the Lambert-Beer holds and, at the same time, the signal-to-noise ratio is maximized.

3.3.4 RTD data post-processing

The adoption of commercial spectrometers interfaced with a dedicated software (Spectrasuite, Ocean Optics) simplified the post-processing of data. It is possible to set up directly on the graphical interface an absorbance measurement. Note that this was not possible with the system based on in-house made detectors: the output of these was a voltage signal (proportional to the intensity of light) and the absorbance was calculated in post-processing. As a result, a new procedure for the analysis of data was developed. The absorbance spectrum is calculated by the software according to the following formula:

$$A(t,\lambda) = -\log_{10}\frac{I(t,\lambda_w) - I_D(\lambda_w)}{I_R(\lambda_w) - I_D(\lambda_w)} \qquad \text{Eq. 3.10}$$

where $I(t,\lambda_w)$ is the actual light intensity spectrum recorded by the spectrometer (expressed in terms of photon counts), $I_R(\lambda_w)$ and $I_D(\lambda_w)$ the light intensity spectra when water flows through the optical path with the source light switched on and off respectively. The dark spectrum is required to start an absorbance reading; however, it would not be strictly necessary for our system, for the flow cells are made in aluminum preventing external light from penetrating into the optical path. Indeed the dark spectrum shows zero photon count for any wavelength. The reference spectrum corresponds to I_0, defined in Eq. 2.28. The absorbance spectrum shows the value of absorbance for any wavelength between 200 and 880 nm. We are only interested in the values of absorbance around the wavelength region where the extinction coefficient of the adopted tracer is maximum. A so called "strip-chart" can be created on Spectrasuite, with the possibility of recording a single or an averaged (for a range of wavelengths) value of absorbance over time. The second option is suggested as smoother signal can be generated and it was adopted for our experiments. The

absorbance-time data is saved to a *csv* file for RTD post-processing. Minor modifications to the MATLAB scripts previously developed were needed to analyze directly the absorbance-time data. The substantial difference was the normalization of the absorbance to calculate the F curve for step input experiments. This calculation was implemented according to:

$$F(t_i) = \frac{A(t_i)}{\bar{A}} \qquad \text{Eq. 3.11}$$

where $A(t_i)$ is the value of absorbance at any time t_i and $\bar{A}$ is the maximum value of absorbance, corresponding to full tracer concentration flowing into the optical cell. The smoothing algorithm, the differentiation (to obtain the *E* curve) and the calculation of mean residence time were unchanged (section 3.2.3).

An additional MATLAB script was developed to perform fitting of experimental RTDs with theoretical solutions of ADM. Two analytical solutions were employed and implemented in the post-processing script: the solution for large deviations from plug flow boundary conditions (reported in Eq. 3.7) and that for small deviation from plug flow (Levenspiel, 1999) reported here:

$$E_{t,ADM} = \sqrt{\frac{u^3}{4\pi D_{ax} L}} \exp\left[-\frac{(L-ut)^2}{4D_{ax}L/u}\right] \qquad \text{Eq. 3.12}$$

where u is the mean flow velocity, L is the total length of the tube from the injection to the detection point, t is the time elapsed from the injection of the tracer and D_{ax} is the axial dispersion coefficient. The only unknown parameter is D_{ax}. The experimental $E_{t,exp}$ curves are fitted with Eq. 3.7 or Eq. 3.12 so that the axial dispersion coefficient ($D_{ax,fitt}$) can be calculated. The fitting is based on the least squares method, that is:

$$\min_{D_{ax}} \sum_i \left[E_{t,ADM}(D_{ax,} t_i) - E_{t,exp}\right]^2 \qquad \text{Eq. 3.13}$$

This was implemented using the *lsqcurvefit* function available in MATLAB. The residual error of the converged solution can be used to judge the quality of the fitting. The error is so calculated:

$$\varepsilon = \sum_i \left[E_{t,ADM}\left(D_{ax,fit}, t_i\right) - E_{t,exp}\right]^2 \qquad \text{Eq. 3.14}$$

This parameter was used to propose a criterion for the applicability of ADM in conditions different from straight channels, for which flow maps, such as the one reported in Figure 2.4, are not available.

Note that the analytical solution (either Eq. 3.7 or Eq. 3.12) to use depends on the vessel dispersion number ($N_L = D_{ax}/uL$), which is not known before performing the fitting. Specifically, the solution for small deviation must be used when $N_L < 0.01$, and that for large deviation when $N_L > 0.01$. As a consequence, the fitting was carried out with both solutions and the vessel dispersion number was calculated after the fitting. The calculated axial dispersion coefficient not satisfying the condition of applicability of the solution was then discarded.

3.3.5 Validation experiments

Validation experiments were performed in a straight capillary with known length. The objectives of this study were:

- to test the apparatus when performing step input experiments;
- to investigate the effect of concentration of tracer solution on RTDs;
- to validate experimental RTDs with theoretical ones predicted by the ADM.
- to measure the diffusion coefficient of Basic Blue 3 and to compare the measured value to those found in the literature.

Step input experiments were performed in a 5 m straight capillary (PTFE, ID 1.0 mm) with a setup similar to that reported in section 3.2.4 . The inlet of the capillary was connected directly to the exit port of the sampling valve, where the step change takes place. Preliminary experiments, conducted with the optical cell placed as close as possible to the exit port of the valve, revealed an almost instantaneous change of absorbance to the value corresponding to full concentration of tracer. Under these circumstances, a perfect step is achieved and the *F* curve can be directly obtained with a single detection point, placed at the outlet of the capillary.

In a first series of experiments the concentration of tracer was varied between 25 and 100 mg/L, lying in the region of validity of the Lambert-Beer law. The flow rate was kept constant at 0.75 ml/min. The F curves were perfectly matched with varying concentrations (Figure 3.19a) while the E curve overlap for concentrations above 25 mg/L. This is due to poor sensitivity when employing tracer concentration considerably lower than the optimal value (see 3.3.3). This aspect is more evident in the E curves where the differentiation magnifies the error (Figure 3.19b). Differently from the results obtained with copper sulphate as tracer, the RTDs measured with Basic Blue 3 are not dependent on its concentration in the tracer solution. This represents a crucial step toward the full validation of the experimental procedure.

Further validation experiments focused on the applicability of the axial dispersion model were conducted. As discussed in section 2.3, the ADM can be used to model RTDs of straight tubes operated in laminar regime provided that the time scale of molecular diffusion is smaller than the mean residence time of the vessel. The flow regime map reported in Figure 2.4 suggests the regions of applicability of the ADM. For straight tubes of circular cross section the Taylor-Aris equation expresses the relationship between axial dispersion and molecular diffusion coefficient (Levenspiel, 1999):

$$D_{ax} = D_m + \frac{u^2 d_t^2}{192\, D_m} \qquad \text{Eq. 3.15}$$

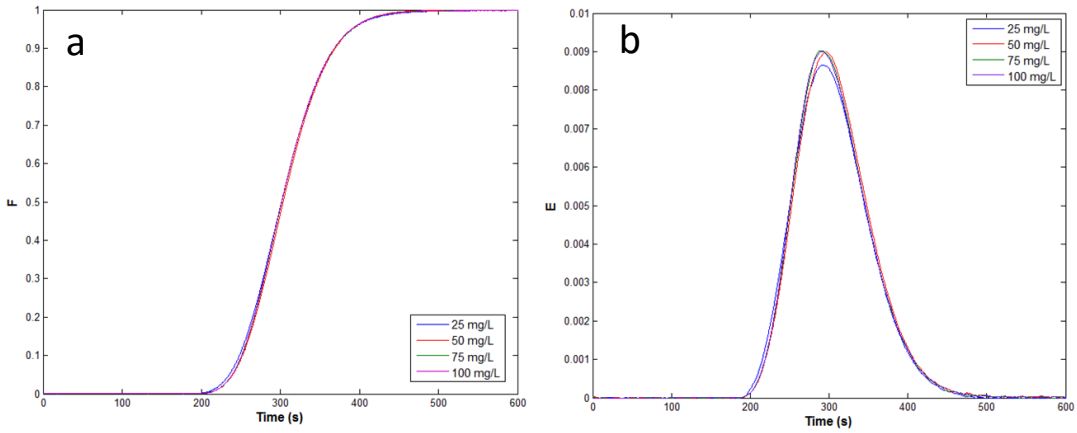

Figure 3.19 – Effect of tracer concentration on F curves (a) and E curves (b) in straight capillary using on-line UV-VIS spectroscopy.

where u is the mean flow velocity, d_t the internal diameter of the capillary, D_m the molecular diffusion coefficient of the tracer into the carrier fluid and D_{ax} the axial dispersion coefficient. The dispersion behaviour depends on the balance between the diffusion and convection rate, expressed by the Bodenstein number ($Bo = ud_t/D_m$). The first term on the right hand side of Eq. 3.15 is dominant when $Bo < 10$, that is when diffusion prevails over convection. When Bo is greater than 100, this term can be neglected. Note that for liquid systems, molecular diffusion coefficients are in the order of $10^{-9}\mathrm{m}^2/\mathrm{s}$. As a result diffusion is hardly dominant (e.g. only when convection approaches zero) and Bodenstein numbers are in the order of 10^4. Eq. 3.15 can then be simplified and rearranged in this way:

$$D_{m,calc} = \frac{u^2 d_t^2}{192\, D_{ax,fitt}} \qquad \text{Eq. 3.16}$$

This equation can be used to calculate molecular diffusion coefficients from RTD experiments in straight tubes. In order to use Eq. 3.16 one must perform experiments under full applicability of the dispersion model, which primarily depends on Bo. Nevertheless, the Bodenstein number cannot be precisely calculated, but just estimated, if the molecular diffusion coefficient is not known. Hence, the conditions of applicability of the model are not known in advance. We employed a procedure to gather information on the applicability of the model as well as to calculate the unknown molecular diffusion coefficient based on the following steps:

- RTDs were measured in a straight capillary with aspect ratio $L/d_t = 5000$ under different Reynolds numbers ($Re = \rho u d_t/\mu$) by varying the flow rate of carrier fluid and tracer solution ($0.025 - 1.0\ \mathrm{ml/min}$). Note that $Bo = Re * Sc$, thus varying Re one moves on a vertical line of the flow regime map because the aspect ratio of the straight tube is constant (Figure 2.4). As a result, although not known exactly (Sc cannot be calculated as D_m is not known), the operating point is located on a vertical line of the flow map and can be inside or outside the region of full applicability of the ADM.

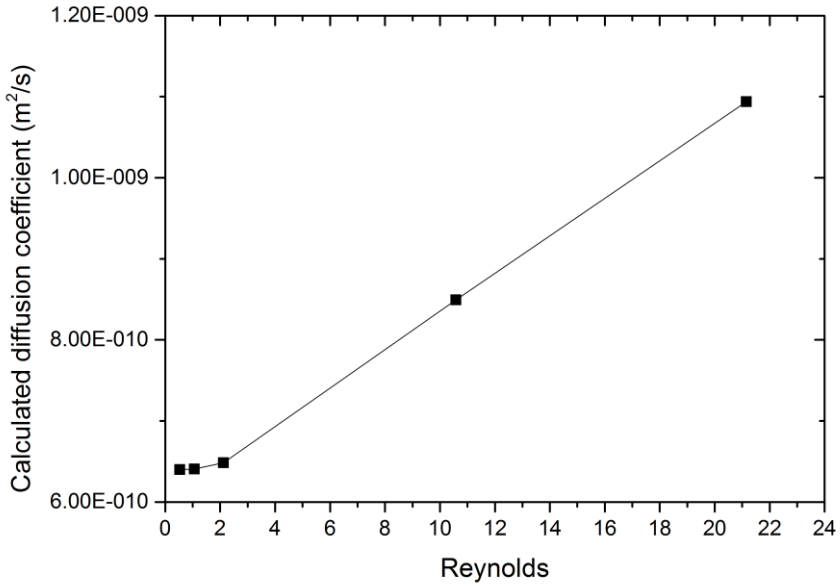

Figure 3.20 – Calculated molecular diffusion coefficients of Basic Blue 3 in water as a function of Re.

- The experimental curves were fitted with analytical solutions of ADM so as to determine the axial dispersion coefficients using the method described in 3.3.4.
- The molecular diffusion coefficients were calculated using Eq. 3.16 and plotted aginst Re (Figure 3.20). We observed that for $Re > 2$, the calculated axial diffusion coefficient depended on Re. However, the calculated molecular diffusion coefficient must not change varying Re, as it is an intrinsic transport property of the system water-tracer. We concluded that the model was fully applicable only for $Re < 2$. As a result the calculated value of D_m is $6.40 * 10^{-10}$ m^2/s. This value is in agreement with measured molecular diffusivities of Basic Blue 3 in water reported in the literature (McKay et al., 1981), validating our experimental procedure in conditions of full applicability of the ADM
- In order to confirm this result, the correct Bodenstein numbers were calculated using the measured molecular diffusion coefficient and the resulting operating points plotted on the flow regime map (Figure 3.21). It can be clearly observed

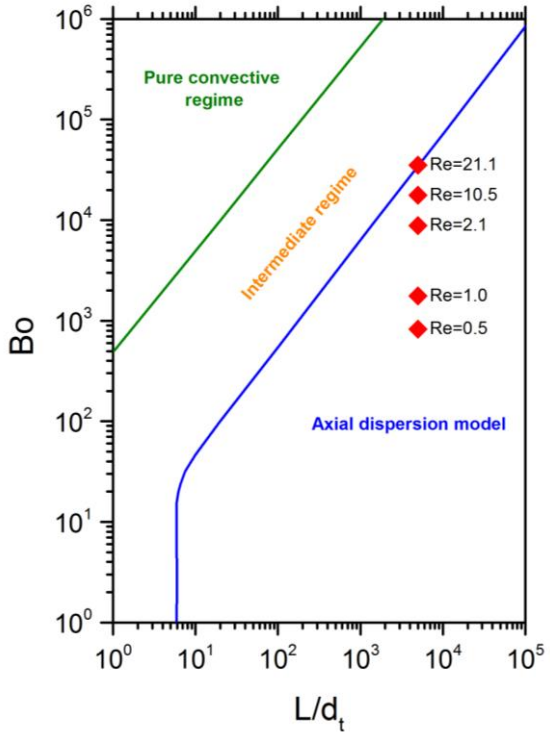

Figure 3.21 – Operating points (in red) on the flow regime map for validation experiments in straight capillary. The map was adapted from Anthakrishnan et al. (1965).

that the experiment carried out when $Re = 21.1$ lies on the line separating the intermediate region from the zone of full applicability of the model. The experiment conducted at 0.5 ml/min ($Re = 10$), despite being in the ADM region, overestimates D_m with an error of 3 %. The applicability of the model can still be considered valid as a result of the small error produced.

3.3.6 A criterion for the applicability of the ADM

Validation experiments presented in the previous section are also important to define a general criterion to be used for the application of the ADM to flow in pipes with geometries different from straight.

It should be noted that the flow regime map suggesting the region of full applicability of the ADM is only valid for straight pipes. Such flow maps are not available for geometries other than straight (e.g. secondary flow in helically coiled tubes). As a result, the values of Bo for which the model is expected to hold are not known. One needs to identify a method for judging the applicability of the model. It has been

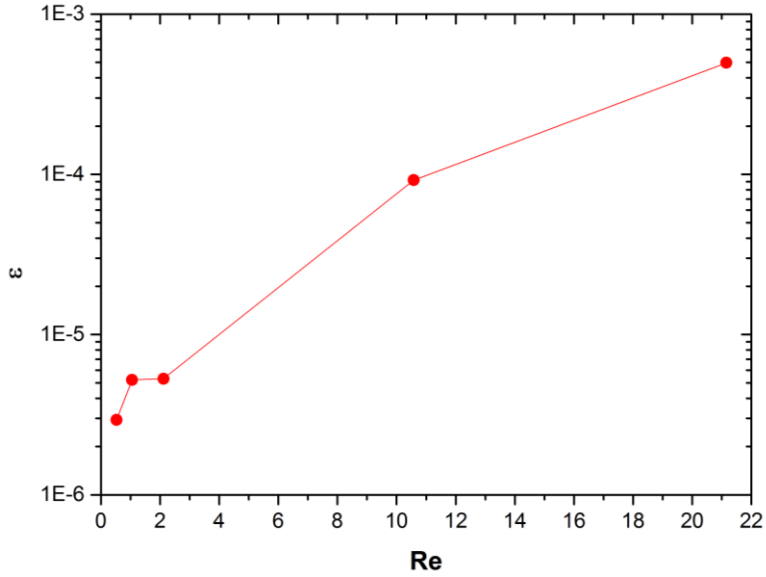

Figure 3.22 – Residual error of the fitting of RTD experiments in straight capillary with solutions of ADM as a function of Re.

suggested in the literature to use the residual error of the data fitting (Eq. 3.14) for this is an indication of the quality of the matching between experimental and theoretical RTDs. Trivedi and Vasudeva (1975) established a threshold value for the residual error of the fitting above which experimental dispersion data of HCTs were discarded.

In this work, a similar but improved approach was adopted. The values of residual errors of the ADM fitting (ε) were reported as a function of the Re (Figure 3.22). The residual error decreases with Re indicating that the quality of the fitting improves. As expected, experiments close to the boundary with the intermediate regime generates greater error and as Bo. However, it can be observed that only the data point corresponding to $Re = 21$ lies on the boudary line between the intermediate zone and ADM zone (Figure 3.21). To this point corresponds a fitting error greater than 10^{-4}. For this reason and also in conjunction with the discussion about the calculated values of calculated diffusion coiefficients, it was identified

$$\varepsilon_{cr} = 10^{-4}$$

as the critical value of residual error to judge valid the applicability of the model for RTDs derived in configurations other than straight.

3.4 Conclusions

Laminar flow characterizes microfluidic devices making hydrodynamic studies crucial for their optimal design. Specifically, when axial dispersion is to be minimized, RTD analysis represents a powerful tool. However, standard techniques for experimental approaches are yet to be established. The aim of the work presented in this chapter was to develop and validate a platform to perform reliably hydrodynamic studies by means of RTD on different microfluidic devices. As result of this work the following conclusions can be drawn:

- An experimental platform based on UV-VIS spectroscopy was developed. This can be used for different microfluidic devices, both capillary- and chip-based systems. The platform employs on-line optical detection directly performed through the walls of standard Teflon tubing with the aid of flow-cells. It also allows conducting synchronous measurements at two detection points when convolution is necessary.
- A first version of the detectors was assembled using inexpensive sensors connected to standard Upchurch crosses. This solutions appeared to suffer from several technical problems. Originally, the couple photodiode-light was designed for working in the infrared region to avoid external light to affect the measurements. Copper sulphate was chosen as tracer for experiments with water as carrier fluid. However, significantly high concentrations of tracer were needed to obtain acceptable signal-to-noise ratio. Under these conditions, RTD measured with step input experiments in capillary tubes were found to be very sensitive to the concentration of tracer solution. Such anomalous behaviour was observed for the first time suggesting that electrolytes, such as copper sulphate, may be unsuitable for RTD studies in TEFLON tubing. It is believed that this behaviour is related to the nature of tracer and its interaction with the surface of the capillaries.
- The second and final version employs commercial spectrometers and custom designed aluminum flow cells. The importance of designing flow cells without wetting parts was proved with a specific study on commercial z-shaped flow cells. These were not found suitable as flow-cell for optical detection of tracer

in RTD experiments. Conversely, the custom designed flow cells appeared to produce consistent RTDs when performing both positive and negative step input experiments. The concentration of tracer does not affect the final RTDs, as with the first setup. The developed platform can be used both for single phase and multiphase RTD characterization in a wide range of microfluidic devices. A practical guide is provided in Appendix A. MATLAB scripts for RTD post-processing were developed and reported in Appendix B.

- Step input experiments in straight capillary were carried out to verify the agreement of experimental RTDs with those predicted by the ADM. The molecular diffusion coefficient of Basic Blue 3 in water was also measured and found to be in agreement with values reported in the literature.
- Ultimately, the conditions of applicability of the ADM were discussed and a general criterion for extending the model to configurations other than straight tubes was proposed.

.

Chapter 4

Axial dispersion in CFIs and HCTs

4.1 Introduction

Among the different ways to narrow down the RTD in laminar flow, characterizing microchannel devices, secondary flow and chaotic advection are the most promising. Even so, not many works in the literature have focused on the beneficial effects of such systems on RTDs (see 2.5). Many geometrical parameters affect the hydrodynamic dispersion in coiled flow inverters (CFIs) due to the combined influence of secondary flow and chaotic advection. The interpretation of their effect on the RTD is crucial for the optimal design of CFIs with reduced axial dispersion. The aim of this work is to perform hydrodynamic studies on different CFIs and helically coiled tubes (HCTs) so as to gain more knowledge on how different design parameters affect the axial dispersion. In particular, the coil-to-tube diameter ratio (the ratio of the diameter of the cylindrical support and that of the fluid tube) defines the magnitude of the centrifugal force acting on the fluid, which primarily creates radial mixing. It is therefore a critical design parameter. Despite this, the effect of coil-to-tube diameter ratio on RTDs has not been extensively studied in HCTs and never in CFIs. For this reason, in this chapter RTD studies conducted on in-house manufactured HCTs and CFIs with different coil-to-tube diameter ratios are reported. The dispersion was characterized using the axial dispersion model. The separate effect of Reynolds number and coil-to-tube diameter ratio was evaluated in terms of axial dispersion number.

4.2 Experimental section

4.2.1 Construction of CFIs and HCTs

In the context of this work CFIs and HCTs were constructed using PVC tubes as supporting frame. For HCTs the support was a straight section of PVC pipe, while for CFIs the PVC pipe was cut in small sections with 45-degree edges and glued together forming a tridimensional frame (Figure 4.1).

PTFE capillaries (Kinesis, OD 1/16 in) with different internal diameters were coiled on the PVC frame. The capillary was firmly secured on the supporting frame using cable ties. The axial pitch was minimized by having successive turns contiguous so that the distance between successive turns equals the external diameter of the capillary. The number of turns was dictated by the dimension of the PVC sections forming the 3D frame. Due to manufacturing constraints it was not possible to have PVC sections greater than 20 mm. Therefore, it was chosen $n_t = 8$ as the number of turns on each arm of the CFI. Note that in order to have sharp flow inversions it is necessary to minimize the free space on each arm of the CFI. The n_t chosen allows having a fully developed secondary flow and was kept constant for all CFIs constructed. A fixed number of bends was selected for study: our focus was on the effect of λ rather than the number of flow inversions, which has been already studied in the literature. Additionally, data in the literature show that the number of bends strongly determines the axial dispersion. In order to study the effect of curvature ratio under identical effect of flow inversions, the number of bends was kept constant for all CFIs constructed.

Figure 4.1 – Example of supporting frame for CFI made with PVC pipes.

Table 4.1 – Geometrical parameters of characterizing the CFIs.

Coil-to-tube diameter ratio	**17.8**	**26.2**	**65.6**
Diameter of support (mm)	17	20	32
Internal diameter of tube (mm)	1.0	0.8	0.5
Length of tube (m)	9.75	11.25	18.85
Axial pitch (mm)		1.6	
Number of bends		19	
Number of turns		8	
Total number of turns		160	

CFIs investigated include 19 bends with a total of 160 turns. This led to very long capillaries (ranging between 9 and 19 m depending on D_s) that was necessary to expand the operative zone for the application of the axial dispersion model.

By changing both D_s and d_t CFIs and HCTs with λ ranging between 17 and 64 were constructed. The CFIs and HCTs investigated are shown in Figure 4.2.

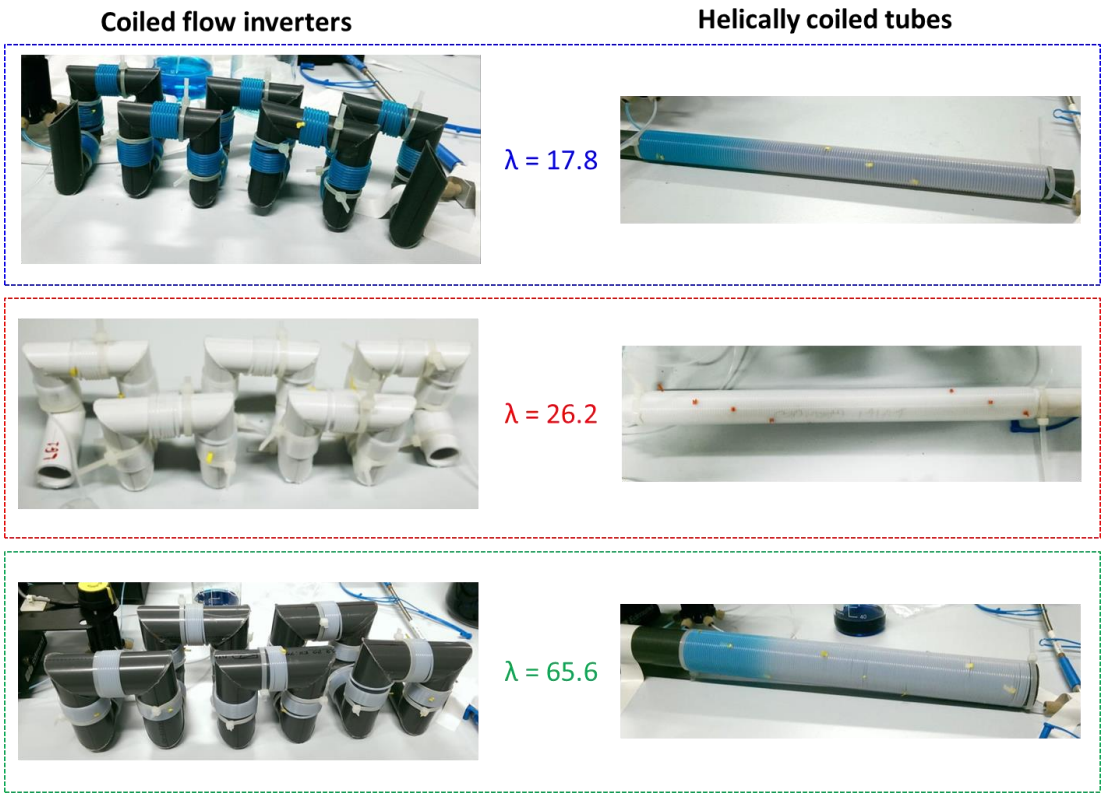

Figure 4.2 – CFIs and HCTs constructed with different coil-to-tube diameter ratios.

4.2.2 Experimental setup and procedure

The hydrodynamics of CFIs and HCTs were studied by means of RTD experiments with the setup shown in Figure 4.3. A dual syringe pump (Harvard Apparatus, PhD 2000) equipped with 25 mL glass syringes (SGE) was used to feed the carrier fluid (deionized water) and the tracer (aqueous solution of Basic Blue 3). The adoption of syringe pumps is important to ensure low pulsations and accurate flow rates. Step input experiments were performed with the aid of a 2 position 6-way injection valve (Rheodyne V-451). The CFI or HCT was directly connected to the valve so as to achieve a sharp step input directly at the inlet boundary. Tracer detection was performed by means of through-the-wall optical measurements. A light source (Ocean Optics DH-2000-BAL) and a spectrometer (Ocean Optics USB-2000) were connected to the flow cell with the aid of 600 μm optical fibers. The flow cell was designed to snugly fit standard 1/16 in Teflon tubing, which can be pulled over to be located precisely at the outlet boundary of the CFI or HCT. The terminations of the optical fiber are in contact with the external surface of the PTFE capillary. In this way, the detection takes place perpendicularly to the direction of flow. The non-intrusive flow cell was manufactured in aluminum to seal the detection point from external light. The transient response of the investigated system to step input of tracer was recorded in terms of absorbance and acquired with the aid of the commercial software Spectrasuite (Ocean Optics). A magnetic sensor mounted on the injection valve triggered the start of the acquisition, thus the experiment. The concentration of tracer used in the inlet mixture depended on the internal diameter of the capillary used. In all cases, the concentration was determined to be within the linear range of the Lambert-Beer law (as reported in 3.3.3).

For each configuration, experiments were carried out at different flow rates ranging between 0.05 and 5.0 ml/min. At least three experiments were performed for any set of parameters to check for repeatability, for a total of 150 experiments.

4.2.3 Analysis and modelling of RTD data

The analysis procedure of absorbance-time data to determine correct RTDs is discussed here together with the modelling approach employed to derive information on the axial dispersion.

The experimental setup and protocol were designed so as to perform step input experiments. Under these circumstances, the F curve can be obtained after normalization of the absorbance-data curve $A(t)$

$$F(t) = \frac{A(t)}{\bar{A}} \qquad \text{Eq. 4.1}$$

where $\bar{A}$ is the maximum value of absorbance, corresponding to full tracer concentration flowing into the optical cell. A smoothing algorithm was applied to the F curve to reduce the noise generated by the acquisition. The E curve was then obtained through numerical differentiation of the F curve

$$E(t) = \frac{\mathrm{d}F(t)}{\mathrm{d}t} \qquad \text{Eq. 4.2}$$

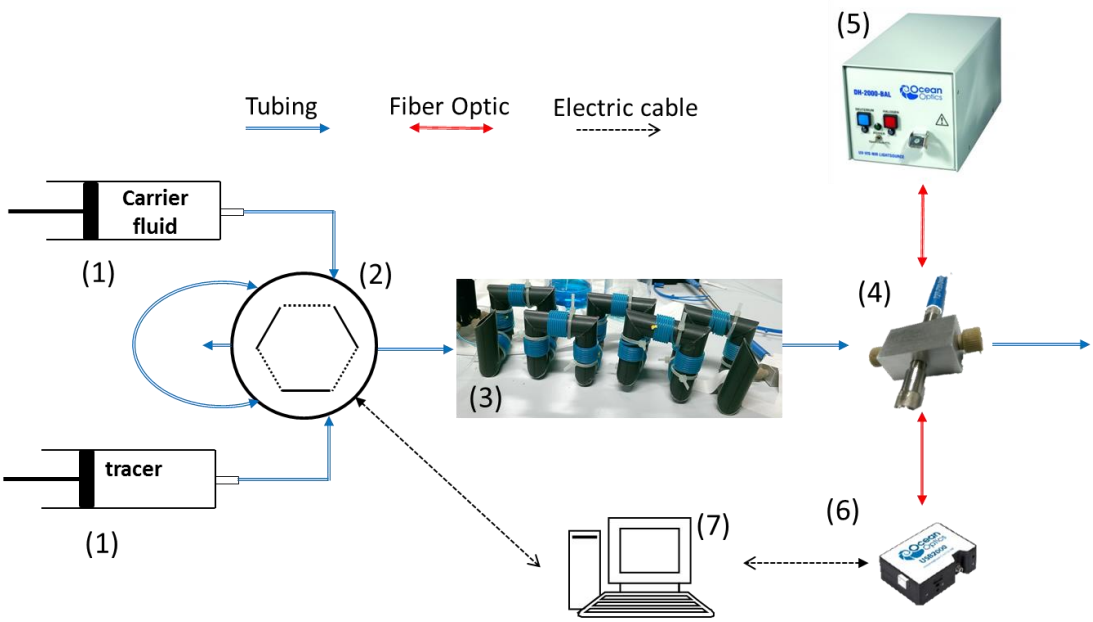

Figure 4.3 – Experimental setup used for RTD experiments comprised of (1) Syringe pump, (2) Injection valve, (3) CFI to investigate, (4) Non-intrusive flow cell, (5) Source light, (6) Spectrometer, (7) Computer for data acquisition.

Note that data smoothing is very important as numerical differentiation amplifies the noise.

The experimental RTDs were then fitted with the solution of the axial dispersion model for small deviation from plug flow to obtain the axial dispersion coefficient :

$$E_{t,ADM} = \sqrt{\frac{u^3}{4\pi D_{ax} L}} \exp\left[-\frac{(L-ut)^2}{4D_{ax}L/u}\right] \qquad \text{Eq. 4.3}$$

where u is the mean axial velocity and L the total length of the capillary forming the CFI or HCT (from injection to detection point). The length of the TEFLON tubing was measured when constructing the structures and the mean internal velocity was calculated as $u = \dot{v}/A_t$ with $\dot{v}$ the volumetric flow rate and A_t the cross-section area of the capillary. The only unknown parameter in Eq. 4.3 is the axial dispersion coefficient that was estimated by means of least squares minimization. The residual error of the fitting (ε defined in 3.3.5) was used to verify the applicability of the model. Note that the conditions of applicability of the ADM in laminar flow, suggested by Anthakrishnan et al. (1965), are only valid for straight pipes where an undisturbed parabolic velocity profile is present. Such conditions are less strict in CFIs and HCTs, because of the modified velocity profile characterized by the Dean roll-cells. As a result, convection contributes to mass transport in radial direction and the contribution is higher as the secondary flow is intensified (e.g. increasing Re). In HCTs a correlation based on empirical data was proposed to verify the conditions of applicability of the model (Eq. 2.40). In CFIs, the contribution of convection to radial mass transfer is expected to be greater as a result of chaotic advection created by the bends. However, correlations similar to that for HCTs are not available in the literature and it is beyond the scope of this work finding one. A general criterion based on the quality of the curve fitting was employed. Validation experiments were conducted in straight capillaries and it was found a direct relationship between the conditions of applicability of ADM and ε (see section 3.3.5). When the latter was greater than 10^{-4} axial dispersion data measured in HCTs and CFIs were excluded. For HCTs the criterion adopted is consistent with the correlation proposed by Trivedi and Vasudeva (1975), as showed in Figure 4.4. The values of τ_{ADM} for the cases investigated in HCTs

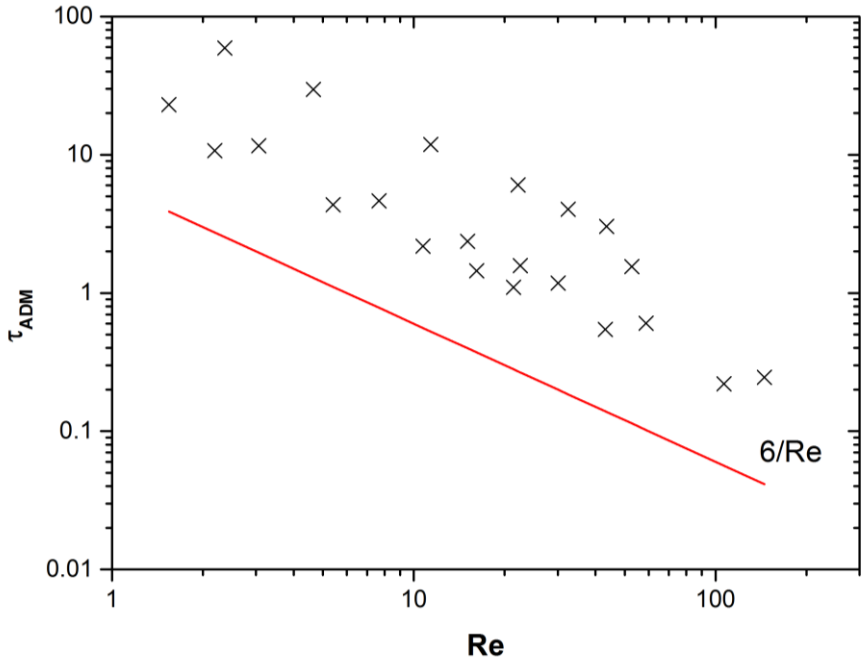

Figure 4.4 – Cross-shaped dots refer to cases investigated in this work for HCTs. The red line shows the values of τ_{ADM} below which the axial dispersion model is not expected to hold (Eq. 2.40.)

are always greater than $6/Re$, value above which the application of the ADM is considered valid .

The validity of the solution for small deviation from plug flow was verified after the fitting. When $N_L > 0.01$, the solution for large deviations from plug (Eq. 3.7) flow was applied to find the value of axial dispersion coefficient.

The extent of axial dispersion can be expressed in dimensionless form in terms of dispersion number N_d

$$N_d = \frac{D_{ax}}{u d_t} \qquad \text{Eq. 4.4}$$

where d_t is the internal diameter of the capillary. Systems with smaller N_d are less dispersive. The adoption of the dispersion number is very convenient because it allows comparing the extent of dispersion measured in CFIs and HCTs with that in straight tubes predicted by the Taylor-Aris equation for dispersion (Eq. 3.15), that can be written as

$$N_{d,TA} = \frac{1}{Re\ Sc} + \frac{Re\ Sc}{192} \qquad \text{Eq. 4.5}$$

with Reynolds and Schmidt number defined as

$$Re = \frac{\rho u d_t}{\mu} \text{ and } Sc = \frac{\mu}{\rho D_m}$$

where ρ and μ are the density and the dynamic viscosity of the fluid respectively and D_m the diffusion coefficient of tracer (Basic Blue 3) in the carrier fluid. The product $Re\ Sc$ is usually referred to as Bodenstein number. The first term on the right hand side of Eq. 4.5 can be neglected as only significant for $Bo < 100$. In this work the Bodenstein number considered ranged between 10^4 and 10^5. Also, the Schmidt number was kept constant as deionized water and aqueous solutions of Basic Blue 3 were used respectively as carrier fluid and tracer. The properties of the fluid were assumed to be those of water at room temperature ($\rho = 997$ kg/m^3, $\mu = 0.001$ Pa s) and the diffusion coefficient of tracer in water was measured with experiments in a straight capillary ($D_m = 6.4 * 10^{-10}$ m^2/s, see section 3.3.5), leading to $Sc = 1677$. Eq. 4.5 can be then rewritten as follows:

$$N_{d,TA} = \frac{Sc}{192} Re = 8.7Re \qquad \text{Eq. 4.6}$$

Eq. 4.6 expresses the relationship between dispersion and Reynolds number for straight pipes. The dispersion number is an increasing linear function of Re for any given Sc.

4.3 Results and discussions

4.3.1 Axial dispersion in HCTs and CFIs

The results of experiments on both CFIs and HCTs with different λ are reported in Figures 4.11-13. The plots show the value of N_d as a function of Re. The corresponding Dean number is calculated and displayed on the secondary axis. As a reference the curve for straight tubes is also reported (Eq. 4.6). The values of axial dispersion number were averaged over three experiments for each set of parameters. The standard deviation is reported as error bars on the data points.

For any value of coil-to-tube diameter ratio, both HCTs and CFIs are less dispersive than straight tubes confirming that the secondary flow plays a major role in defining the dispersion behaviour. The reduction of axial dispersion is as high as 10-fold for the higher values of Reynolds number investigated in CFIs. The dispersion number increases with Reynolds, however with a rate smaller than that of straight tubes. The

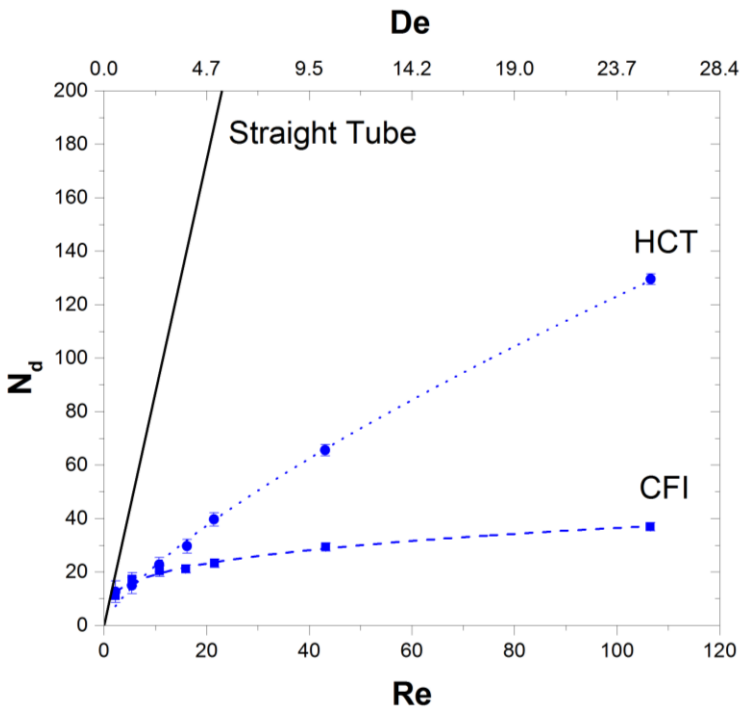

Figure 4.5 – Axial dispersion number as function of Re (primary axis) and De (secondary axis) for CFI (squares) and HCT (circles) with $\lambda = 17.8$. The straight line refers to Eq. 4.6.

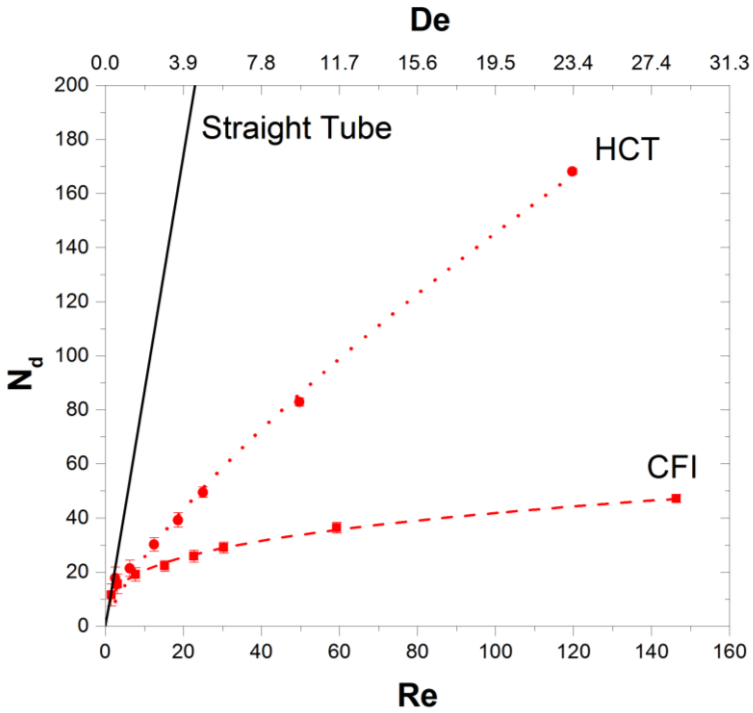

Figure 4.7 – Axial dispersion number as function of Re (primary axis) and De (secondary axis) for CFI (squares) and HCT (circles) with $\lambda = 26.2$. The straight line refers to Eq. 4.6.

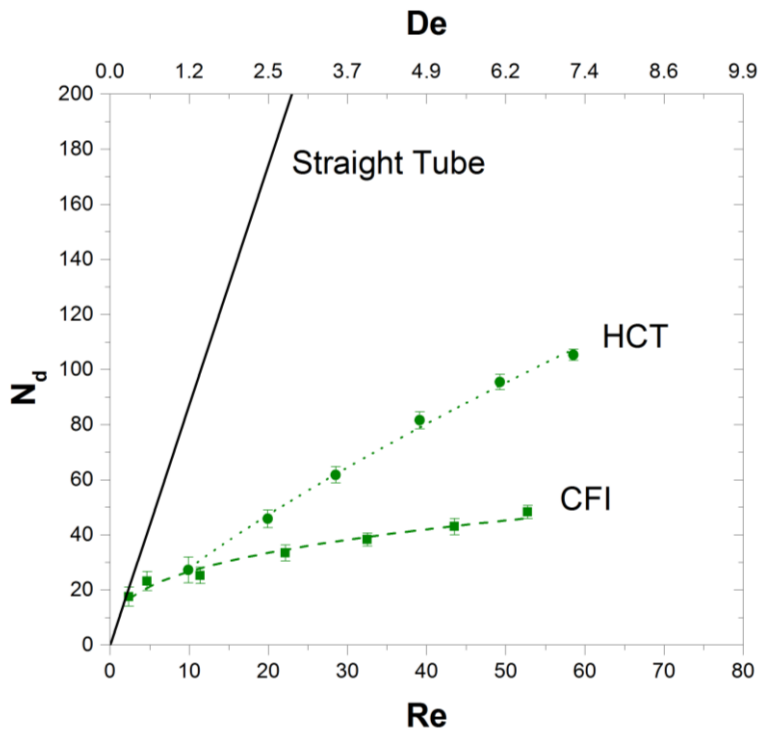

Figure 4.6 – Axial dispersion number as function of Re (primary axis) and De (secondary axis) for CFI (squares) and HCT (circles) with $\lambda = 65.6$. The straight line refers to Eq. 4.6.

rate appears to depend on Re, λ as well as on the type of configuration. The curves for HCTs increase with a smaller rate than those for CFIs, confirming that flow inversions have a strong effect on the dispersion behaviour. It can also be observed that the rate decreases with Re, revealing a different trend as compared with straight tubes, for which the correlation is linear.

As Re tends to zero the dispersion curves for HCTs and CFIs approach the line for straight pipes. This is expected because at low Re the intensity of secondary flow, quantified by De, is modest and the Dean roll-cells, primarily responsible for reducing the dispersion, disappear. The exact value of De below which the dispersion behaviour of HCTs and CFIs equals that of straight tubes cannot be clearly identified due to the lack of experimental data in the low Re region. It can be roughly estimated analyzing the curves reported: it appears that all data point with $De < 0.5$ approach closely the curve for straight tubes. It was suggested in the literature that when $De < 0.25$ one can use the Taylor-Aris dispersion equation to quantify the dispersion in HCTs, validating our findings (Erdogan and Chatwin, 1967; Nigam and Vasudeva, 1976).

For any λ, CFIs are characterized by lower dispersion intensities as compared to HCTs, confirming the pioneering observations of Saxena and Nigam (1984). They reported that significant reduction of axial dispersion was achieved as compared to HCTs. Moreover, they observed that the vessel dispersion number ($N_L = D_{ax}/uL$) did not depend on De, for CFIs with $n_b = 15,\ 30,\ 57$ in the range $2 < De < 60$. Nevertheless, the results presented here are qualitatively different because N_d increases with De, meaning that as the secondary flow intensifies, so does the effect of reduction on the dispersion behaviour. Note that N_d and N_L are qualitatively comparable as $N_L = N_d * (d_t/L)$. The importance of flow inversions to create further radial mixing and in turn to narrow down the RTD lies in the change of direction of the centrifugal force resulting in the Dean roll-cells changing position in the radial direction. In the absence of secondary flow (and therefore of Dean roll-cells) the effect of flow inversion is expected to vanish. However, for $De < 2$ the curves for HCTs and CFIs overlap before approaching $N_{d,TA}$. This suggests the existence of a narrow region ($0.5 < De < 2$) in which the action of centrifugal force is still active on the reduction of axial dispersion, but the Dean roll-cells are not strong enough to create chaotic

mixing at the bends. As a result, when operating in this region HCTs and CFIs have identical performance in terms of axial dispersion.

The curves for HCTs are qualitatively similar to those for CFIs: a continuous increase in N_d can be observed with Re, with a rate dependent on λ. This is partially in contrast with what Trivedi and Vasudeva (1975) observed: the vessel dispersion number of HCTs would reach a maximum for a given value (dependant on λ) of Reynolds number, suggesting that at high Re the dispersion behaviour changes. The authors did not provide a physical explanation to this behaviour. However, the data are not perfectly comparable, as different values of λ were studied and the range of Re investigated in our work was limited to the criterion of applicability of the ADM. Further investigation needs to be carried out to draw conclusions on this aspect.

4.3.2 Effect of coil-to-tube diameter ratio

For the first time, the effect of coil-to-tube diameter ratio was investigated in CFIs. This can be directly examined in Figure 4.8. A significant dependence of N_d on λ can be observed in the range investigated. The dependence is stronger at higher Re. As the

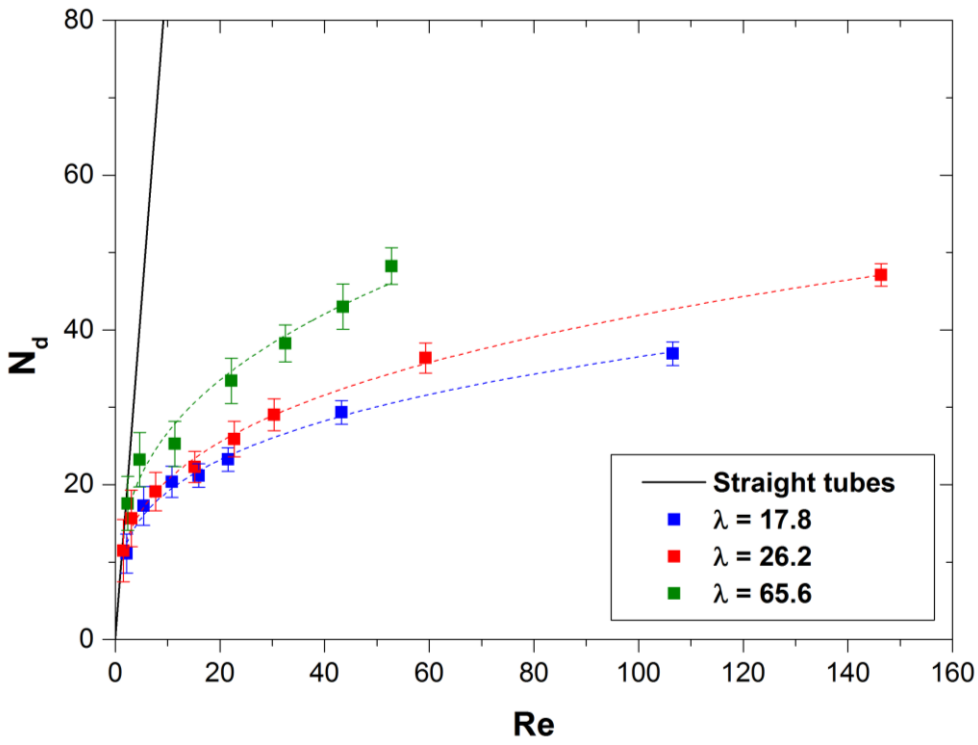

Figure 4.8 – Axial dispersion number as function of Re for CFIs at different λ. The straight line refers to Eq. 4.6.

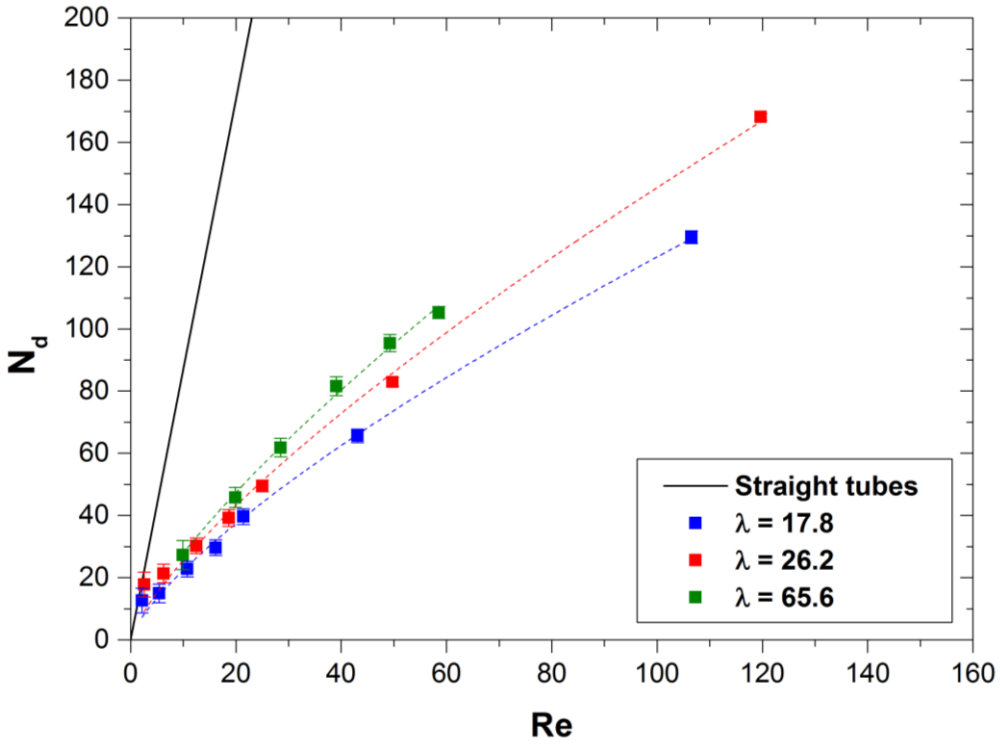

Figure 4.9 – Axial dispersion number as function of Re for HCTs at different λ. The straight line refers to Eq. 4.6.

mean velocity increases (and so Re) the centrifugal force, primarily dependant on λ, acting on the fluid is intensified. This results in stronger recirculation due to Dean roll-cells that is reflected in more effective flow inversions. Conversely, the coil-to-tube diameter ratio has a lower impact on the magnitude of axial dispersion in HCTs (Figure 4.9). This can be explained reminding that in CFIs two mechanisms contribute to the reduction of axial dispersion: (1) Dean roll-cells in the sections of straight helical coils; (2) change of orientation of Dean roll-cells at the bends. As a consequence, for a given Re, when decreasing λ, the stronger secondary flow is manifested in both sections of straight helical coil and at the bends. The second mechanism is absent in HTC explaining the reduced dependence of axial dispersion on λ. These observations suggest that λ can be used more effectively in CFIs as a design parameter to narrow down the RTD for a given Re.

The values of dispersion number obtained experimentally were correlated to Re using a relationship similar to the Taylor-Aris equation for dispersion:

$$N_d = k_1(\lambda) Re^{k_2(\lambda)} \qquad \text{Eq. 4.7}$$

Table 4.2 – Fitted values of k_1 and k_2 for both HCT and CFI.

λ	HCT		CFI	
	k_1	k_2	k_1	k_2
17.8	4.069	0.740	9.978	0.281
26.2	4.499	0.754	10.125	0.308
65.6	4.813	0.763	12.559	0.327

where $k_1(\lambda)$ and $k_2(\lambda)$ are fitting parameters found with a least squares method. The fitted curves are reported as dashed-lines in figures 4.14-15. It was assumed that k_1 and k_2 are only dependent on λ, as any other parameter was kept constant. Note that $k_1(\lambda)$ can also be thought as $Sc\ k_1'(\lambda)$, where $k_1'(\lambda \to \infty)$=1/192. However in this work Sc was kept constant and it was preferred to include it into k_1. The choice of a power law is consistent with the curve trends. The values of k_1 and k_2 are reported for both CFIs and HCTs in Table 4.2.

The proposed equation correlate very well the data in the range investigated. It should be reminded that the values found are only valid for the parameters kept constant in our characterization: n_b, n_t, p, Sc and strictly for the range of Reynolds number considered.

4.4 Conclusions

Axial dispersion in helically coiled tubes and coiled flow inverters was investigated by means of RTD experiments. The widely used axial dispersion model was adopted to quantify the extent of dispersion. The separate effect of coil-to-tube diameter ratio and Reynolds number was studied in terms of axial dispersion number. As result of this work the following conclusions can be drawn:

- Dispersion data obtained by means of experimental RTDs in microfluidic CFIs and HCTs are qualitatively consistent with previous observations in the literature. The work presented in this thesis provide stronger evidence and more quantitative data on the reduction of axial dispersion induced by secondary flow and flow inversions.

- HCTs are characterized by considerable reduction of axial dispersion as compared to straight pipes. The reduction is directly dependent on Re, as effect of stronger centrifugal force for higher flow velocities resulting in more intense secondary flow. Available data in the literature suggest that a change of the dispersion behaviour occurs for a fixed Reynolds number (for any λ), similarly to what happens in straight tubes in correspondence of transition to turbulence (Trivedi and Vasudeva, 1975).To our best knowledge, these observations have not been confirmed yet. In the context of this work, the dispersion number was found to continuously increase with Re. However, the limited range of Reynolds numbers, dictated by the chosen criteria for the applicability of the model does not allow to rule out the possibility of a maximum in the dispersion curves observed in the past.
- Further reduction of axial dispersion can be achieved when introducing bends (CFIs), where the change of direction of centrifugal force induces repositioning of Dean roll-cells. The shift of Dean roll-cells create interchange of fluid elements with different age, thus experiencing a wider range of axial velocities (Saxena and Nigam, 1984). This concept was confirmed in this work as the intensity of dispersion is smaller in CFIs as compared to HCTs having the same number of total turns. It was also observed that when $De < 2.0$ the dispersion of CFIs equals that of HCTs, suggesting that mixing in bends is only effective when secondary flow is enhanced.
- Several design parameters define the performances of CFIs with regard to the dispersion behaviour. The present work focused on the effect of the coil-to-tube diameter ratio, which had not been studied before. The number of bends, number of turns and axial pitch were kept constant to allow a correct comparison. It was observed that for Re up to 100, the intensity of dispersion in CFIs exhibit a stronger dependency on λ than in HCTs. Additionally, for a given Reynolds number, the intensity of dispersion decreases with λ. The coil-to-tube diameter ratio is therefore a crucial parameter when designing CFIs.
- A power law formulation is suggested as a potential correlation for the dispersion number as a function of Reynolds number. It is worth mentioning that in this form the correlation is very similar to the equation of dispersion for straight tubes (Eq. 4.6).

Chapter 5

Conclusions and future works

The work presented in this thesis provides stronger evidence on the reduction of axial dispersion of coiled flow inverters (CFIs) and helically coiled tubes (HCTs) as compared to straight pipes. The available data in the literature were partially confirmed and extended, demonstrating that CFIs are most effective when one is to approach plug flow. RTD experiments were conducted in CFIs and HTCs constructed with TEFLON capillaries on pre-assembled frames and the axial dispersion model was adopted. The experiments were conducted with a detection system specifically developed to carry out studies on microfluidic devices.

In chapter 3, the development of an experimental platform for RTD measurements in microfluidic devices was reported. A standard approach has not been proposed in the literature and measurement techniques are often system-specific. Our objective was to design an experimental setup with which many different microfluidic devices could be investigated interchangeably. In-line absorbance detection with the aid of transparent tubing and suitable flow cells was employed. In a first stage, the detection system consisted of a photodiode and a LED light source (both working in the infrared range) attached to a PEEK cross junction. Aqueous solutions of copper sulphate, having absorbance peak in the infrared were used as tracer. Experiments in straight capillaries revealed the RTDs to be dependent on the copper sulphate concentration. The nature of the tracer and possible interaction with the tubing walls could explain this unexpected behaviour. This has never been reported in the literature and suggests that electrolytes, such as copper sulphate, may be not suitable as tracer in TEFLON based systems with through-the-wall measurements. A complete modification of the detection system was needed for the adoption of a different tracer. Commercial spectrometers, allowing to work in a wide range of wavelengths, were employed. Intrusive commercial flow cells were tested but showed to produce poor reproducibility as well as unexpected curvature changes of the F curves. The

importance of avoiding wetting parts was demonstrated when running experiments in custom-designed non-intrusive flow cells. A calibration campaign was conducted to establish the concentration of Basic Blue 3 (employed as tracer) lying in the region of validity of the Lambert-Beer law when capillaries with different internal diameter are to be used. With this tracer concentrations as low as 50 mg/L are sufficient to perform step input experiments with a high degree of repeatability. Validation experiments in straight capillary, for which Taylor's equation for dispersion holds, showed high reproducibility and RTDs independent of the tracer concentration. Experiments were also carried out to measure the molecular diffusion coefficient of the tracer in water and to generate a criterion for the applicability of the axial dispersion model in systems different than straight tubes.

In this work, the effect of the coil-to-tube diameter ratio and Reynolds number was p investigated employing the RTD platform developed. The former was found to influence the intensity of dispersion more significantly in CFIs than HCTs. This demonstrates that flow inversions are extremely effective on narrowing down the RTD. However, it was also observed that the flow inversions are active only for Dean numbers above 2. The operating Dean number can be tuned by changing either the Reynolds number or the coil-to-tube diameter ratio. The former is often dictated by the operating conditions (flow rate, properties of the fluid) of the process. For a fixed Reynolds number the coil-to-tube diameter ratio must be as small as possible. However, using standard manufacturing techniques (supporting structures) it is not easy to design CFIs with λ smaller than 10. The recent development of 3D printing techniques offers new opportunities for less constrained CFIs designs and manufacturing. CFIs with small coil-to-tube diameter ratios could be constructed allowing to characterize more extensively the effect of this parameter on the dispersion behaviour.

For CFIs to be adopted on a larger scale, it would be useful to obtain correlations relating the dispersion number to design and operating parameters. In this work, it was found that N_d correlate with the Reynolds number according to a power law formulation. This was obtained for fixed values of Schmidt number, number of bends and number of turns. More extensive data need to be derived to validate our findings and to understand the functional relationship of the other parameters involved.

As a result of the enhanced mixing and reduced hydrodynamic dispersion, CFIs could be employed as high-performance reactors for continuous processes involving particle formation, such as nanoparticle synthesis and crystallization. In recent years, these operations, traditionally conducted in batch reactors are being implemented into continuous milli- and micro- fluidic systems in an effort to achieve improved controllability, specifically on the final particle size distributions (PSDs). For this reasons, narrow residence time distributions are to be attained, allowing particles to grow for even times. The experimental work conducted in this thesis provides additional evidence that CFIs are promising solutions for such operations.

Appendix A

A step-by-step guide to RTD experiments with the experimental platform developed

This section aims to provide a practical and detailed guide to perform RTD experiments on the platform developed. This section is divided into four different subsections:

1. **General description of the setup:** this section provides an explanation of the constituting components, the working principles and the potential application of our setup.
2. **Brief guide to absorbance measurements:** this section provides a brief theoretical introduction on absorbance measurements,
3. **Step-by-step guide to experimental procedure:** in this section we explain in detail how to perform an experiment and how to export the data.
4. **A guide to post-processing**: this section provides a brief description of each MATLAB script developed for post-processing.

A.1 General description of the setup

This setup has been developed with the aim of having a flexible and reliable platform to perform residence time distributions measurements on microfluidic devices. A schematic of the experimental setup is reported in Figure A. and a description of the components follows. The schematic representations refer to the case of a single detection point placed at the outlet of the microfluidic device. The setup can be adapted easily to perform measurements with two detection points with an additional flow cell positioned close to the inlet of the microfluidic system. All components were purchased for the setup with two detection points: two flow cells, two spectrometers for synchronous measurements and a bifurcated optical fiber.

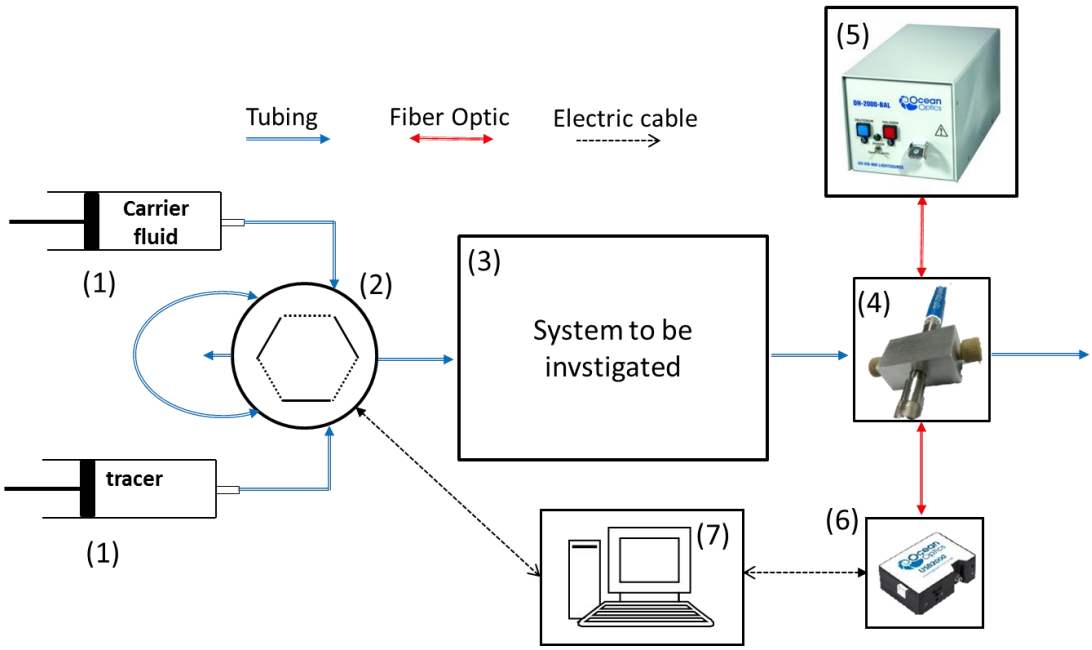

Figure A.1 – Schematic representation of RTD detection system with a single detection point.

(1) Pump. Both the carrier fluid and the tracer should be pumped at the desired flowrate. Any pump can be used for this purpose, however it is suggested to employ dual syringe pumps (e.g., Harvard Apparatus PhD Ultra). The advantages of using a syringe pump lie on the reduced flow oscillations, the precise flow rate and the possibility of using a single pump for both fluids, minimizing the risk on imperfect flow rate calibration. The only drawback is represented by the size of the syringes (usually not bigger than 100 ml). Note that, depending on the extent of dispersion, the syringes should be no smaller than twice the internal volume of the system to be investigated.

(2) Injection valve. The injection of a tracer is the basic working principle of RTD experiments. Any kind of injections can be used with this setup and one should select accordingly a suitable injection. This setup has been extensively used and validated for step input experiments using a 6-port valve to perform sharp step stimulus. Specifically, the configuration of the 6 port valve has been adapted to obtain a sharp switch between carrier fluid and tracer at any given time. A schematic representation of the valve setup is reported Figure A.2.

When the pump is in load position the carrier fluid is delivered to the downstream system to be investigated. As soon as the valve is manually

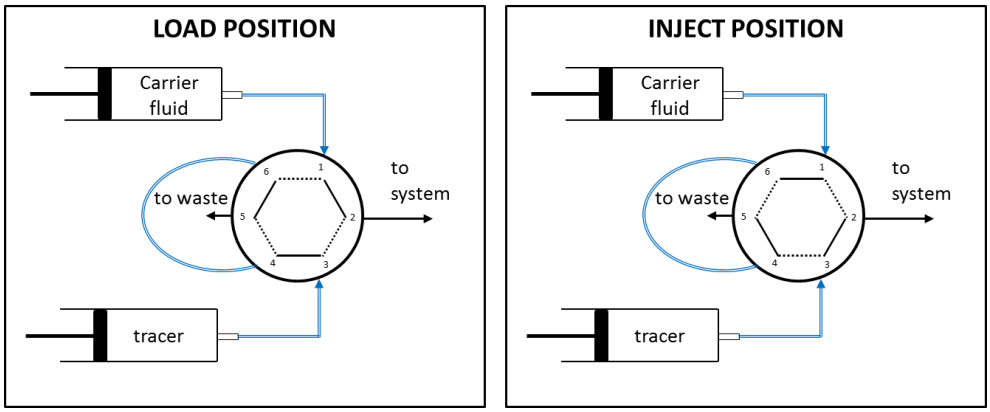

Figure A.2 – Schematics of 2-positions 6-way injection valve.

switched, the tracer is delivered to the downstream system while the carrier fluid goes to waste. The numbers reported on Figure A. refers to the ports of a V-451 injection valve (Upchurch Scientific). This port is also equipped with a magnetic sensor to trigger the absorbance acquisition on the spectrometers. However, using the spectrometer in triggering mode has some major limitations on the integration time of the spectrometers. An alternative way of recording the injection time relies on a separate stopwatch.

(3) System to be investigated. As stated above the main idea behind this setup is the possibility to easily change the microfluidic devices to be investigated. Both compact microstructures (i.e., microchips) and capillary-based systems can be analyzed. In the first case, suitable tubing connections both for the injection-inlet and outlet-detection sections need to be used. In the case of a capillary-based system the inlet of the system can be directly fitted into the injection valve, where the desired injection takes place. Similarly, the detection point can be placed at the outlet section of the system.

(4) Flow cell. This in-house designed flow cell allows non-intrusive through-the-wall absorbance measurements. The Teflon tubing is inserted in one of the holes (1.6 mm through-hole for 1/6 in OD tubing). The other two ends are instead fitted with the fiber optics connected to the light source and the spectrometer respectively. The flow cell has been manufactured in aluminum to isolate the optical path from external light. A representative drawing dimensions is reported in Figure A.3 for future manufacturing.

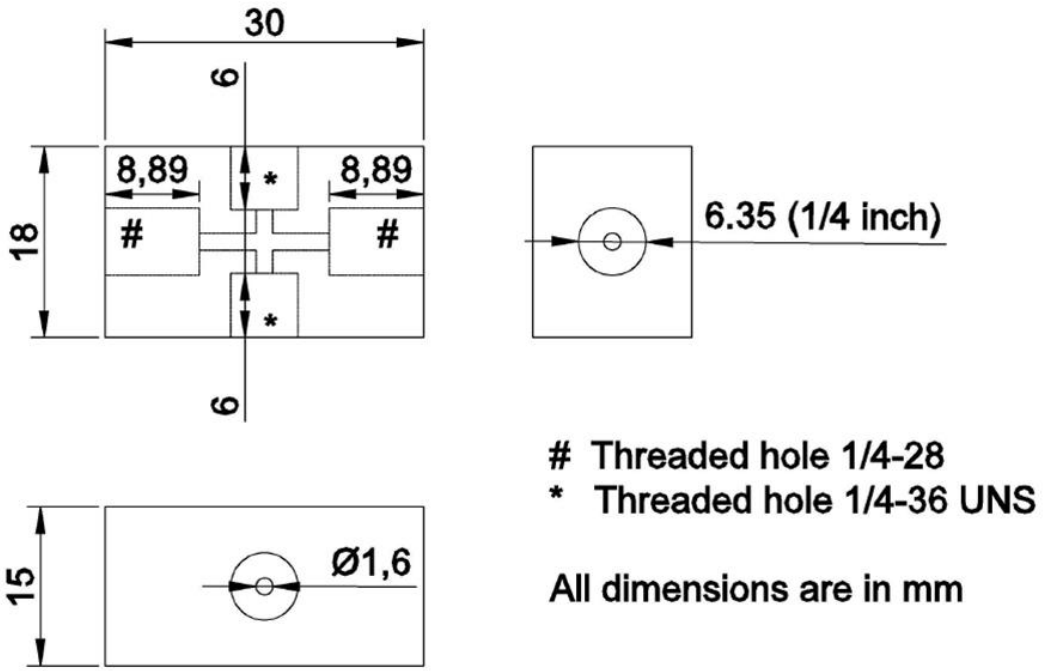

Figure A.3 – Drawing of the flow cell comprehensive of detailed dimensions.

(5) Light source. A light source is needed for absorbance measurements. The available light source is an Ocean Optics DH-2000-BAL with broadband emission between 230 and 2500 nm. A 2m long 600 um ID fiber optics (Ocean Optics) is used to connect the light source with one end of the flow cell. In the case of measurements with two detection points, a bifurcated optical fiber was purchased and can be used.

(6) Spectrometer. This is the core of the experimental setup allowing to measure the concentration of tracer over time. The measurements rely on UV-VIS spectroscopy allowing the adoption of any couple carrier-fluid/tracer with absorption peak between 200 and 850 nm. The spectrometer is connected to the one end of the flow cell through a 25 cm long 600 um ID fiber optics (Ocean Optics). It is connected to a computer via USB. The basic reading of the spectrometer is the intensity spectrum over the whole range of wavelengths. This represents the count of photons hitting the different sensors, each absorbing light in a very narrow range of wavelengths.

(7) Computer. The computer needs to be equipped with Spectra Suite software.

The guide refers to step input experiments in single phase flow in capillary based systems. To this end, we include a step-by-step guide to perform experiments as well as a brief description of the post-processing scripts written in MatLab . However, the setup can be adapted to carry out different RTD experiments, such as:

- *Single-phase in compact chip devices*: include suitable connections trying to minimize the length of these section for more precise measurements.
- *Multi-phase slug flow:* the introduction of a second phase (either gas or liquid) implies the development of appropriate signal processing to discard the absorbance reading referring to the disperse phase (i.e., usually the tracer is soluble in the continuous phase). These type of experiments can be carried out both on capillary-based and compact chip systems. In the latter case, one needs to make sure that connections do not alter the stability of the flow. However the experimental procedure will be the same as that for single phase experiments.

A.2 Brief guide to absorbance measurements

RTD measurements are based on the injection of an inert tracer into the system at the inlet. The concentration of the tracer is changed with a known function (e.g. pulse, step inputs, etc.) and the response is found by measuring the concentration of the tracer at the outlet. A suitable detection technique must be employed to be able to record in-line the concentration of the tracer over time. Optical measurements are particularly suitable for microfluidic devices as a result of optical transparency (often encountered in microfluidics) and reduced dimensions, ensuring short optical path-lengths and in turn enhanced sensitivities. The light absorption properties of the tracer can be exploited performing suitable absorbance measurements. The absorbance (A) is a measure of the light attenuation resulting from absorption of light and it is defined as

$$A = -\log_{10}\frac{I}{I_0} = -\log_{10} T \qquad \text{Eq. A.1}$$

where I is the intensity of light reaching the detector and I_0 is the incident light or a reference light intensity (if properly designed, the absorption contribution of the suspending medium is negligible and $I_0 = I_R$) and T is the trasmittance.

The relationship between the absorbance and the concentration of a chemical species to be detected (the tracer) is expressed by the Lambert-Beer law:

$$A = \epsilon\, l\, c \qquad \text{Eq. A.2}$$

where ϵ is the extinction coefficient of the tracer, l the optical path length and c the concentration of tracer. Note that the extinction coefficient depends on the wavelength of the light: each chemical species absorbs light more intensely at different wavelength. The Lambert-Beer law reveals that there exists a linear relationship between absorbance and concentration. As a result we can directly use absorbance-time data to obtain the RTD. Nevertheless, the validity of the Lambert-Beer law is limited to low concentrations of tracer. For any detection system, tracer and suspending medium, a maximum value of concentration can be found above which Eq. A.2 does not hold. Calibration experiments need to be carried out to identify the region (in terms of concentration) of validity of the Lambert-Beer law. This step is very important because absorbance measurements obtained under non-linear conditions would produce erroneous RTDs.

A calibration campaign was conducted on the detection system described in this guide using Basic Blue 3 as tracer (CAS 33203-82-6). The calibration was carried out using PTFE capillaries with different internal diameters. Note that the walls of the capillaries contribute to light reflection with magnitude that depends on their thickness. It was found that 75, 100, 200 mg/L are the maximum concentrations of Basic Blue 3 in water respectively for 1.00, 0.8 and 0.5 mm ID PTFE tubing. Other tracer were also tested (Methylene Blue, Waterman Ink), but the calibration curves are not available.

A.3 Step-by-step guide to experimental procedure

Notes on setting up operations

- The capillary needs to be fitted into the flow cell, which is then pulled over and placed at the desired distance from the injection. Prior to this operation, it is necessary to thoroughly clean both the flow cell and the capillary to lower the

risk of dust particles obstructing the optical window. It is also suggested to secure the position of the flow cell along the tubing using nuts and ferrules on both sides. The flow cell is equipped with standard Upchurch threads for 1/8 in. nuts, suitable for 1/16 in. tubing.

- Make sure that all fluid connections are tightly fitted to prevent unwanted air bubbles to enter the system resulting in noisy absorbance measurements. Similarly, when loading the syringes with carrier fluid and tracer, remove unwanted air.
- Bending of optical fiber must be minimized to reduce the attenuation of light (primarily dependent on the bending angle) and to avoid damaging (above a certain angle the optical fiber breaks!). The short optical fiber connecting the flow cell to the spectrometer is particularly fragile.
- It is very important that all the components are immobilized on the working bench, particularly the optical fibers connected to the flow cell. Note that accidental motion of the optical fibers would alter the incident light and/or the portion of light travelling from the flow cell to the spectrometer. As a result the absorbance reading would change and affect the measurement.

Experimental protocol

- Switch on the source light while completing setting up operations. Both lamps must be switched on and the shutter should be closed while warming up. For the light source to reach a constant light intensity it is necessary to let it to warm up for at least 30 minutes.
- Wash the microfluidic device with plenty of carrier fluid at high flow rate to clean from impurities and/or tracer injected in previous experiments.
- Fill one syringe with carrier fluid and the other syringe with tracer verifying that both are loaded with the same amount of liquid. Place the syringes on the pump and make sure to connect them to the appropriate port of the valve (as shown in Figure A. for step input experiments).
- Open the Spectrasuite software on the computer connected to the spectrometer. The software automatically detects the spectrometers and shows the intensity spectrum as default. To create an absorbance measurement in the *File* tab select

New/Absorbance measurement. The wizards window opens and leads to the following steps:

1. Select the source spectrometer, if more than one spectrometers is plugged.
2. Insert the acquisition parameters. The integration time needs to be specified. This can be thought of as the shutter time of a camera and defines the frequency of the acquisition. The integration time need to be adjusted according to maximum photon count. The spectrometers become saturated and stop acquiring data when at any wavelengths the photon counts exceeds 65000. The integration time can be adjusted manually checking the *preview spectrum* in the wizard. A common value of maximum integration time is 10 ms for our system. However, this depends on the tubing adopted. Integration times lower than the maximum can be used; however, this will limit the sensitivity, as the photon count will be lower. It is therefore suggested to set as integration time the maximum value above which saturation occurs. Note that the integration time defines also the distance between data points in the final absorbance-time data. To reduce the number of data points one can use the option *scans to average,* set on 1 as default. For example when the integration time is 10 ms, selecting 10 in the *scans to average* tab, the absorbance reading would be updated every 100 ms with an average value of the previous 10 readings.
3. Take a *reference spectrum.* This is the intensity spectrum when the capillary is filled with pure carrier fluid (no tracer). Before storing the spectrum, make sure that the **shutter** of the source light is **open**.
4. Take a *dark spectrum*. This is the intensity spectrum in dark conditions to account for the external light penetrating into the flow cell. Before storing the spectrum, make sure that the **shutter** of the source light is **closed**. Note that the flow cell was designed to prevent external light entering the optical path, however, a small fraction of light might enter through the capillary. Nevertheless, the dark spectrum should be characterized by very low photon counts (200 to 500) at any wavelength.

At this stage an absorbance spectrum is created showing zero for any wavelength in the operating range of the spectrometer (200-800 nm). It is then necessary to create a graph recording the values of absorbance at the desired wavelength over time. Click on the *strip-chart* button to open the wizard window. It is suggested to select the option *Average* in the *Range Selection* tab. Instead of a single wavelength, the software would produce an averaged value of absorbance over the range of wavelength selected. This should be chosen around the absorbance peak of the tracer adopted. The absorbance peak of Basic Blue 3 is at 650 nm. The suggested average range is 645-660 nm. Do not change any other setting and click on *Next* to close the wizard. A new graph is created reporting the value of absorbance (averaged between the selected wavelengths) changing over time.

- Select the desired flow rate on the pump and start dispensing the fluid with the injection valve in the load position. The carrier fluid will be delivered to the microfluidic device while the tracer will go directly to waste.
- Switch the valve to the inject position to introduce the tracer. Using the configuration shown in Figure A. a step input is performed. However, the 6-way valve equipped with a suitable sample loop can also be used for pulse input experiments. In case of pulse input experiments the experimental procedure will be the same.
- It is possible to control the acquisition with a magnetic sensor mounted on the injection valve and connected to the spectrometer. When switching the pump a signal will be sent to the spectrometer and the acquisition will start. To do so it is necessary to tick the *External Trigger* box on the absorbance spectrum toolbar. Note that this option is only available when the integration time is set to 50 ms. When using this option the time at which the injection was performed will correspond to time zero on the strip chart. If a different integration time is to be used, the acquisition needs to be started manually before the injection. In this case it is also necessary to record with the aid of a stopwatch the time elapsed from the acquisition start to the injection time for the post-processing procedure. To start the acquisition, press the *start* button on the strip-chart toolbar.

- For step input experiments to be considered concluded check the strip-chart and make sure that the absorbance reached a plateau. This means that the maximum concentration of tracer (as the tracer solution loaded into the syringe) is flowing at the detection point.
- To export the absorbance-time data click on the *save* option on the strip-chart toolbar. Select the desired directory for the file to be saved and name the file as "*filename.csv"*. Make sure to include the extension "*.csv*". A file containing three columns will be saved: (1) exact time, (2) elapsed time from acquisition, (3) absorbance.

A.4 MATLAB scripts for post-processing

MATLAB scripts were developed to perform post–processing analysis of absorbance-time data. The full scripts can be found in Appendix B and are provided with operating comments. A brief description of each script follows. The title of the script is indicated with the suffix **.m**

1. **Fcurve.m -** Script to obtain F curve from absorbance-time data for step input experiments. Import data from .csv file, rescale times for multiple injections, normalize absorbance to obtain F curves, write to new data-arrays and save to new Matlab matrix. Inputs needed: (a) *filename:* name of the .csv file; (b) *foldername_read:* name of the folder where the .csv file is located; (c) *foldername_write:* name of the folder where the matrix with processed data will be saved; (d) *injection_times:* vector containing the elapsed times from start of acquisition of first injection, following injections, end of experiment.
2. **Ecurve.m** – Script to calculate E curves. Read F curves matrix previously generated, perform smoothing, calculate E curve, calculate mean residence time and variance. The E curve are then saved to a new MatLab matrix. Inputs needed: (a) *filename:* name of the original .csv file; (b) *foldername:* name of the folder where the F curve matrix is located.
3. **ADMfitting.m** – Perform fitting of experimental E curve with solutions of axial dispersion model. Both solutions for small and large deviations from plug-flow are implemented (Levenspiel, 1999). Inputs needed: (a) *filename:*

name of the original .csv file; (b) *foldername:* name of the folder where the E curve matrix is located; (c) *flowrate:* value of flowrate used for experiment in ml/min; (d) *L:* length of the tubular reactor in m; (e) *d_t:* internal diameter of the tubing in mm; (f) *Dm:* molecular diffusion coefficient of tracer in carrier fluid in m^2/s.

4. **ImportFile.m** – Auxiliary function to import data from .csv files
5. **CreateFigure.m** – Auxiliary function to generate plots of E curves.

Appendix B

MATLAB scripts for RTD experiment post-processing

This section contains MATLAB scripts used for post-processing of step input experiments with UV-VIS spectroscopy.

Fcurve.m

```
%% Main m-file to read *.csv files exported by Spectrasuite and write F
%% curve to new MatLab matrix file. It works in the general case of multiple
%% injections
clear all
%% Variable input
%
% Filename used to create .csv file
filename = ['exp1'];
% Name of folder where .csv files are located. (
foldername_read = ['Data'];
% Name of subfolder where to write the data matrix created in the working
% directory. The name may refer to the parameter investigated (e.g. flow
% rate). In this folder a subfolder must be created named as 'filename'
%
foldername_write = ['1mLmin'];
% Injection times/end: insert below the sequence of elapsed times from
% starting of acquisition after each single injection as well as the final
% elapsed time
inj_time = [10.0    100.0];
%
%% Import files recalling ImportFile.m
%
[time,Abs] = ImportFile([foldername_read '\' filename '.csv']);
%
%% Separate data of multiple injection
%
N_inj = length(inj_time)-1;
%
for i=1:length(inj_time)-1
    i_start(i) = find(time >= inj_time(i),1,'first');
    i_end(i) = find(time <= inj_time(i+1),1,'last');
end
%
%% For loop to write to new matrix Abs_data
%
POS=0; NEG=0;
for i=1:N_inj
    %
    if ceil(i/2)-i/2 > 0
        %%Write to variable positive steps
        % First column: time
        % Second column: absorbance
        % Third column: normailized absorbance (F curve)
        Abs_data(:,1) = time(i_start(i):i_end(i))-time(i_start(i));
        Abs_data(:,2) = Abs(i_start(i):i_end(i));
```

```
        Abs_data(:,3) = (Abs_data(:,2)-
min(Abs_data(:,2)))/max(Abs_data(:,2));
        % Save Abs_data matrix to folder with the same filename created in
        % the working directory
        POS = POS+1;
        save([foldername_write '\' filename '\' 'Abs_data_POS_'
num2str(POS)],'Abs_data','inj_time')
        clear Abs_data
    else
        %%Write to variable negative steps
        % First column: time
        % Second column: absorbance
        % Third column: normailized absorbance (W curve)
        % Fourth column: F = 1-W
        Abs_data(:,1) = time(i_start(i):i_end(i))-time(i_start(i));
        Abs_data(:,2) = Abs(i_start(i):i_end(i));
        Abs_data(:,3) = (Abs_data(:,2))/max(Abs_data(:,2));
        Abs_data(:,4) = 1-Abs_data(:,3);
        % Save Abs_data matrix to folder with the same filename created in
        % the working directory
        NEG = NEG + 1;
        save([foldername_write '\' filename '\' 'Abs_data_NEG_'
num2str(NEG)],'Abs_data','inj_time')
        clear Abs_data
    end
end
%%%%%%%%%%%%%%%%%%%%%%%%%%%%%%%%%%%%%%%%%%%%%%%%%%%%%%%%%%%%%%%%%%%%%%%%%%%%%%
```

Ecurve.m

```
%% Main m-file to anlyse RTD experimental data from F curve
clear all
%% Variable input
% Name of the folder where Fcurve_POS1.m is located
folder_name = '1mLmin';
% Original name of the .csv file
file_name = 'Exp1_POS_1';
% Input 1 for positive injectios. Input 0 for negative injections
POS = 1;
% Span: number of data points for smoothing
span = 50;

%% Open Fcurve_POS1.m
load([folder_name '\' file_name '\Fcurve_' file_name],'Abs_data')
%
%% Allocate imported array to column variable names
Time = Abs_data(:,1);
if POS==1
    Abs = Abs_data(:,3);
else
    Abs = Abs_data(:,4);
end
%
%% Smooth F curve
%
Abs_smooth = smooth(Time,Abs,span);
n = ceil(length(Abs_data(:,1))/2000);
Time = downsample(Time,n);
dt=diff(Time);
Abs_smooth = downsample(Abs_smooth,n);
%
%% Differentiate the concentration and normalize
%
dAbs = diff(Abs_smooth)./dt;
```

```
dTime = Time(1:end-1)+dt./2;
E_t = dAbs_/sum(dAbs.*dt);
% Normalization accounting for drifting of signal
slope=(mean(E_t(end-50:end))-mean(E_t(1:50)))/dTime(end);
E_t = E_t - slope.*dTime;
%
%% Plot E_t
%
disp_name= file_name;
plot_name = 'Residence Time Distribution';
x_label = 'Time (s)';
y_label='E';
%
CreateFigure(dTime,E_t,plot_name,x_label,y_label,folder_name,disp_name)
clearvars plot_name x_label y_label disp_name
%
%% Calculations:mean residence time and variance
% Calculate mean residence time
t_mean= trapz(dTime,E_t.*dTime)
% Calculate variance
sigma = trapz(dTime,E_t.*(dTime-t_mean).^2)
%
%% Calculation of RTD in dimensionless domain
%
theta = dTime/t_mean;
E_theta = E_t*t_mean;
%
%% Write to RTD data and save
% RTD_data
% First column: time (s)
RTD_data(:,1) = dTime;
% Second column: E_t (1/s)
RTD_data(:,2) = E_t;
% Third column: theta (dimensionless)
RTD_data(:,3) = theta;
% Fourth column: E_theta (dimensionless)
RTD_data(:,4) = E_theta;
%
save([folder_name '\RTD_data_'
file_name],'RTD_data','F_data','t_mean','sigma')
%
%%%%%%%%%%%%%%%%%%%%%%%%%%%%%%%%%%%%%%%%%%%%%%%%%%%%%%%%%%%%%%%%%%%%%%%%%%%%%%%
```

ADMfitting.m

```
%% This is the main m-file to perform fitting of RTD data with ADM
%
clear all
%% Variable input
%
% Name of the folder where Ecurve_POS1.m is located
folder_name = '1mLmin';
% Original name of the .csv file
file_name = 'Exp1_POS_1';
% Flowrate used for experiment
flowrate = 1.0;
% Internal diameter of tubular vessel  [mm]
d_t = 1.0;
% Length of tubular vessel investigated [m]
L = 5.0;
% Molecular diffusivity of tracer in carrier fluid
Dm = 6.4E-10; %[m2/s]
%
%% Import data and preliminary calculations
```

```
load([folder_name '\' filename '\RTD_data_' file_name])
time = RTD_data(:,1); Et_exp = RTD_data(:,2);
% Calculate mean internal velocity
d_t = d_t*10^-3; A = pi*d_t^2/4;
flowrate = flowrate*10^(-6)/60;
u = flowrate/A;
% Calculate axial dispersion coefficient with Taylor-Aris eq. as first
% value for fitting
Dax_0 = u^2*d_t^2/(192*Dm);
% Estimate vessel dispersion number
Nl_0 = Dax_0 / (u*L)
%
%% Calculate Dax through least square fitting
%

%% RTD curve - t domain - small deviation - N_d < 0.01 open open
options = optimset('TolFun',1e-12,'TolX',1e-
12,'Diagnostics','on','Display','iter');
% Function handling
fun_sd = @(Dax_sd_fit,time) sqrt(u.^3./(4*pi*Dax_sd_fit*L))*exp(-(L-
u*time).^2./(4*Dax_sd_fit*L./u));
% Dax fitting
[Dax_sd,RESNORM_sd,RESIDUAL_sd,exitflag_sd] =
lsqcurvefit(fun_sd,Dax_0,time,Et_exp,0,Inf,options);
% Vessel dispersion number
NL_sd = Dax_sd/(L*u);
% Dispersion number
Nd_sd = Dax_sd/(L*u);
% Re-calculate curve and plot
Et_ADMsd = sqrt(u.^3./(4*pi*Dax_sd*L))*exp(-(L-u*time).^2./(4*Dax_sd*L./u));
plot4 = plot(time,Et_ADMsd,'r');
set(plot4(1),'DisplayName','Small deviations - fitted');
%
% RTD curve - t domain - large deviation - N_d > 0.01 open open
options = optimset('TolFun',1e-12,'TolX',1e-
12,'Diagnostics','on','Display','iter');
% Function handling
fun_ld = @(Dax_ld_fit,time) u./sqrt((4*pi*Dax_ld_fit*time)).*exp(-(L-
u*time).^2./(4*Dax_ld_fit*time));
%
[Dax_ld,RESNORM_ld,RESIDUAL_ld,exitflag_ld] =
lsqcurvefit(fun_ld,Dax_0,time,Et_exp,0,Inf,options); %
% Vessel dispersion number
NL_ld = Dax_ld/(L*u);
% Dispersion number
Nd_ld = Dax_ld/(L*u);
% Re-calculate curve and plot
Et_ADMld_oo = u./sqrt((4*pi*Dax_ld*time)).*exp(-(L-
u*time).^2./(4*Dax_ld*time));
plot5 = plot(time,Et_ADMsd_0,'b');
set(plot5(1),'DisplayName','Large deviations - fitted');
%
%% Save data
%
save([folder_name '\RTD_fitted_ADM_' file_name])
%%%%%%%%%%%%%%%%%%%%%%%%%%%%%%%%%%%%%%%%%%%%%%%%%%%%%%%%%%%%%%%%%%%%%%%%%%%%%%%
```

ImportFile.m

```
%% Auxiliary function to import absorbance-time data from .csv files
function [Time,Abs] = importfile(filename, startRow, endRow)
%IMPORTFILE Import numeric data from a text file as column vectors.
%   [ELAPSEDTIME,ABSORBANCEABSORBANCE] = IMPORTFILE(FILENAME) Reads
%   data from text file FILENAME for the default selection.
```

```
%
%   [ELAPSEDTIME,ABSORBANCEABSORBANCE] = IMPORTFILE(FILENAME,
%   STARTROW,ENDROW) Reads data from rows STARTROW through ENDROW of
%   text file FILENAME.
%
% Example:
%   [ElapsedTime,AbsorbanceAbsorbance] =
%   importfile('L500cm_005mlmin_BB.csv',6, 8280);
%
%    See also TEXTSCAN.
%% Initialize variables.
delimiter = '\t';
if nargin<=2
    startRow = 6;
    endRow = inf;
end

%% Format string for each line of text:
%   column2: double (%f)
%   column3: double (%f)
% For more information, see the TEXTSCAN documentation.
formatSpec = '%*s%f%f%[^\n\r]';

%% Open the text file.
fileID = fopen(filename,'r');

%% Read columns of data according to format string.
% This call is based on the structure of the file used to generate
% this code. If an error occurs for a different file, try
% regenerating the code from the Import Tool.
dataArray = textscan(fileID, formatSpec, endRow(1)-startRow(1)+1,
'Delimiter', delimiter, 'EmptyValue' ,NaN,'HeaderLines', startRow(1)-1,
'ReturnOnError', false);
for block=2:length(startRow)
    frewind(fileID);
    dataArrayBlock = textscan(fileID, formatSpec, endRow(block)-
startRow(block)+1, 'Delimiter', delimiter, 'EmptyValue' ,NaN,'HeaderLines',
startRow(block)-1, 'ReturnOnError', false);
    for col=1:length(dataArray)
        dataArray{col} = [dataArray{col};dataArrayBlock{col}];
    end
end
%% Close the text file.
fclose(fileID);
%% Allocate imported array to column variable names
Time = dataArray{:, 1};
Abs = dataArray{:, 2};

%%%%%%%%%%%%%%%%%%%%%%%%%%%%%%%%%%%%%%%%%%%%%%%%%%%%%%%%%%%%%%%%%%%%%%%%%%%
```

CreateFigure.m

```
%% Auxiliary function to plot data
function CreateFigure(X_1,Y_1, plot_name,x_label,y_label,filename,disp_name)
%CREATEFIGURE(X1,YMATRIX1)
%  X1:  vector of x data
%  YMATRIX1:  matrix of y data

% Create figure
figure1 = figure('Name',[plot_name ' - ' filename],'NumberTitle','off');

% Create axes
axes1 = axes('Parent',figure1,...
    'Position',[0.101850809289233 0.11 0.775 0.815]);
```

```
box(axes1,'on');
hold(axes1,'all');

% Create multiple lines using matrix input to plot
plot1 = plot(X_1, Y_1,'Marker','o');
set(plot1(1),'Color',[1 0 0],'DisplayName',disp_name);

% Create xlabel
xlabel(x_label,'FontWeight','bold','FontSize',12,'FontName','Arial');

% Create ylabel
ylabel(y_label,'FontWeight','bold','FontSize',12,...
    'FontName','Arial');

% Create title
title(plot_name,'FontSize',16,'FontName','Arial');
%%%%%%%%%%%%%%%%%%%%%%%%%%%%%%%%%%%%%%%%%%%%%%%%%%%%%%%%%%%%%%%%%%%%%%%%%%%%
```

Appendix C

Numerical RTDs by means of particle tracking

In recent years, only a limited number of studies have been devoted to develop procedures for the numerical characterization of RTDs in microfluidic devices. Despite the need for numerical modelling as predictive tool to couple with experiments, many challenges are yet to be addressed. Two different methods have been proposed.

Adeosun and Lawal (2009) investigated numerically the RTD of a T-junction microchannel. They proposed to obtain the RTD by solving numerically both the velocity flow field and the mass species transport by means of Computational Fluid Dynamics (CFD). We refer to this method as *fully-CFD*. The proposed method is characterized by two steps: firstly, the equations of flow are solved at the steady state to obtain the velocity distribution in the adopted geometry; the converged solution is then used to simulate the transient response to a pulse input of tracer. This is performed by solving the equation of species as unsteady simulation. They validated the procedure comparing results of simulation with analytic RTD predicted by pure convection model as well as experimental data.

A different approach resorts to the tracking of massless particles, acting as tracer. The Navier-Stokes equations are solved at the steady-state so that the velocity flow field is characterized. Subsequently, a time-dependent study is implemented and the motion of particles is tracked with a lagrangian approach. Aubin et al. (2009) studied the effect of the cross-section aspect ratio on RTD in rectangular microchannels by means of particle tracking. Keeping constant the cross-sectional area they observed a significant narrowing of the RTD for very wide and shallow channels (small aspect ratio). In their case, the motion of particles was fully convective: each particle moves according to the velocity of the fluid. Nevertheless, the assumption of absence of diffusion-like motion is not always valid. The molecular diffusion motion was implemented in a

particle tracking algorithm by (Cantu-Perez et al., 2010). A random-walk term is added to the equation of motion of the particles. At a given time-step the movement of each particle depends on the local velocity of the fluid and an additional contribution, whose length is calculated from the diffusion coefficient. The direction of this contribution is randomly generated. The numerical approach was validated by comparison with both theoretical (Axial Dispersion Model) and experimental RTDs.

In this work, the application of the model based on lagrangian tracking was studied in the pure convective regime. The study focused on the setup of simulation using the commercial software COMSOL Multiphysics.

C.1 Brief description of the numerical model

The approach chosen to model RTD in microreactors relies on fictional particles introduced in the computational domain and tracked over time with a Lagrangian point of view. The particles need to be considered fictional as we use them only to record the residence time of the fluid molecules, from which we can then obtain the RTD. They are massless and do not interact with one another. In general, two mechanisms contribute to the motion of each particle: convection, which is deterministic and governed by the velocity field of the fluid; diffusion (or dispersion), which can be modelled by means of a stochastic approach based on random walk. In specific conditions (low velocities and short channels) the contribution of diffusion (dispersion) can be neglected. The *pure convective* version of this model can be adopted when one is only concerned with the hydrodynamics induced by the geometry of the channels or, differently, when diffusion is negligible.

C.2 Simulations in pure convective regime

We adopt the pure convective particle tracking model to calculate numerical RTDs of straight cylindrical channels. The objective of this study is to validate the model comparing with analytical solutions.

The computational domain is a simple straight cylinder (Figure C.1a). The velocity flow field is simulated at the steady state by solving numerically the Navier-Stokes equations. A mesh independence study is carried out: we found that 930000 computational cells are necessary to simulate a 2.5 cm long channel with 0.5 mm internal diameter. The mesh adopted is hybrid: rectangular and denser cells approaching the walls, triangular structures in the bulk. Once obtained the velocity field, 5000 massless particles are initialized at the inlet boundary. The initial positions of the particles are distributed according to the local velocity (Figure C.2b): in this way we mimic a uniform local flow rate, this being the ideal way to inject tracer particle with non-uniform velocity (Levenspiel and Turner, 1970). The time spent by each particle from the initial time to the time at which it reaches the outlet boundary is recorded and used to calculate the RTD:

$$E = \frac{N_p(\vartheta_i)}{\sum N_p(\vartheta_i)} \frac{1}{\Delta \mathrm{t}} \qquad \text{Eq. C.1}$$

where N_p is the number of particle having a residence time (ϑ_i) between t_i and t_{i+1} and Δt is the time-step used for the sampling of ϑ_i. We used COMSOL 4.3 to run both the CFD simulation (velocity flow field) and the particle tracking, exploiting the built-in module. In Figure C.2 we report the simulated RTDs of six different couples of parameters (length of the channel/flowrate); the values of the parameter used can be found in Table C.1.

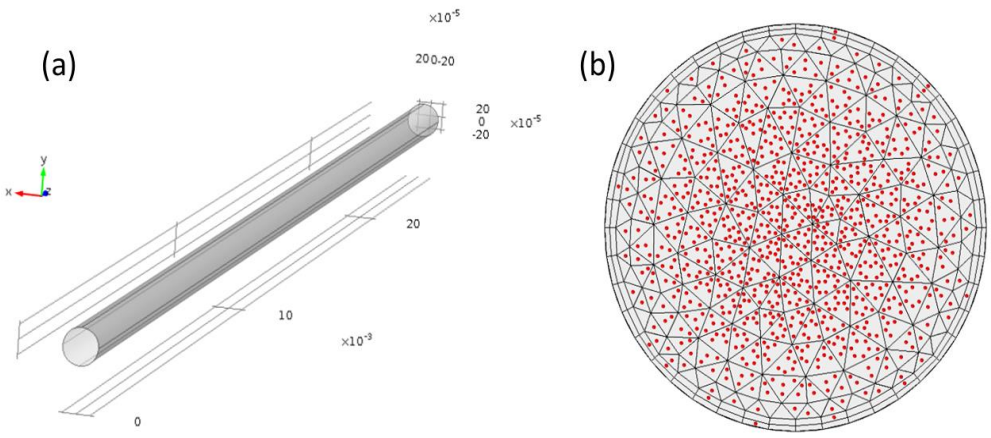

Figure C.1 – (a) Computational domain representative of the channel; (b) position of particle at the inlet boundary.

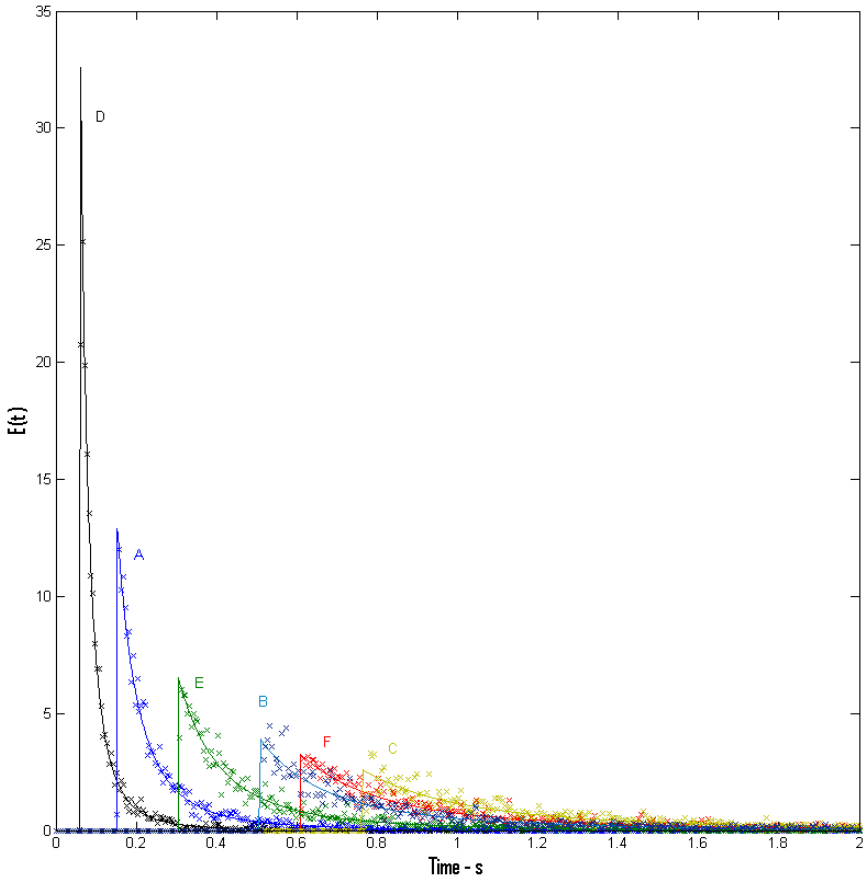

Figure C.2 - Numerical (points) and analytical (solid lines) RTDs for different set of parameters.

For the six couples of parameters considered the simulated RTDs are in good agreement with those predicted by the pure convection model. Both the time at which the first particle reaches the outlet and the peak of the distribution are in all cases matched. Due to space and time discretization the data points are scattered around the theoretical curves. The scattering is more intense when the theoretical residence time ($\tau = L/u$, with u the mean internal velocity), suggesting when simulating long residence time flow systems less accurate results may be generated, particularly in the tail of the distribution. However the mean residence time (the first moment of the numerical RTD) matches very closely the theoretical ones with a 1 % error for the higher residence time.

Table C.1 – Parameters corresponding to different RTDs simulated.

RTD	d_t/L	$\dot{v}$ **(ml/min)**	**L (cm)**	**τ (s)**	$\bar{t}$ **(s)**
A	50	1	2.5	0.3040	0.3055
B	50	0.3	2.5	1.0134	1.0244
C	50	0.2	2.5	1.5020	1.5218
D	20	1	1	0.1216	0.1209
E	20	0.2	1	0.6080	0.6048
F	20	0.1	1	1.2161	1.2095

Although these simulations have been carried out under relatively simple geometry and flow conditions, they fully validate our approach and allow us to use it with more complicated geometries provided that diffusion (dispersion) mechanism is not significant. However, we can also conclude that considerably fine meshes are needed to acquire accurate results. It is therefore crucial to reduce the size of the domain to simulate and in turn the number of computational cells: this can be done by identifying symmetries or repetitive units.

Bibliography

Adeosun, J.T., Lawal, A., 2009. Numerical and experimental studies of mixing characteristics in a T-junction microchannel using residence-time distribution. Chem. Eng. Sci. 64, 2422–2432.

Alexoff, D., Hallaba, K., Schlyer, D., Ferrieri, R., 1995. A simple liquid detector for radiopharmaceutical processing systems, in: 5. International Workshop on Targetry and Target chemistry,Upton, NY (United States),19-23 Sep 1993.

Anthakrishnan, V., Gill, W., Barduhn, A., 1965. Laminar Dispersion in Capillaries: Part I. Mathematical Analysis. AIChE J. 1063–1072.

Arampatzis, G., Assimacopoulos, D., Mitsoulis, E., 1994. Treatment of numerical diffusion in strong convective flows. Int. J. Numer. Methods Fluids 18, 313–331.

Aris, R., 1956. On the dispersion of a solute in a fluid flowing through a tube. Proc. R. Soc. A Math. Phys. Eng. Sci. 235, 67–77.

Aubin, J., Prat, L., Xuereb, C., Gourdon, C., 2009. Effect of microchannel aspect ratio on residence time distributions and the axial dispersion coefficient. Chem. Eng. Process. Process Intensif. 48, 554–559.

Berger, S.A., Talbot, L., Yao, L.S., 1983. Flow in Curved Pipes. Annu. Rev. Fluid Mech. 15, 461–512.

Bošković, D., Loebbecke, S., 2008. Modelling of the residence time distribution in micromixers. Chem. Eng. J. 135, S138–S146.

Bošković, D., Loebbecke, S., Gross, G. a., Koehler, J.M., 2011. Residence Time Distribution Studies in Microfluidic Mixing Structures. Chem. Eng. Technol. 34, 361–370.

Cantu-Perez, A., Barrass, S., Gavriilidis, A., 2010. Residence time distributions in microchannels: Comparison between channels with herringbone structures and a rectangular channel. Chem. Eng. J. 160, 834–844.

Cantu-Perez, A., Barrass, S., Gavriilidis, A., 2011. Hydrodynamics and reaction studies in a layered herringbone channel. Chem. Eng. J. 167, 657–665.

Capel, A.J., Edmondson, S., Christie, S.D.R., Goodridge, R.D., Bibb, R.J., Thurstans, M., 2013. Design and additive manufacture for flow chemistry. Lab Chip 13, 4583–90.

Castelain, C., Mokrani, A., Legentilhomme, P., Peerhossaini, H., 1997. Residence time distribution in twisted pipe flows: helically coiled system and chaotic system. Exp. Fluids 22, 359–368.

Cho, S., Kang, D., Choo, J., Mello, A. de, Chang, S., 2011. Recent advances in microfluidic technologies for biochemistry and molecular biologys. BMB Rep. 705–712.

Dankwerts, P. V., 1953. Continuous flow systems. Chem. Eng. Sci. 2, 1 – 13.

Dean, W.R., 1927. Note on the motion of fluid in a curved pipe. Philos. Mag. 4, 208–223.

Dean, W.R., 1928. The streamline motion of fluid in a curved pipe. Philos. Mag. 5, 673–695.

Erdogan, M.E., Chatwin, P.C., 1967. The effects of curvature and buoyancy on the laminar dispersion of solute in a horizontal tube. J. Fluid Mech. 29, 465.

Fogler, H.S., 2006. Elements of Chemical Reaction Engineering, 4th Ed. ed. Pearson Education.

Günther, A., Khan, S.A., Thalmann, M., Trachsel, F., Jensen, K.F., 2004. Transport and reaction in microscale segmented gas-liquid flow. Lab Chip 4, 278–86.

Günther, M., Schneider, S., Wagner, J., Gorges, R., Henkel, T., Kielpinski, M., Albert, J., Bierbaum, R., Köhler, J.M., 2004. Characterisation of residence time and residence time distribution in chip reactors with modular arrangements by integrated optical detection. Chem. Eng. J. 101, 373–378.

Ham, J.-H., Platzer, B., 2004. Semi-Empirical Equations for the Residence Time Distributions in Disperse Systems - Part 1: Continuous Phase. Chem. Eng. Technol. 27, 1172–1178.

Hessel, V., Löwe, H., Schönfeld, F., 2005. Micromixers—a review on passive and active mixing principles. Chem. Eng. Sci. 60, 2479–2501.

Janssen, L., 1976. Axial dispersion in laminar flow through coiled tubes. Chem. Eng. Sci. 31, 215–218.

Johnson, M., Kamm, R., 1986. Numerical studies of steady flow dispersion at low Dean number in a gently curving tube. J. Fluid Mech. 172, 329–345.

Jones, S.W., Thomas, O.M., Aref, H., 1989. Chaotic advection by laminar flow in a twisted pipe. J. Fluid Mech. 209, 335.

Kreutzer, M.T., Günther, A., Jensen, K.F., 2008. Sample dispersion for segmented flow in microchannels with rectangular cross section. Anal. Chem. 80, 1558–67.

Kumar, V., Mridha, M., Gupta, a. K., Nigam, K.D.P., 2007. Coiled flow inverter as a heat exchanger. Chem. Eng. Sci. 62, 2386–2396. doi:10.1016/j.ces.2007.01.032

Kumar, V., Nigam, K.D.P., 2005. Numerical simulation of steady flow fields in coiled flow inverter. Int. J. Heat Mass Transf. 48, 4811–4828.

Kwak, D., Kiris, C., Kim, C.S., 2005. Computational challenges of viscous incompressible flows. Comput. Fluids 34, 283–299.

Levenspiel, O., 1999. Chemical Reaction Engineering, 3rd ed. John Wiley and Sons.

Levenspiel, O., Lai, B.W., Chatlynne, C.Y., 1970. Tracer curves and the residence time distribution. Chem. Eng. Sci. 25, 1611–1613.

Levenspiel, O., Smith, Laan, V. der, 1956. Notes on the diffusion-type model for longitudinal mixing in flow. Lett. to Ed.

Levenspiel, O., Turner, J.C.R., 1970. The interpretation of residence-time experiments. Chem. Eng. Sci. 25, 1605–1609.

Lobo, V.M.M., 1993. Mutual diffusion coefficients in aqueous electrolyte solutions. Pure Appl. Chem. 65, 2613–2640.

Lohse, S., Kohnen, B.T., Janasek, D., Dittrich, P.S., Franzke, J., Agar, D.W., 2008. A novel method for determining residence time distribution in intricately structured microreactors. Lab Chip 8, 431–8.

Mandal, M., Aggarwal, P., Nigam, K.D.P., 2011. Liquid–Liquid Mixing in Coiled Flow Inverter. Ind. Eng. Chem. Res. 50, 13230–13235.

Mandal, M.M., Serra, C., Hoarau, Y., Nigam, K.D.P., 2010. Numerical modeling of polystyrene synthesis in coiled flow inverter. Microfluid. Nanofluidics 10, 415–423.

Marre, S., Jensen, K.F., 2010. Synthesis of micro and nanostructures in microfluidic systems. Chem. Soc. Rev. 39, 1183–202.

McKay, G., Otterburn, M.S., Sweeney, A.G., 1981. Surface mass transfer processes during colour removal from effluent using silica. Water Res. 15, 327–331.

Minnich, C.B., Sipeer, F., Greiner, L., Liauw, M.A., 2010. Determination of the Dispersion Characteristics of Miniaturized Coiled Reactors with Fiber-Optic Fourier Transform Mid-infrared Spectroscopy. Ind. Eng. Chem. Res. 49, 5530–5535.

Mridha, M., Nigam, K.D.P., 2008. Coiled flow inverter as an inline mixer. Chem. Eng. Sci. 63, 1724–1732.

Nagy, K.D., 2011. Catalyst Immobilization Techniques for Continuous Flow Synthesis. Chem. Eng. Massachusetts Institute of Technology.

Nauman, B., 1977. The residence time distributions for laminar flow in elically coiled tubes. Chem. Eng. Sci. 287, 287–293.

Nauman, B., 1981. Residence time distribution in systems governed by the dispersion equation. Chem. Eng. Sci. 36, 957–966.

Nauman, E.B., 2008. Residence Time Theory. Ind. Eng. Chem. Res. 47, 3752–3766.

Nauman, E.B., Buffham, B.A., 1983. Mixing in Continuous Flow Systems. John Wiley & Sons, New York.

Nguyen, N.-T., 2002. Fundamentals and Applications of Microfluidics. William Andrew.

Nguyen, N.-T., Wu, Z., 2005. Micromixers—a review. J. Micromechanics Microengineering 15, R1–R16.

Nigam, K., Vasudeva, K., 1976. Influence of curvature and pulsations on laminar dispersion. Chem. Eng. Sci. 31, 1–3.

Parida, D., Serra, C. a., Garg, D.K., Hoarau, Y., Bally, F., Muller, R., Bouquey, M., 2014. Coil Flow Inversion as a Route To Control Polymerization in Microreactors. Macromolecules 47, 3282–3287.

Roberge, D.M., Ducry, L., Bieler, N., Cretton, P., Zimmermann, B., 2005. Microreactor technology: A revolution for the fine chemical and pharmaceutical industries? Chem. Eng. Technol. 28, 318–323. 8

Ruthven, D., 1971. The residence time distribution for ideal laminar flow in helical tube. Chem. Eng. Sci. 26, 1113–1121.

Saxena, A.K., Nigam, K.D.P., 1984. Coiled configuration for flow inversion and its effect on residence time distribution. AIChE J. 30, 363–368.

Squires, T.M., Quake, S.R., 2005. Microfluidics : Fluid physics at the nanoliter scale. Rev. Mod. Phys. 77, 977 – 1026.

Taylor, E.S., 1968. Film notes for secondary flow [WWW Document]. Massachussets Inst. Technol. URL http://web.mit.edu/hml/ncfmf/13SC.pdf

Taylor, G., 1953. Dispersion of soluble matter in solvent flowing slowly through a tube. Proc. R. Soc. A Math. Phys. Eng. Sci. 219, 186–203.

Taylor, G.I., 1960. Deposition of a viscous fluid on the wall of a tube. J. Fluid Mech. 10, 161.

Trachsel, F., Günther, A., Khan, S.A., Jensen, K.F., 2005. Measurement of residence time distribution in microfluidic systems. Chem. Eng. Sci. 60, 5729–5737.

Trivedi, R., Vasudeva, K., 1974. RTD for diffusion free laminar flow in helical coils. Chem. Eng. Sci. 29, 2291–2295.

Trivedi, R., Vasudeva, K., 1975. Axial dispersion in laminar flow in helical coils. Chem. Eng. Sci. 30, 317–325.

Vashisth, S., Nigam, K.D.P., 2008. Liquid-phase residence time distribution for two-phase flow in coiled flow inverter. Ind. Eng. Chem. Res. 47, 3630–3638.

Wen, C.Y., Fan, L.T., 1975. Models for Flow Systems and Chemical reactors. Marcel Dekker, New York.